

**DESIGN AND DEVELOPMENT OF FUNCTIONALIZED IRON  
OXIDE BASED NANOZYMES FOR DETECTING DISEASE  
SPECIFIC BIOMOLECULES**

by

**Fatema Zerine Farhana**

In the partial fulfillment of the requirement for the degree

of

**DOCTOR OF PHILOSOPHY**



**Department of Chemistry**

**BANGLADESH UNIVERSITY OF ENGINEERING AND  
TECHNOLOGY (BUET)**

**DHAKA-1000**

**October 2021**

**Bangladesh University of Engineering and Technology (BUET)**  
**Dhaka-1000**  
**Department of Chemistry**



**Certification of Thesis**

**A thesis on**

**DESIGN AND DEVELOPMENT OF FUNCTIONALIZED IRON OXIDE  
BASED NANOZYMES FOR DETECTING DISEASE SPECIFIC  
BIOMOLECULES**

**By**

**Fatema Zerin Farhana**

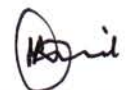
Roll No: 0417034002, Session: April-2017, has been accepted as satisfactory in partial fulfillment of the requirements for the degree of Ph.D. in Chemistry and certify that the student has demonstrated satisfactory knowledge of the field covered by this thesis in an oral examination held on 13.10.2021.

**Board of Examiners**

**1. Dr. Md. Shakhawat Hossain Firoz**  
Professor  
Department of Chemistry  
BUET, Dhaka-1000.

  
13.10.21  
\_\_\_\_\_  
Supervisor & Chairman

**2. Dr. Md Abdur Rashid**  
Head  
Department of Chemistry  
BUET, Dhaka-1000

  
13.10.21  
\_\_\_\_\_  
Member (Ex-Officio)

**3. Dr. Al-Nakib Chowdhury**  
Professor  
Department of Chemistry  
BUET, Dhaka-1000



---

Member

**4. Dr. Shakila Rahman**  
Professor  
Department of Chemistry  
BUET, Dhaka-1000



---

Member

**5. Dr. Chanchal Kumar Roy**  
Assistant Professor  
Department of Chemistry  
BUET, Dhaka-1000



---

Member

**6. Dr. Md. Mominul Islam**  
Professor  
Department of Chemistry  
University of Dhaka, Dhaka -1000



---

Member

**7. Dr. Muhammed Shah Miran**  
Professor  
Department of Chemistry  
University of Dhaka, Dhaka -1000



---

Member (External)



## CANDIDATE'S DECLARATION

It is hereby declared that this thesis or any part of it has not been submitted elsewhere for the award of any degree or diploma.

A handwritten signature in black ink, appearing to read 'Fatema Zerine Farhana', written over a horizontal line.

**Fatema Zerine Farhana**

# **DEDICATED TO**

**Nabiha Nawshin**

**And**

**Nashita Zahin**

## Acknowledgement

---

I would like to express my sincere gratitude to both of my PhD supervisors **Dr. Md. Shakhawat Hossain Firoz** (supervisor), Professor, Department of Chemistry, BUET, and **Dr. Muhammad J. A. Shiddiky** (collaborative supervisor), Associate professor, Griffith University, Australia, for their invaluable guidance during my PhD candidature. I really appreciate their continuous support, leadership, motivation and scientific advices. I owe **Dr. Md. Shakhawat Hossain Firoz** a big debt of gratitude for providing me with the opportunity to work on the fascinating topic of electrochemical nano-biosensors while also providing me with the opportunity to collaborate with many research groups, and I consider myself extremely fortunate to be a part of the nanoChem research group.

I would like to acknowledge CASR, BUET and Shiddiky lab, Griffith University for providing me all the necessary resources needed for my PhD research work. I would like to convey my deepest gratitude to all teachers Department of Chemistry, BUET, for their valuable suggestions and guidance during the course and research period.

My deepest gratitude goes to all my lab mates: Amzad, Imon, Nadeem, Sujon, Shuvo, Mim, Noman, Bushra, Sharmin and Fahima for all funny moments we had together in last years. My special thanks are reserved for Reaz for his enormous support and motivation during my candidature time.

I would like to take this opportunity to express my infinite gratitude to my parents for their unconditional love. They were always there for me in hardest moments. I was also lucky enough to have friends like Liya and Shafiq, they were supporting me and encouraging me despite being far. Last but not the least I would like to thank my loving family, whose sacrifice, incomparable love and inspiration helped me to achieve my goals and follow my dreams.

## Abstract

---

Early sensitive and specific cancer biomolecule detection play a vital role in life science and in biosensor. Recently, nanozymes that exhibit enzyme mimicking catalytic activity have been immensely used in molecular biosensor as an alternative to natural enzymes. Herein, I report a starch-assisted method for the synthesis of a novel class of carboxyl group-functionalized iron oxide nanoparticles (C-IONPs) that emerged peroxidase mimicking activity and follow Michaelis-Menten kinetics. Scanning electron and transmission electron microscopy analysis revealed that the nanoparticles possess a spherical shape with an average size of around 250 nm. Raman and X-ray photoelectron spectroscopy spectra reveal that nanoparticles surface is coated with COOH group. We demonstrated that C-IONPs can bind biomarkers in complicated mixtures, allowing for fast magnetic separation and improved electrochemical detection of cancer biomarkers particularly for methylated DNA and exosomes from cancer cells. Our study revealed that a straightforward approach for the direct isolation and measurement of disease-specific exosomes and methylated DNA was developed using C-IONPs. The Chronoamperometric analysis revealed that the approach has an excellent specificity for OVCAR3 cell-derived exosomes (linear dynamic range,  $6.25 \times 10^5 - 1.0 \times 10^7$  exosomes/mL; detection limit,  $1.25 \times 10^6$  exosomes/mL) with a relative standard deviation of  $<5.0\%$  ( $n=3$ ). I believe that this approach is a promising candidate for the development of advanced exosome biosensing assays for various clinical applications. And a differential pulse voltametric (DPV) examination of the electroactive indicator  $[\text{Ru}(\text{NH}_3)_6]^{3+}$  bound to the surface-adsorbed DNA yielded an electrochemical estimate of the amount of DNA adsorbed on the electrode surface, which correlates to the DNA methylation level in the sample. Using a 200 ng DNA sample, the assay could successfully detect as low as 5% differences in global DNA methylation levels with high reproducibility (relative standard deviation (% RSD) =  $<5\%$  for  $n = 3$ ). The method could also be used to detect different amounts of global DNA methylation in synthetic samples and cell lines in a reproduce able manner. The approach does not require bisulfite treatment, does not rely on enzymes for signal creation, and can detect global DNA methylation without PCR amplification using clinically relevant amounts of sample DNA. I believe that this proof-of-concept technology could have used in point-of-care settings for liquid biopsy-based global DNA methylation analysis.

## Table of Contents

1	Introduction.....	3
	Common nanozymes for biosensors .....	7
	Nanozyme as a substitute of HRP.....	10
	Applications of nanozymes in Lateral-flow immunodetection.....	12
	Application of nanozymes in Colorimetric sensor .....	14
	Application of nanozymes in Fluorescence sensor.....	15
	Applications of nanozyme in electrochemical biosensors.....	16
1.1.1	Genosensor.....	16
1.1.2	Cytosensor .....	19
1.1.3	Immunosensor.....	20
1.1.4	Aptasensor .....	23
	Synthesis of common nanozymes for biosensing.....	24
1.1.5	Synthesis of metal oxides nanozymes .....	25
1.1.6	Synthesis of metallic nanozymes.....	27
1.1.7	Synthesis of carbon-based nanozymes .....	28
	Present remarks in the synthesis of nanozymes to approach biomolecule detection:	30
	Objectives .....	31
	References.....	33
2	Synthesis and Characterization of –COOH Functionalized Magnetic Iron oxide Nanozymes.....	45
2.1	Introduction.....	45
	Experimental.....	47
2.1.1	Reagents and Materials .....	47
2.1.2	Synthesis of –COOH Functionalized Fe <sub>2</sub> O <sub>3</sub> Magnetic Nanoparticles (C-IONPs) 47	



2.1.3	Characterization of C-IONPs.....	49
2.1.4	Peroxidase-like Activity of C-IONPs .....	49
	Results and Discussion .....	51
2.1.5	Preparation and Electron Microscopic Characterization of C-IONPs .....	51
2.1.6	X-Ray Photoelectron Spectroscopic (XPS), Raman Spectroscopy and X-ray Diffraction (XRD) Pattern Analysis of C-IONPs .....	58
2.1.7	Magnetic Properties of C-IONPs.....	62
2.1.8	Peroxidase like Activity of C-IONPs.....	63
	Conclusions.....	68
3	Direct Isolation and Detection of Exosomes Using Functionalized Iron oxide (C- IONPs) Nanozymes .....	73
	Introduction.....	73
	Experimental.....	75
3.1.1	Reagents and Materials .....	75
3.1.2	Cell Culture and Isolation of Exosomes .....	75
3.1.3	Cryo-Transmission Electron Microscopy (Cryo-TEM) .....	75
3.1.4	Preparation of Anti-CD9 Conjugated C-IONPs .....	76
3.1.5	Direct Isolation of Exosomes from Cell Culture Media and Plasma Samples 76	
3.1.6	Fabrication of Sensor and Chronoamperometric Detection of Exosomes	77
	Results and Discussion .....	77
3.1.7	Size and Vesicular Compartments of Exosomes .....	77
3.1.8	FTIR Analysis of C-IONPs and Anti-CD9/C-IONPs.....	78
3.1.9	Direct Isolation and Detection of Exosomes .....	79
3.1.10	Assay Functionality and Specificity .....	81
3.1.11	Assay Sensitivity.....	83

3.1.12	Analysis of Known concentration of Spiked Exosomes in Plasma Samples	85
	Conclusions.....	87
	References.....	89
4	Detection and quantification of DNA methylation using functionalized iron oxide (C-IONPs) based nanozymes.....	93
	Introduction.....	93
	Materials and methods .....	95
	4.1.1    Materials .....	95
	4.1.2    Preparation of DNA Samples .....	96
	4.1.3    Preparation of Anti-5mC Conjugated C-IONPs (5mC/C-IONPs).....	96
	4.1.4    Electrochemical Detection of Global DNA Methylation .....	97
	Result and discussion.....	97
	4.1.5    FTIR Analysis of C-IONPs and Anti-5mC/C-IONPs.....	97
	4.1.6    Principal of <i>e</i> -MagnetoMethyl IP Method.....	99
	4.1.7    Functionality and Selectivity of the Assay .....	101
	4.1.8    Analysis of Heterogeneous DNA Methylation.....	103
	4.1.9    Analysis of DNA Methylation in Cell Lines .....	106
	Conclusions.....	107
	References.....	109
5	Conclusions.....	114
	Publication.....	116

## List of Figures

---

Figure 1.1 Global cancer incidences, causes and future predictions .....	4
Figure 1.2 Schematic representation of the nanozyme's catalytic activities and its application in the electrochemical biosensor. Nanozymes can be functionalized with a range of receptor probes (e.g., complementary capture probes for DNA and RNA targets, antibodies for proteins, etc.) by conventional surface modification procedures. The probe-functionalized nanozymes can capture the targets (e.g., pathogen, cancer cell, exosome, nucleic acid) via the specific interaction between nanozyme-bound probes and targets. The nanozymes-attached targets can then be quantified electrochemically or optically (i.e., naked eye and UV-visible) via an ELISA-type sandwich immunoassay or sandwich hybridization method. ....	5
Figure 1.3 Schematic presentation of the typical enzyme-mimetic activities of nanozymes, their advantages, and limitations compared to natural enzymes, recommended strategies to improve their substrate specificity, and their applications in electrochemical biosensors. ....	6
Figure 1.4 Classification of nanozymes [8, 27-28] (*) Mark represents the nanozymes commonly used for electrochemical biosensors. ....	9
Figure 1.5 Ultrasensitive ELISA in the determination of DNA by using Nanozyme nest [48]. ....	11
Figure 1.6(a). Antibody functionalized Pt nanocatalysts (PtNCs) and biotinylated nanobody. (b) Site-selective chemical modification of a nanobody with an exposed cysteine mutation (red), where lysine residues are highlighted in orange on the structural model (left and cartoon of oriented elements at the streptavidin test line. (c) Comparison of dynamic ranges of 4 <sup>th</sup> generation LIFA, ELISA and PtNC LIFA. Reprinted from Ref [51]. ....	13
Figure 1.7(A) Synthesis of FeTCPP@MOF nanozymes followed by covalent coupling with streptavidin (SA) to form FeTCPP@MOF-SA composite and (B) Target binding initiates allosteric switch of the hairpin probe allows FeTCPP@MOF-SA to recognize the	

probe and o-PD oxidation provides the electrochemical signal. Reprinted with permission from Ref [66]. .....	18
Figure 1.8 Schematic representation of circulating tumor cell detection using reduced graphene oxide/molybdenum disulfide (rGO/MoS <sub>2</sub> ) composites modified magnetic glassy carbon electrode (MGCE) as a detector, and aptamer modified magnetic Fe <sub>3</sub> O <sub>4</sub> NPs as dispersible capture agents.Reproduce from ref [69]. .....	20
Figure 1.9 Schematic representation of naked eye and electrochemical detection of p53 autoantibody where target recognition and electrochemical measurement are operated in two separated electrodes. Reprinted from Ref. [33]. .....	22
Figure 1.10 Schematic representation of layer-by-layer (LBL) assembly of the nonenzymatic nanoprobe NP1 (aptamer) and NP2 (cDNA) and NTH-assisted dual-aptamer based electrochemical sensor for detection of cTnI. Reprinted from Ref. [78]. .....	23
Figure 2.1 Flowchart diagram describing the workflow for synthesis of –COOH functionalized iron oxide. ....	48
Figure 2.2 Optimization of C-IONPs concentration. Mean responses of absorbance obtained for the designated concentration of (5, 10, 15, 20, and 25 μg) of C-IONPs. Peroxidase-mimicking activity C-IONPs was performed in the presence of 800 μM TMB and 700 mM H <sub>2</sub> O <sub>2</sub> , in 0.2 M acetate buffer (pH 3.6) at room temperature. UV-vis absorbance was recorded at 652 nm. ....	50
Figure 2.3 Comparison of nanozyme catalytic activity of C-IONPs with HRP. For (A), TMB = 500 μM, H <sub>2</sub> O <sub>2</sub> = 700 mM and Fe <sub>2</sub> O <sub>3</sub> = 15 μg; (B), TMB = 500 μM, H <sub>2</sub> O <sub>2</sub> = 700 mM and HRP = 0.5 ng; (C), TMB = 1000 μM, H <sub>2</sub> O <sub>2</sub> = 700 mM and Fe <sub>2</sub> O <sub>3</sub> = 15 μg/μL, and (D), TMB = 1000 μM, H <sub>2</sub> O <sub>2</sub> = 700 mM and HRP = 0.5 ng). .....	51
Figure 2.4 schematic diagram of synthesis and functionalization of iron oxide. ....	52
Figure 2.5 Mechanism of reaction between the iron oxide nanoparticles and dopamine. ....	53

Figure 3.1 Cryo-TEM images of OVCAR3 cell derived exosomes demonstrating size and vesicular compartments such as membrane layers. ....	78
Figure 3.2 FTIR analysis of C-IONPs and anti-CD9/C-IONPs.....	79
Figure 3.3 Schematic representation of the assay for the direct detection of ovarian cancer cell-derived exosomes. CD-9 antibody functionalised-C-IONPs were dispersed in the conditioned exosome media derived from OVCAR3 or Met5a cell lines. After magnetic isolation and separation, the exosome-bound C-IONPs were incubated onto an extravidin-modified screen-printed carbon electrode pre-functionalized with biotinylated anti-CA-125. The immunocomplex formed on the electrode surface (C-IONPs/anti-CD9/Exo/anti-CA-125/SPCE) was then treated with H <sub>2</sub> O <sub>2</sub> /HQ and chronoamperometric measurement at 0.2V (vs. Ag/AgCl) was used to get the amperometric current.....	80
Figure 3.4 Chronoamperometric responses obtained for positive and four control experiments. Positive = undiluted conditioned exosome media derived from OVCAR3 cells, NTC = Undiluted conditioned exosome media derived from Met5a cells, NAC = no-antibody control, NNPC = no-nanoparticle control. Inset in (a), enlarged view of the amperograms. (b) Corresponding $\Delta i$ . Error bars represent the standard deviation of three repetitive experiments.....	82
Figure 3.5 Amperometric responses obtained for serially diluted conditioned media derived from OVCAR3 cells with known concentration of exosomes ( $1 \times 10^7$ to $6.2 \times 10^5$ exosomes/mL). Inset in (a), enlarged view of the amperograms. (b) Corresponding $\Delta i$ . Error bars represent the standard deviation of three repetitive experiment.....	84
Figure 3.6 Comparison of HRP and C-IONPs catalyzed HQ/H <sub>2</sub> O <sub>2</sub> reaction and the corresponding current response generated. HRP catalyzed reaction provided 9-11 times higher current response compared C-IONPs. Error bars represent the relative standard deviation of three experiments.....	85
Figure 3.7 Amperometric responses obtained for the analysis of known concentration of exosomes ( $1 \times 10^7$ and $1.25 \times 10^6$ exosomes/mL). NTC corresponds to samples without exosomes. (a) Comparison of current responses obtained for spiked-in plasma and buffer (PBS) exosome samples. The inset in (b), shows the enlarged view of the corresponding	

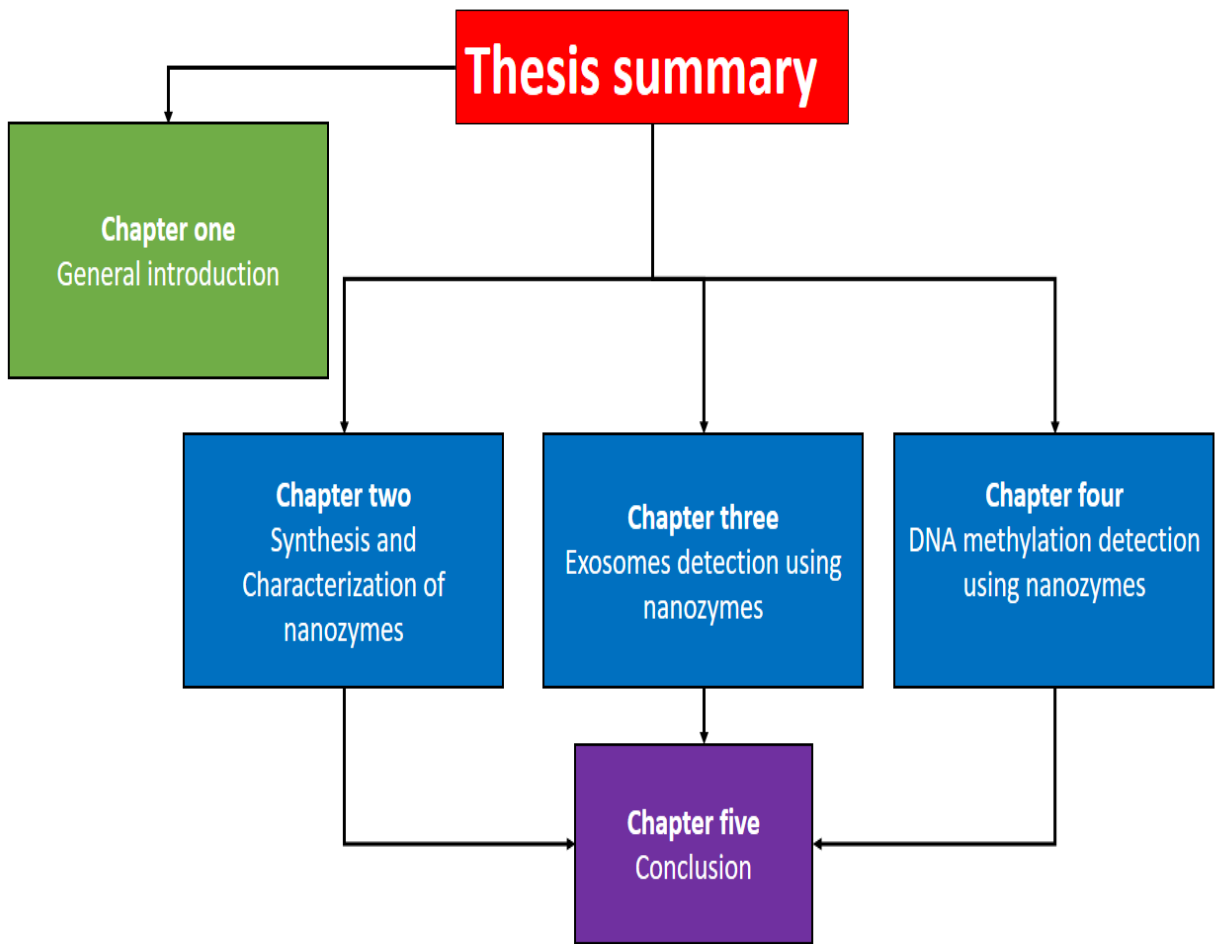
amperograms. Error bars represent the relative standard deviation of three experiments. .....	86
Figure 4.1 Conjugation of anti-5mC antibody with C-IONPs by EDC/NHS coupling chemistries. ....	98
Figure 4.2 FTIR analysis of C-IONPs and anti-5mC/C-IONPs .....	99
Figure 4.3 Schematic representation of the e-MagnetoMethyl IP method. Methylated DNA is subjected to anti-5mC/C-IONPs mediated immunoprecipitation (IONPs-anti-5mC/mDNA complex). Immunoprecipitated DNA is adsorbed directly onto the SPGE surface and electrochemically detected as a function of current response generated by the reduction of DNA backbone-bound $[\text{Ru}(\text{NH}_3)_6]^{3+}$ molecules. ....	100
Figure 4.4 (a) Functionality of e-MagnetoMethyl IP method. ~2.5-fold higher current response was obtained for mDNA (100% methylated DNA) compared to umDNA (0% methylated DNA). (b) Specificity of the assay. Current response obtained by NTC (no-target control), NAC (C-IONPs not conjugated to anti-5mC) and bare electrode was significantly lower compared to sample with 5% methylated DNA. DPV measurements were conducted at room temperature in the presence of 10 mM tris-buffer (pH 7.4)..	102
Figure 4.5(a) Differential pulse voltammetry analysis of heterogeneous DNA methylation levels. DPV current changes are corresponding to level of DNA methylation in different samples. (b) Average percent change in DPV current responses obtained for various DNA methylation levels. DPV measurements were conducted at room temperature in the presence of 10 mM tris-buffer (pH 7.4). Each data point represents the average of three separate measurements, and error bars represent the standard deviation of measurements (%RSD = < 5% for n =3).....	104
Figure 4.6(a) Differential pulse voltammetry analysis of heterogeneous DNA methylation levels. DPV current changes are corresponding to level of DNA methylation in different samples. (b) Average percent change in DPV current responses obtained for various DNA methylation levels. Each data point represents the average of three separate measurements, and error bars represent the standard deviation of measurements (%RSD	

= < 5% for n =3). DPV measurements were conducted at room temperature in the presence of 10 mM tris-buffer (pH 7.4)..... 106

### **List of Tables**

Table 1 d-space values calculated from electron diffraction pattern and standard atomic spacing obtained of Fe<sub>2</sub>O<sub>3</sub> along with their hkl indexes from JCPDS card (39-1346).....56

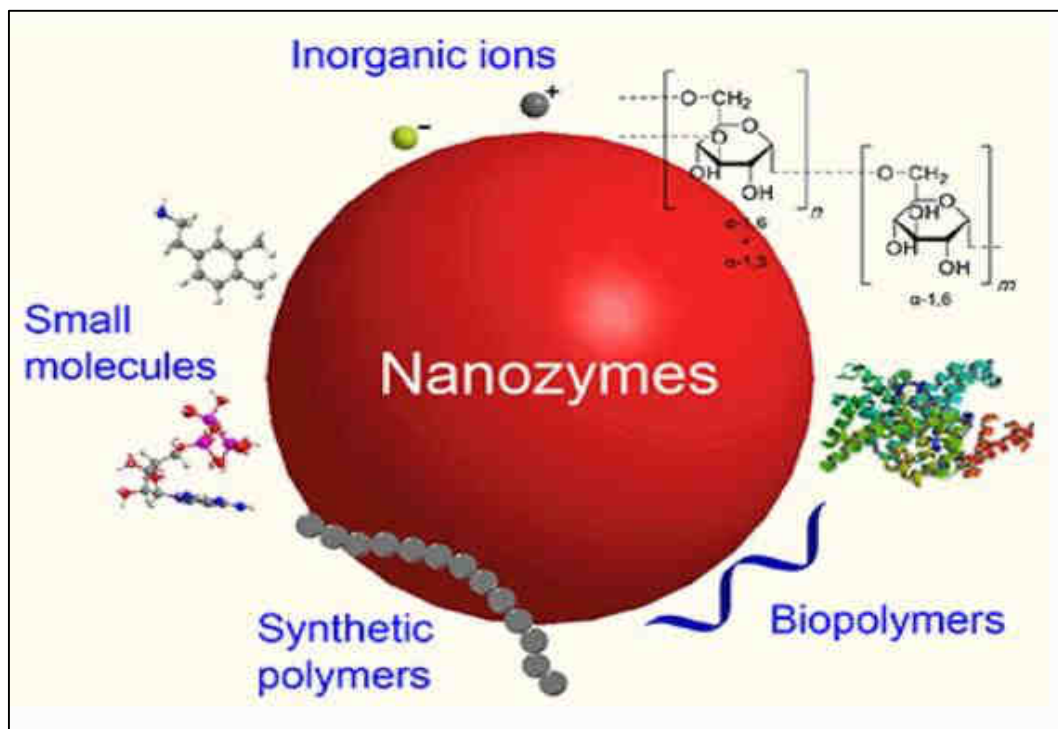
Table 2 The obtained kinetic parameters of Fe<sub>2</sub>O<sub>3</sub> in comparison with the previous findings ..... 67





# CHAPTER ONE

## General Introduction



# CHAPTER ONE

---

## 1 Introduction

Early detection of diseases, particularly cancer, requires an ultrasensitive and easy technique for detecting and measuring disease-specific biomolecules. Cancer is considering one of the leading causes of death in the modern world. Cancer is an excessive complicated and variable disease and has a substantial social and economic impact on individuals, families and the community. According to WHO, in 2018, globally approximately 9.6 million people were died from cancer and detected 18.1 million new cases. According to the statistics, by the year 2040, around 27.5 million new cases will be detected globally. Also in Bangladesh, 2018, total cancer affected people was about 150 thousand and died around 108 thousand that means 72% of people could not survive. Thus, early detection of cancer biomarkers is crucial to increase the survival rate. It is known that cancer and pathogenic infections present their signature biomarkers (e.g., DNA methylation, exosomes, circulating tumor DNA, microRNA) in the peripheral circulatory system which can be used as diagnostics, prognostics and therapeutic markers[1-2]. The concentration of these biomarkers in the peripheral blood or other bodily fluids (saliva, urine, etc.) is extremely low at the early stages of the disease [2]. Over the past several decades, electrochemical biosensors have successfully been used in detecting a range of molecular and cellular biomarkers in the fields of biomedical, biotechnology, and environmental sciences.

Electrochemical biosensor, a subclass of chemical sensors, is a miniature device that produces a measurable electrical signal which is directly related to the analyte concentration in the sample matrix. These devices apply the analytical power of electrochemical techniques with the high specificity and selectivity of biological recognition processes. An electrochemical biosensor consists of biological recognition elements (enzyme, proteins, antibodies, nucleic acids, cells, tissues, or membrane receptors) that specifically interacts with the target of the analyte and uses an electrode as the transducer to convert the biological change into the quantitative amperometric and potentiometric response. Depending on the nature and detection mechanism of the biological recognition process, electrochemical biosensors can be divided into two main categories: biocatalytic devices and affinity sensors.

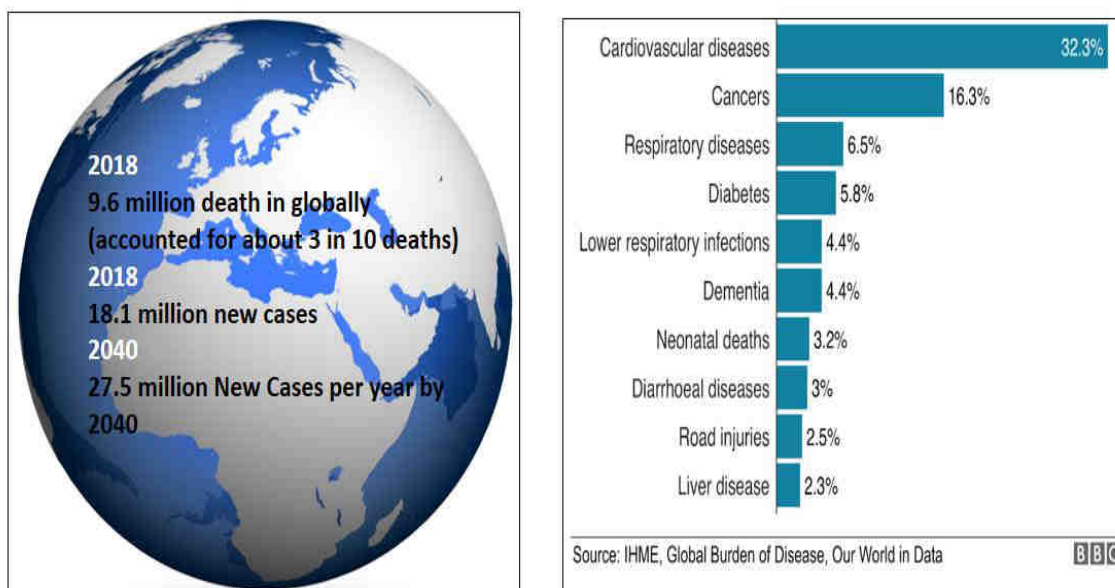


**Figure 1.1** Global cancer incidences, causes and future predictions

Biocatalytic devices employ enzymes, cells or tissues as immobilized biocomponents and utilize the enzyme-target reaction to produce electroactive species. While affinity sensors employ antibodies, membrane receptors or nucleic acids and utilize the interaction between bioreceptor and analyte to create measurable signal. Immunosensors, aptasensors, DNA sensors, and genosensors are example of affinity biosensors. Most importantly, the electrochemical detection system is amenable to miniaturization and offers other advantages such as simplicity, cost-effective nature, high sensitivity and specificity [3]. Recently, nanozyme-based electrochemical biosensor provides a suitable platform that facilitates the formation of probe-target complex (i.e., specific recognition event) in such a way that the binding event triggers a useable signal for electrochemical readout [4]. As shown in **Fig 1.2**, biorecognition and signal transduction are two critical elements in the fabrication of electrochemical biosensors, and nanozyme have played an essential role in this regard.

The term “nanozymes” was first introduced by Pasquato and co-workers in 2004 to describe the ribonuclease-like activity of triazacyclononane functionalized gold nanoparticles (NPs) in the transphosphorylation reaction [5]. The definition of nanozyme

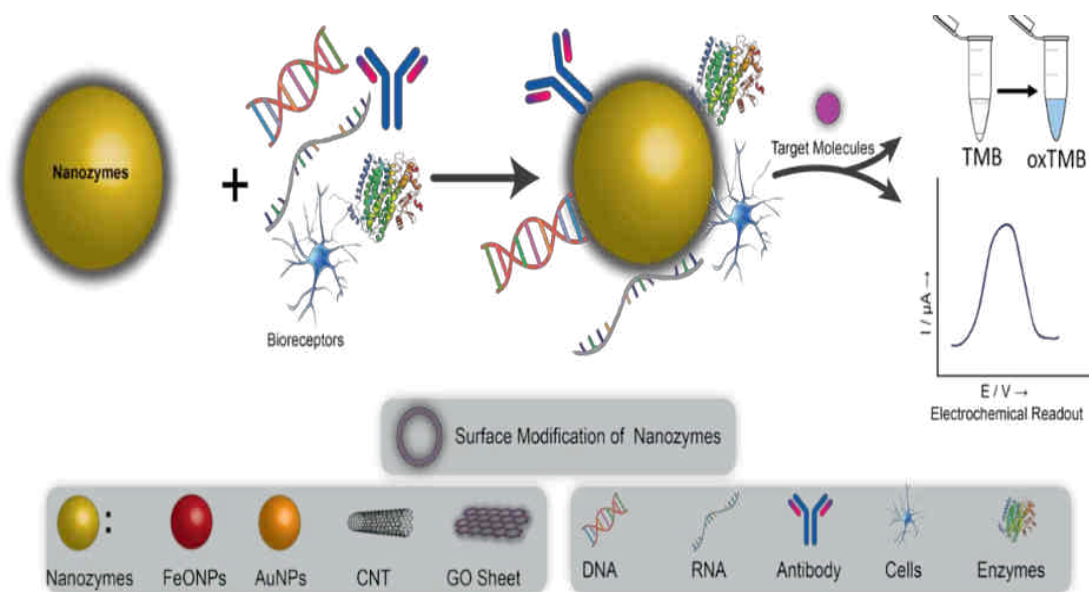


**Figure 1.2** Schematic representation of the nanozyme’s catalytic activities and its application in the electrochemical biosensor. Nanozymes can be functionalized with a range of receptor probes (e.g., complementary capture probes for DNA and RNA targets, antibodies for proteins, etc.) by conventional surface modification procedures. The probe-functionalized nanozymes can capture the targets (e.g., pathogen, cancer cell, exosome, nucleic acid) via the specific interaction between nanozyme-bound probes and targets. The nanozymes-attached targets can then be quantified electrochemically or optically (i.e., naked eye and UV-visible) via an ELISA-type sandwich immunoassay or sandwich hybridization method.

has been solidified as enzyme-mimicking nanomaterials after the demonstration of intrinsic peroxidase-like activities of magnetite ( $\text{Fe}_3\text{O}_4$ ) NPs in 2007 [6-7]. Since then, hundreds of nanomaterials have been reported with enzyme-mimicking properties along with diverse applications. Nanozymes have shown considerable superiorities over natural enzymes due to their high and tunable catalytic activities, ease of modification, large surface area, low cost, and large-scale production. As such, nanozymes are widely regarded as direct alternatives to natural enzymes. **Fig.1.3** summarizes the unique features of nanozymes and their applications in electrochemical sensors.

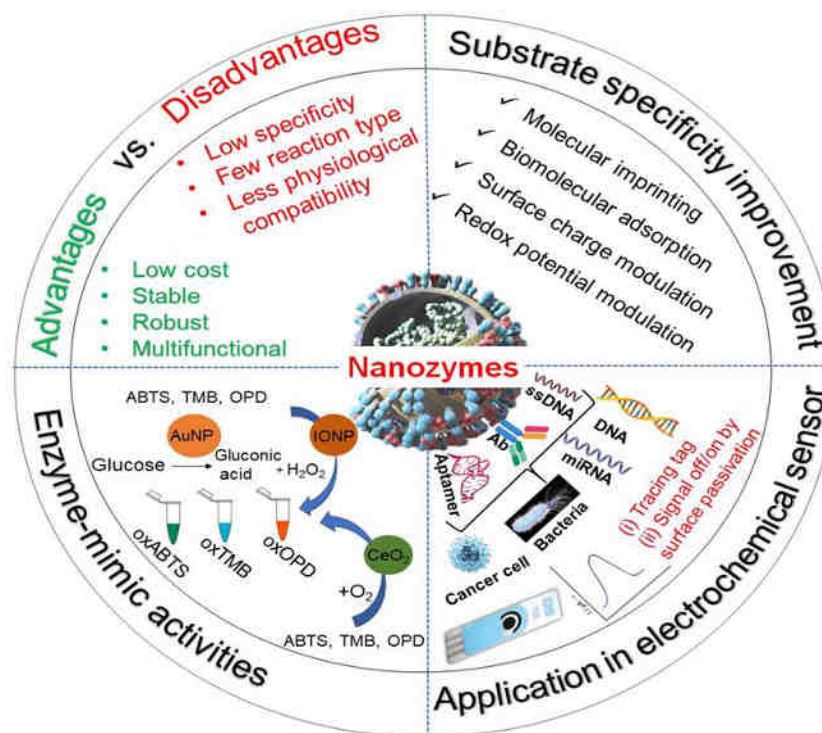


**Figure 1.3** Schematic presentation of the typical enzyme-mimetic activities of nanozymes, their advantages, and limitations compared to natural enzymes, recommended strategies to improve their substrate specificity, and their applications in electrochemical biosensors.

Along with enzyme-mimic activities, optical, electrical, and magnetic properties of certain nanozymes are ideal for most analytical applications. These characteristics greatly facilitate the integration and automation of multiple processes such as separation and detection procedures of molecular targets with immensely high speed, leading to a decrease in the preparatory steps and required time [6,8-9]. In electrochemical biosensors, nanozymes can be used in two ways: (i) as an electrode material for biomarker sensing or (ii) as a tracing tag for signal amplification. As an electrode material, nanozymes have widely been used to fabricate the third and fourth generations of glucose sensors [10] as well as to detect cancer cells [11-12]. High surface area and high-density capture sites of the nanozymes could allow enhanced loading of the electroactive species at their surfaces, resulting in improved electrochemical responses. For example, Wang *et al.* used peroxidase-mimicking graphene-supported ferric porphyrin as a tracing tag for signal

amplification in detecting DNA [13]. High loading of porphyrin on both sides of graphene oxide (GO) offered at attomolar-order of sensitivity.

Tremendous advancements in nanotechnology have contributed significantly to the unprecedented growth and applications of nanozymes in biosensing. The most common nanozymes used in sensing systems include metal NPs (e.g., Au NPs, [14-16] Pt NPs, [16-20] Pd NPs[16-21]), metal oxide NPs (e.g., CeO<sub>2</sub> NPs, CuO NPs, BiFeO<sub>3</sub> NPs, CoFe<sub>2</sub>O<sub>4</sub> NPs), carbon-based nanomaterials (e.g., carbon nanotubes (CNTs), and graphene oxide (GO)). In general, nanozymes can oxidize a variety of chromogenic substrates (e.g., 3,3',5,5'-tetramethylbenzidine (TMB), 2,2'-azino-bis (3-ethylbenzthiazoline-6-sulfonic acid)(ABTS), 3,3'-diaminobenzidine (DAB), and o-phenylenediamine dihydrochloride (OPD)) in the presence of hydrogen peroxide (H<sub>2</sub>O<sub>2</sub>) and produce a distinguishable color. This concept has already been proved useful to detect not only H<sub>2</sub>O<sub>2</sub> but also other biologically relevant molecules like glucose or lactate when it becomes a part of cascade enzymatic reactions or tandem catalysis by a hybrid nanozyme. A hybrid nanozyme can be made through assembling either glucose oxidase (GOx) or oxidase-like nanozymes on the surface of iron oxide nanozyme or with other peroxidase mimics [22]. Integration of two or more nanozymes could improve the catalytic efficiency by enhancing the proximity effect, i.e., the first enzymatic reaction occurs in close (nanoscale) proximity to the second enzyme, thereby overcoming the limitation of diffusion-limited kinetics and intermediate instability [22].

### **Common Nanozymes for Biosensors**

Intense research and investigation have been conducted to reveal the nanozyme activities of various nanostructured materials. Until now, several nanomaterials have been reported to have catalytic activities similar to peroxidase, oxidase, catalase, and superoxide dismutase (SOD). Based on the reaction mechanism, nanozymes can be divided into two main families [8]: (i) oxidoreductase family and (ii) hydrolase family. Oxidoreductase nanozymes catalyze the oxidation reaction, where reductants and oxidants work as electron donors and acceptors, respectively. Over the past several years, graphene and AuNPs-based nanozymes have been demonstrated to possess excellent peroxidase-like activity to catalyze the oxidation of many substrates, such as TMB and ABTS in the presence of H<sub>2</sub>O<sub>2</sub> [8]. It has also been shown that other metallic nanoparticles have

oxidoreductase activities. For example, Tremel *et al.* reported that MoO<sub>3</sub> nanoparticles work as nanozymes for the oxidation of SO<sub>3</sub><sup>2-</sup> to SO<sub>4</sub><sup>2-</sup> under physiological conditions [23]. On the other hand, hydrolase nanozymes catalyze the hydrolysis reaction by cleaving chemical bonds. In this process, a larger molecule dissociates into two smaller molecules. For instance, gold nanoparticles have widely been used as common hydrolase nanozymes to catalyse hydrolysis reactions [24-26].

In terms of the free radical scavenging capability, nanozymes can also be categorized as (i) antioxidants and (ii) pro-oxidants [27]. In biological systems, pro-oxidant induces oxidative stress by producing free radicals. For example, the presence of transition metal can produce hydroxyl radical (HO<sup>•</sup>) by Fenton chemistry [28]. Therefore, certain peroxidase or oxidase involved in the reaction of free radical generation could be regarded as pro-oxidant [27]. On the contrary, antioxidant nanozymes clean up or scavenge free radical by using catalase- or SOD-like activities [27]. SOD-mimetic catalyzes the dismutation of superoxide anions into hydrogen peroxide, which in turn, can be converted to molecular oxygen and water through catalase-like nanozyme. On the other hand, peroxidase-like may convert hydrogen peroxide into a hydroxyl-free radical and oxidized, and produced colored product. Similar colored products may also be produced by oxidase-like nanozyme through direct oxidation of a chromogenic substrate. **Fig. 1.4** summarizes the classification of nanozymes based on both the reaction mechanism and free radical generation/scavenging.

Among the oxidoreductase nanozymes, peroxidase and oxidase-mimicking nanomaterials are mostly explored for electrochemical biosensors. The common nanomaterials with peroxidase mimetics includes metal nanoparticles (AuNPs [29], PdNPs[30]), metal oxides (Fe<sub>2</sub>O<sub>3</sub>[31-32], Au-NPFe<sub>2</sub>O<sub>3</sub>NC [33-34], Fe<sub>3</sub>O<sub>4</sub> MNP [35], CeO<sub>2</sub>/NiO [36], and CuO[37]), core-shell nanostructure (Au@Pt [38]), dendrite (dealloyed-AuNi@pTBA [39], Cu–Co alloy dendrite [40]), carbon-based composite (GO-AuNP [41], His@AuNCs/rGO [42], PtNPs decorated CNT [43]), and metal-organic frameworks (MOFs). Unlike other nanomaterials, MOFs have drawn enormous interest as a new class of nanozymes due to their uniform cavities which are likely to provide biomimetic active centers and enzyme-like pseudo-substrate-binding pockets [44].

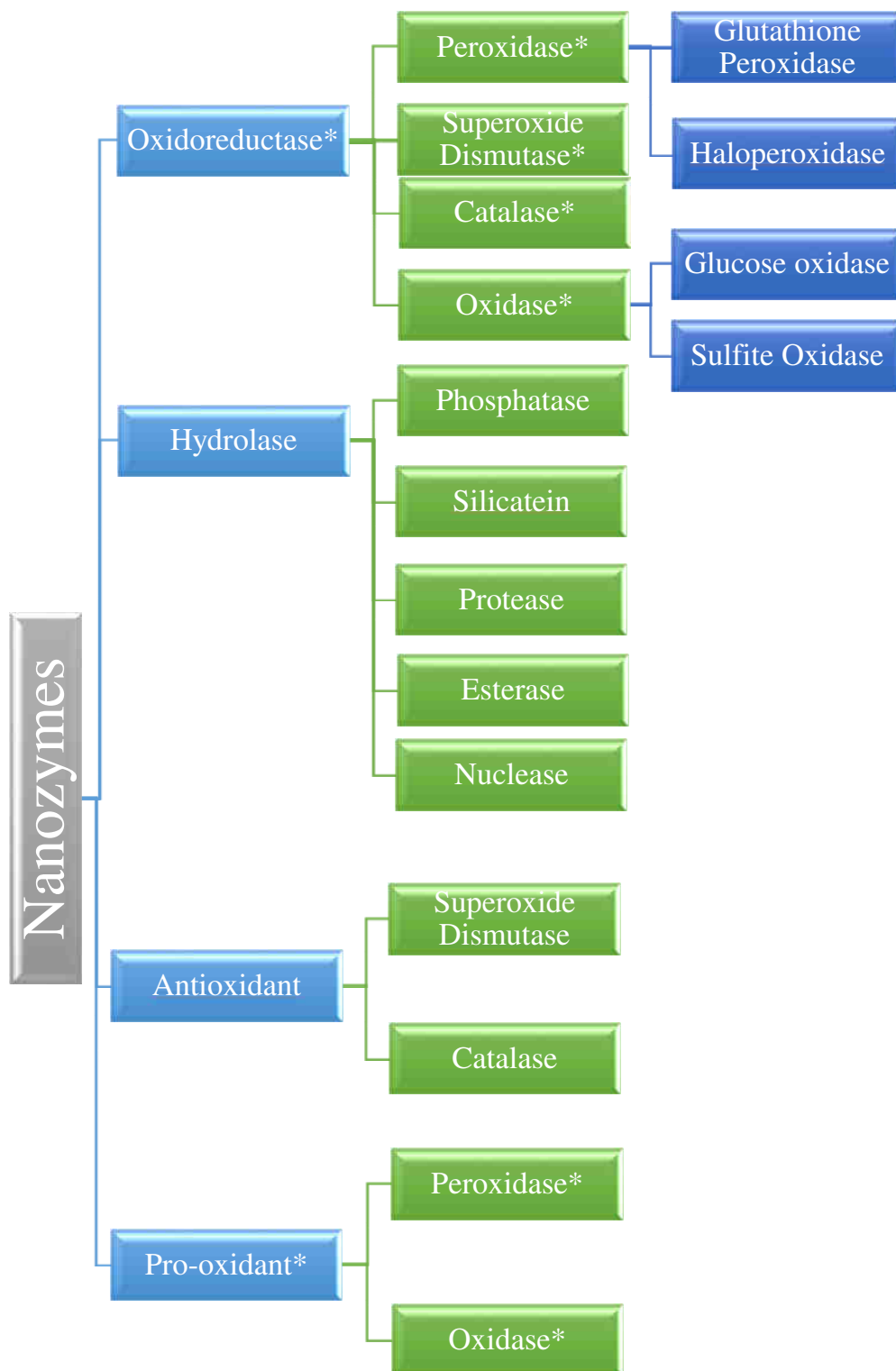


**Figure 1.4** Classification of nanozymes [8, 27-28] (\*) Mark represents the nanozymes commonly used for electrochemical biosensors.



## Nanozyme as a Substitute of HRP

The enzyme-linked immunosorbent assay (ELISA) is the most routinely used technique for detecting and quantifying peptides and antigens. In ELISA, an enzyme-linked primary antibody (direct ELISA) or secondary antibody (indirect or sandwich ELISA) specifically recognizes an antigen. Until now, HRP is the most widely used enzyme reporter in ELISA. It catalyzes the oxidation of TMB in the presence of H<sub>2</sub>O<sub>2</sub> to produce a colorimetric signal, and the intensity of the signal is proportional to the recognized antigen concentration. Despite having many advantages including high substrate turnover, small size, and facile conjugation ability with other biological receptors, HRP suffers several drawbacks. The major drawback associated with HRP is its low tolerance to many preservatives such as sodium azide that inactivates peroxidase activity even at low concentrations. It also undergoes proteolytic degradation, and its enzymatic activity is limited to a narrow range of pH and temperature. Moreover, conventional ELISA lacks sensitivity to detect ultra-low concentrations of biomolecules, especially in the early stages of the diseases [46]. To overcome these limitations, numerous nanostructured materials based nanozymes including MOFs based hybrid nanozymes (described above), have been developed, which are believed to be direct surrogates of HRP [47]. For instance, Ruan *et al.* reported the third generation of 2D GO/Fe-MOF hybrid nanozymes, named nanozyme nest, which was used in a conventional sandwich ELISA to detect benzo[a]pyrene-7,8-diol 9,10-epoxide–DNA adduct (BPDE–DNA), a woodsmoke biomarker found in the blood [48]. This method showed enhanced sensitivity for the oxidation of TMB by dual peroxidase active nanozyme nest (Fe-MOF and GO) (**fig. 1.5**). The value of Michaelis-Menten constant,  $K_m$ , (0.3599mM for nanozyme nest vs. 0.4072 mM for HRP) clearly revealed that nanozyme nest offers higher TMB affinity than that of HRP. Importantly, this hybrid nanozyme reports a lower LOD value compared to that of the HRP, suggesting the better sensitivity of nanozyme nest over HRP in detecting biomolecules [48].

The peroxidase-like activity of nanozyme can be increased via rational design of nanostructured materials as multifunctional nanozymes. Heteroatom doping and sequence of doping are two effective ways to increase the peroxidase-like activity and specificity of nanozymes. For instance, up to a 100-fold increase in catalytic activity

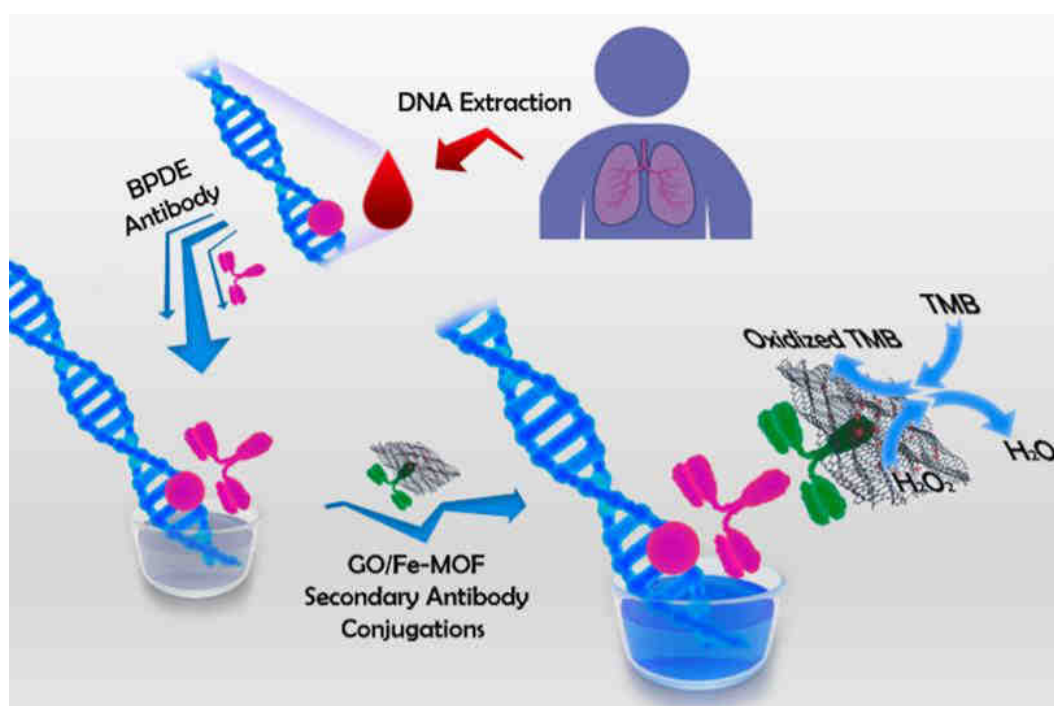


**Figure 1.5** Ultrasensitive ELISA in the determination of DNA by using Nanozyme nest [48].

has been reported for the nitrogen-doped (N-doped)reduced graphene oxide (N-rGO) nanozymes in compared to the reduced graphene oxide (rGO) alone [49]. Density functional theory (DFT) calculation revealed that N-rGO selectively activates H<sub>2</sub>O<sub>2</sub> over O<sub>2</sub> and •O<sub>2</sub><sup>-</sup> and forms stable radical oxygen species adjacent to N-doped sites. These radical oxygen species, in turn, oxidize peroxidase substrates (e.g., TMB) and offer enhanced responses. In another study, Kim *et al.* showed 1000-fold higher catalytic efficacy ( $k_{cat}/K_m$ ) of N and B co-doped reduced graphene oxide (NB-rGO) compared to that of the rGO alone. The catalytic performance of this material is very similar to that of the natural HRP. They have also demonstrated that the sequence of doping of the heteroatoms in the nanostructure materials could significantly affect the catalytic efficacy ( $k_{cat}/K_m$ ) of nanozymes. For example, the catalytic activity of BN-rGO resulted in ~30% lower  $k_{cat}$  compared to that of the NB-rGO [45]. High surface to volume ratio,  $\pi$ - $\pi$  and hydrophobic interactions assist NB-rGO to acquire stronger affinity towards substrates (e.g., TMB) than that of HRP. Due to this property, NB-rGO nanozymes were able to

detect C-reactive protein (CRP), a reliable biomarker for inflammation, tissue damage and cardiovascular disease, via the oxidation-dependent rapid color change of TMB within 3 minutes. In contrast, HRP-based ELISA needs at least 10 minutes. It also shows three-times lower LOD (~5ng/mL of CRP) than that of HRP [45].

### **Applications of Nanozymes in Lateral-flow Immunodetection**

Lateral-flow immunostrip (i.e., nanozyme-strip), a paper-based biosensor, is considered as one of the excellent demonstrations for (point of care) POC testing of biomolecular targets because of its operational simplicity, rapid analysis, naked-eye detection and low cost. Generally, lateral flow biosensors are composed of a sample pad, a conjugate pad, a nitrocellulose membrane containing test and control lines, and an absorbent pad. Many nanozymes have been integrated into this form of assay. For example, Duan *et al.* reported a Fe<sub>3</sub>O<sub>4</sub> magnetic nanoparticle (MNP) based immunochromatographic strip to detect glycoprotein of ebolavirus (EBOV) [50]. In this assay, MNP conjugated detection antibody (anti-EBOV) recognizes EBOV, which in turn forms a sandwich complex with the capture antibody in the test line. After the formation of immunocomplex, oxidation of the peroxidase substrate develops color for visual observation, indicating the presence of EBOV. Pre-processing the sample with immunomagnetic separation offered an additional sensitivity to the EBOV analysis. Overall, this strip demonstrates 100-fold higher sensitivity over the standard colloidal AuNPs based strip with the LOD of 1 ng/mL of glycoprotein (≈240pfu/ml). This method requires less than half an hour [50] and it is sensitive enough to detect Ebola at onset of symptoms.

Recently, porous platinum core-shell nanocatalysts (PtNCs) based immunostrip has been developed to detect p24 HIV capsid protein, a reliable marker for HIV diagnosis (**Fig. 1.6**). In this assay, both target specific antibody-functionalised PtNCs and orthogonally biotinylated camelid antibody fragments (nanobody-biotin) are designed to recognize the distinct regions of target p24 protein [51]. In the presence of a test sample (i.e., serum or plasma contacting p24 protein), p24 protein-bound PtNCs become biotinylated through complexation with the biotinylated nanobody fragments.

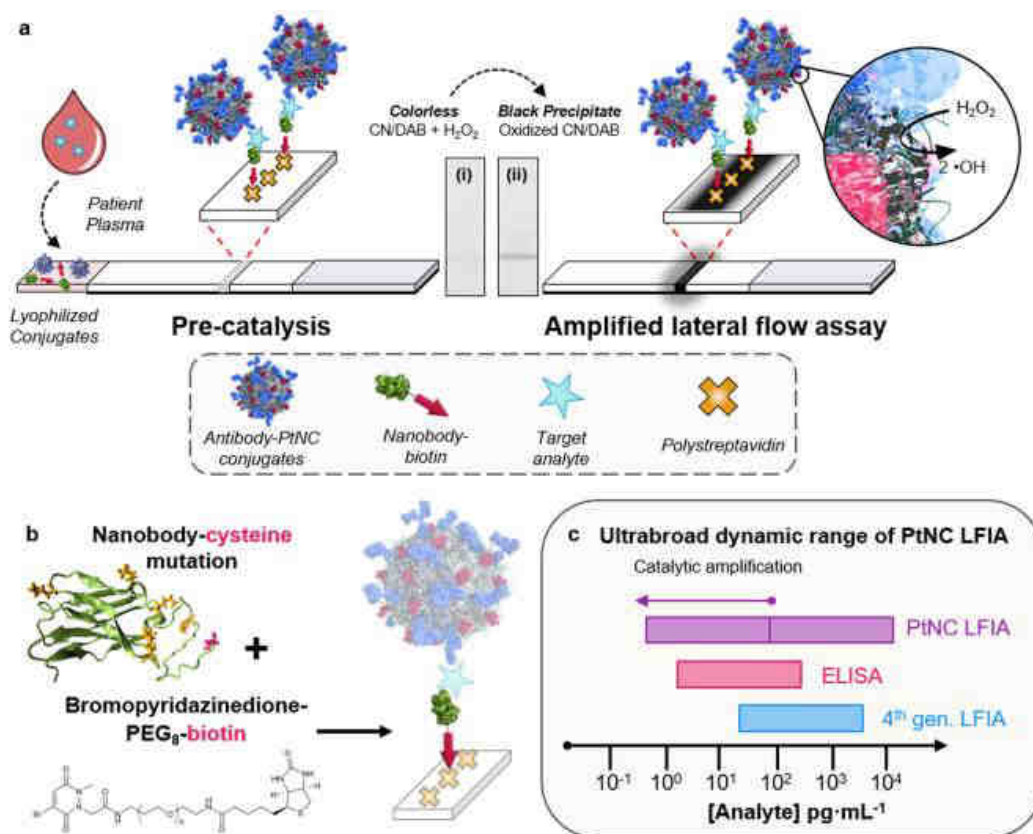


**Figure 1.6(a).** Antibody functionalized Pt nanocatalysts (PtNCs) and biotinylated nanobody. **(b)** Site-selective chemical modification of a nanobody with an exposed cysteine mutation (red), where lysine residues are highlighted in orange on the structural model (left and cartoon of oriented elements at the streptavidin test line). **(c)** Comparison of dynamic ranges of 4<sup>th</sup> generation LIFA, ELISA and PtNC LIFA. Reprinted from Ref [51].

At the polystreptavidin-coated test line, rapid high affinity biotin-streptavidin binding enables a target dependent deposition of biotinylated p24 protein-bound PtNCs complex. PtNCs bound at the test line catalyze the oxidation of 4-chloro-1-naphthol/3,3'-diaminobenzidine, tetrahydrochloride (CN/DAB) substrate in the presence of H<sub>2</sub>O<sub>2</sub> producing an insoluble black product that is clearly visible with the naked eye. This method allows the detection of acute-phase HIV in clinical human plasma samples in under 20 min.

## Application of Nanozymes in Colorimetric Sensor

Colorimetric detection of an analyte has the advantage of providing a fast response (color change) to obtain visual observation (naked eye) and subsequent UV-visible quantification. An advantage of naked-eye detection is that it can be employed as a first-pass screening test for rapid diagnosis of diseases. Once positive results are obtained, UV-vis or other quantities measurements (i.e., electrochemical detection) could be performed to quantify the level and severity of diseases to determine the treatment options, management strategy, which could significantly reduce the cost and time associated with the disease diagnosis and management. This feature of colorimetric sensors makes it suitable for developing rapid and inexpensive screening tools in the fields of medicine (i.e., detection of disease-specific molecules, proteins, and cells), biotechnology, and environmental sciences. As peroxidase mimic nanozyme can oxidise chromogenic substrates (e.g., TMB, ABTS, and OPD) and produce a color in the presence of  $H_2O_2$ , it can directly detect  $H_2O_2$  or other  $H_2O_2$  producing substrates (e.g., glucose).

The Peroxidase-like activity of both the iron oxide nanocomposites (e.g., PDDA coated  $Fe_3O_4$  MNPs [52], mesoporous silica encapsulated  $Fe_3O_4$  MNPs [53],  $Fe_3O_4$ -GO composites [54],  $CeO_2$ -coated hollow  $Fe_3O_4$  nanocomposites [55]), and iron-containing nanomaterials (e.g., assembling hemin in ZIF-8) have widely been used for glucose detection. In all the cases, these materials were combined with GOx and synergistic effect of these two enzymes was the key factor in achieving high sensitivity and superior analytical performance in biomolecular sensing. Again, the sensitivity of glucose detection can also be increased by introducing pores to the iron oxide nanoparticles as it increases the effective catalytic surface area and exposes the metal ions to the surface. For instance, Masud *et al.* detected glucose concentration as low as 0.9  $\mu M$  with the mesoporous iron oxide ( $\gamma-Fe_2O_3$ ), which is ten-times more sensitive than that of the assay with the ZIF-8 (NiPd) nanoflowers [56]. In addition to porosity, oxidation state of the metal could also influence the nanozyme activity.  $LaNiO_3$  perovskite with  $Ni^{3+}$  demonstrated 58-fold and 22-fold higher peroxidase activity than that of perovskite with  $Ni^{2+}$  (e.g., NiO nanoparticles) and  $N^0$  (e.g., Ni nanoparticles) oxidation states, respectively. In addition to porosity, oxidation state could influence the activity of nanozymes.  $LaNiO_3$  perovskite with  $Ni^{3+}$  demonstrated 58~fold and 22~fold higher

peroxidase activity than that of nanoparticle with  $\text{Ni}^{2+}$  (e.g., NiO nanoparticles) and  $\text{Ni}^0$  (e.g., Ni nanoparticles) oxidation states, respectively. The superior activity of these nanozymes facilitated the colorimetric assays of  $\text{H}_2\text{O}_2$ , glucose, and sarcosine [57]. However, as described by Wang *et al.*, the occupancy of  $e_g$  orbitals of the central metal ions may affect the peroxidase-like activity of perovskite nanozyme.

Modulation of peroxidase-like activity of nanozymes via interacting with molecules and ions present in biological systems can be used to detect biomolecular targets. Shah *et al.* used the interaction of AuNPs nanozymes with ATP, ADP, carbonate, sulphate and phosphate ions and the resultant peroxidase-like activity was calculated [58]. It was shown that compared to ADP, phosphate, sulphate and carbonate ions, the incorporation of ATP in the system could significantly enhance the nanozyme activity of AuNPs nanozymes. On the contrary, surface passivation of citrate-capped AuNPs with DNA aptamer inhibits peroxidase substrate to reach the AuNPs surface, thereby attenuates their nanozyme activity. However, when the aptamer binds to its specific targets, it leaves the AuNPs surface and reactivates the nanozyme activity. Based on this phenomenon, Weerathunge *et al.* used AuNP-aptamer transducer to detect murine norovirus with a detection limit of 3 viruses ( $\sim 30$  viruses/mL) within 10 min [59]. As the method can be used for other aptamers (i.e., it is not limited to any specific aptamers), this AuNPs nanozyme-based sensor can be adopted for the detection of other viruses.

### **Application of Nanozymes in Fluorescence Sensor**

A fluorescence sensor consists of the emission of light by a material (fluorophore) after being excited at lower wavelengths and the intensity (or lifetime) of that emission varies with the concentration of the target analyte [60]. In this type of sensor, nanozyme converts a non-fluorescent substrate into a fluorescently active one by catalysing hydrolysis or oxidation reaction. For instance, it was reported that iron and nitrogen-incorporated CNTs that were grown *in situ* on 3D porous carbon foam (denoted as Fe-Phen-CFs) possesses a peroxidase-like activity, which could oxidise terephthalic acid (TA) to the fluorescent product of hydroxyl terephthalate (HTA) in the presence of  $\text{H}_2\text{O}_2$  and can be used as a unique strategy for fluorescence detection of  $\text{H}_2\text{O}_2$  [61]. However, similar to other peroxidase-mimic nanozymes, Fe-Phen-CFs needs to be coupled with GOx. The method

showed excellent sensitivity towards the detection of H<sub>2</sub>O<sub>2</sub> and glucose with a detection limit of 68 nM and 0.19 mM, respectively.

In recent years, the ratiometric fluorescence sensor has gained popularity because of its built-in self-calibration for signal correction, enabling more reliable detection. It also enables more accurate imaging contrast, which often leads to higher detection sensitivity. Ratiometric fluorescence sensor can effectively overcome most of the issues associated with false positive results in traditional fluorescence sensing by introducing another fluorescence emission band to achieve ratiometric signal readouts [62-63]. Very recently, this sensor has been used for the detection of H<sub>2</sub>O<sub>2</sub> and glucose. Briefly, the peroxidase-like activity of ruthenium ion/carbon nitride (Ru-C<sub>3</sub>N<sub>4</sub>) nanosheets catalyses OPD to fluorescent DAB which exhibits emission at 565 nm. Meanwhile, fluorescence emission at 455 nm by Ru-C<sub>3</sub>N<sub>4</sub> decreases or quenches due to the inner filter effect of the generated DAB. Via this method, an excellent sensitivity and selectivity to serum glucose in the presence of common interferences were obtained [63].

### **Applications of Nanozyme in Electrochemical Biosensors**

Over the past several decades, electrochemical biosensors have successfully been used in detecting a range of molecular and cellular biomarkers in the fields of biomedical, biotechnology, and environmental sciences. Therefore, highly sensitive and specific analysis/detection methods are required. To achieve this goal, nanozymes-based catalytic signal amplification strategy for bio molecules detection is one of the promising options.

#### **1.1.1 Genosensor**

Detection of specific nucleic acid (DNA or RNA) sequences has proved their utility in molecular diagnostics, pathogen detection and nanomedicine (nanoscience and nanotechnology) applications in the life and health sciences. It is known that many malignant diseases (e.g., cancer) and pathogenic infections present their signature nucleic acid markers (e.g., circulating tumor DNA, microRNA) in the peripheral circulatory system which can be used as diagnostics, prognostics and therapeutic markers [1,64]. In electrochemical nucleic acid biosensor, sensitivity can easily be enhanced via incorporating catalytic hairpin assembly (CHA) combined with nanozyme label-based redox cycling signal amplification. As outlined by Hun *et al.*, CHA was used to form a

double stranded DNA on a AuNPs modified electrode [65]. Initially, hairpin H1 was immobilized onto AuNPs modified gold electrodes and in the presence of the target DNA, the stem-loop structure of H1 opened due to binding to the target DNA and formed a double strand product with 21 base hybridizations. This triggered in the opening of the second hairpin and formed the partially complementary dsDNA with 39 base hybridizations. This step released the target DNA which could be recycled and used for opening another H1. In the second step, DNA probe functionalized Au@PtNPs nanocatalyst was hybridized with the electrode attached DNA. Au@PtNPs can catalyze the reduction of p-nitrophenol (PNP) to p-aminophenol (PAP) in the presence of NaBH<sub>4</sub>. The generated PAP was electrooxidized to p-quinone imine (PQI) by ferrocenecarboxylic acid (FCA) in the solution. The produced PQI was then reduced back to PAP by NaBH<sub>4</sub>, leading to the redox cycling between PAP and PQI. As a result, an enhanced electrochemical response produced which allows achieving a high sensitivity with 3-orders of magnitude higher than that of AuNP labels alone. This sensor was able to detect as low as 0.3 nM DNA. In another strategy, Ling *et al.* reported an electrochemical DNA quantification method based on nanozyme activity of MOF nanostructure and allosteric switch of hairpin DNA (**Fig.1.7**) [66]. Initially, glassy carbon electrode was functionalized with the streptavidin (SA) aptamer sequence of a hairpin DNA. Due to its loop structure, electrode-bound hairpin DNA is inaccessible to SA attached conjugates. Upon the addition of target DNA, the loop bound to the target sequence and unfolded the stem of hairpin DNA, making it accessible for SA attached conjugates to form a structure with the combinative SA aptamer. The surface-bound activated DNA selectively bound with the SA coated FeTCPP@MOF via specific interaction between SA-aptamer and SA. Nanozyme activity of FeTCPP@MOF was then used to catalyze the oxidation of o-phenylenediamine (o-PD) in the presence of H<sub>2</sub>O<sub>2</sub>. This assay demonstrates a good performance for the detection of DNA with a LOD down to 0.48 fM, the 6-order magnitude linear range, single mismatch differentiation ability, and practical application in complex samples. This study opens up a new direction of functionalized MOF as nanozymes for signal transduction in electrochemical biosensing and shows better enzymatic activities due to their natural enzyme-like metal center and porous nanostructure.



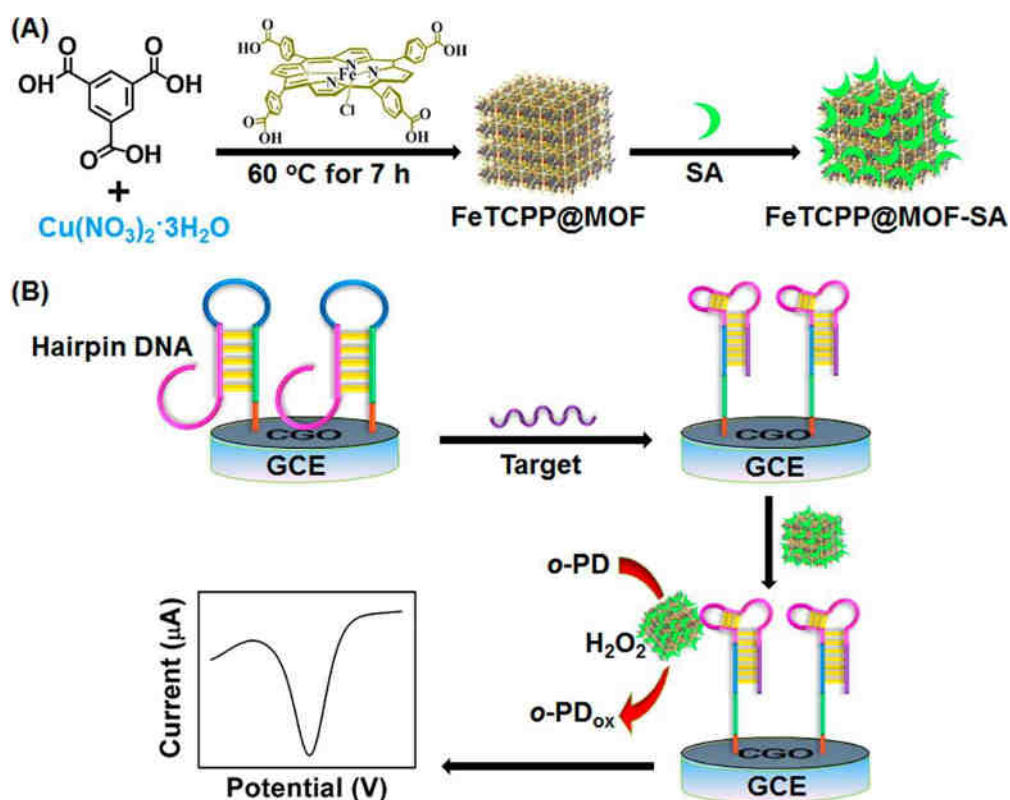


**Figure 1.7**(A) Synthesis of FeTCPP@MOF nanozymes followed by covalent coupling with streptavidin (SA) to form FeTCPP@MOF-SA composite and (B) Target binding initiates allosteric switch of the hairpin probe allows FeTCPP@MOF-SA to recognize the probe and o-PD oxidation provides the electrochemical signal. Reprinted with permission from Ref [66].

MicroRNAs (miRNAs) are small (~17–25 nucleotides long), single-stranded noncoding RNA molecules that suppress the expression of protein-coding genes by translational repression, messenger RNA degradation, or both and involved in early events in disease progression. The nanozyme based electrochemical miRNA sensor provides rapid analysis along with adequate sensitivity. Li *et al.* developed a miRNA sensor to detect miRNA-122 [67], a biomarker of drug-induced liver injury. The nanozyme activity of palladium nanoparticles-based MOF nanohybrids was used. The nanohybrid enzymes were utilized both as nanocarriers to immobilize a large amount of biotin-labeled signal probes (H2) and as tracers to quickly catalyze the oxidation of TMB in the presence of  $\text{H}_2\text{O}_2$ . The target miR-122 was sandwiched between the tracers and electrode-bound thiolated

capture probes (H1). With the help of target-catalyzed hairpin assembly (TCHA), target miR-122 triggered the hybridization of H1 and H2 to further released to initiate the next reaction process resulting in numerous tracers anchored onto the sensing interfaces. Due to dual signal amplification (e.g., target induced signal amplification and TMB oxidation by tracer indicator PdNPs@Fe-MOF), this method could detect miRNA-122 as low as 0.003 fM in human serum [67].

### 1.1.2 Cytosensor

Circulating tumor cells (CTCs) have emerged as valuable tool that can provide mechanistic insights into the tumor heterogeneity, clonal evolution, and stochastic events within the metastatic cascade. They are regarded as one of the most promising biomarkers for early diagnosis of cancer. As a general strategy of CTC detection, antibody- or aptamer-anchored (for aptasensors see Section 1.6.4) nanoprobe are designed to target abnormal and/or over expressed cell surface receptors (proteins) or other cell surface components, including glycans, folic acid, and sialic acid. [64,68] However, the low abundance (1–10 CTCs per 1 billion of blood cells) and inherent fragility of CTCs pose great challenges for CTC detection. To enhance the sensitivity of CTCs analysis, Tian et al. has developed an ultrasensitive electrochemical sensor using reduced graphene oxide/molybdenum disulfide (rGO/MoS<sub>2</sub>) composites modified magnetic glassy carbon electrode (MGCE) as a detector, and aptamer modified magnetic Fe<sub>3</sub>O<sub>4</sub>NPs as dispersible capture agents (**Fig. 1.8**). Cancer cells were attached with the aptamer modified Fe<sub>3</sub>O<sub>4</sub>NPs via aptamer-antigen interaction. The cell-attached conjugates were then magnetically attached onto the rGO/MoS<sub>2</sub> composites-modified electrode. An enhanced electrochemical signal was achieved due to the nanozyme catalytic oxidation of TMB on rGO/MoS<sub>2</sub> composites with Fe<sub>3</sub>O<sub>4</sub>NPs binanozyme surface. The method was able to detect 6 MCF-7 cells per mL which showed significant improvement from their previous report with rGO/AuNPs modified GCE and MUC-1 aptamer modified CuO nanozyme (LOD 27 cells per mL) [37,69]. Very recently, Alizadeh et al. proposed a “signal-off” strategy to detect cancer cells. CuO/WO<sub>3</sub> nanoparticle decorated graphene oxide nanosheets (CuO/WO<sub>3</sub>-GO) were modified with folic acid (FA), which were then absorbed on cancer cells via folic acid targeting ligand. In this strategy, peroxidase like-

activity of CuO/WO<sub>3</sub>-GO was used to oxidise o-phenylenediamine in the presence of H<sub>2</sub>O<sub>2</sub>.

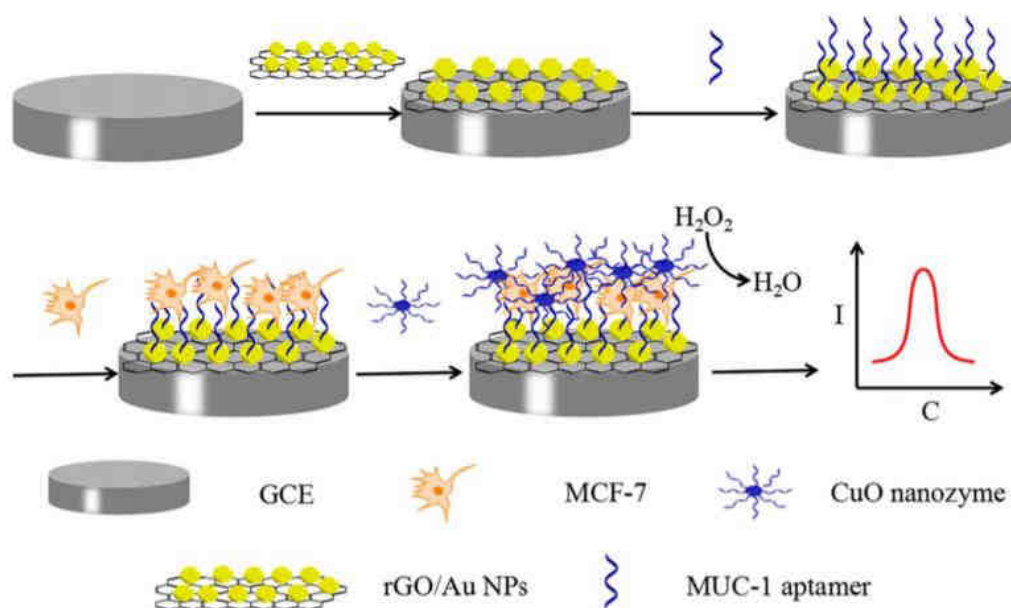


**Figure 1.8** Schematic representation of circulating tumor cell detection using reduced graphene oxide/molybdenum disulfide (rGO/MoS<sub>2</sub>) composites modified magnetic glassy carbon electrode (MGCE) as a detector, and aptamer modified magnetic Fe<sub>3</sub>O<sub>4</sub> NPs as dispersible capture agents. Reproduce from ref [69].

During the interaction between cells and CuO/WO<sub>3</sub>-GO, some amount of H<sub>2</sub>O<sub>2</sub>-OPD system participated in chemical reaction and removed from the electrode, resulting in a decrease in the response signal. Using this principle, the authors successfully achieved a detection limit of 18 cells per mL [11].

### 1.1.3 Immunosensor

The basis of electrochemical immunosensor is the non-covalent interaction between an antigen and antibody to form a sandwich-type architecture on the electrode surface. In a conventional system, enzyme-labelled antibody or antigen amplifies the immune-capture event that can be quantified by voltammetric or amperometric readout method [64,70]. In this regard, successful conjugation of antibody or antigen with enzyme is crucial.

However, most of the standard conjugation, separation and purification methods for enzyme-conjugated antibody or antigens suffer from expensive, time consuming, multistep and laborious procedures. For examples, during the conjugation of antibody with nanozyme, nearly all nanozyme labelled antibody settle down through centrifugation at relatively lower RPM, which adds an extra degree of complexity to the immunosensor fabrication process. Nanozyme-antibody conjugation can be achieved via either electrostatic interactions between them or chemical reactions between the carboxylic acid (-COOH) or anime (-NH<sub>2</sub>) groups of functionalized nanozymes with the -NH<sub>2</sub> or acid – COOH groups of antibodies. For instance, it was reported that -NH<sub>2</sub> groups of secondary antibodies (Ab<sub>2</sub>) electrostatically interacted with Au@Pt (Au-N and Pt-N) of Co<sub>3</sub>O<sub>4</sub>@CeO<sub>2</sub>-Au@Pt nanozymes and used as labels in a sandwich-type electrochemical immunosensor to detect squamous cell carcinoma antigen. This sensor showcased an excellent sensitivity due to the surface area for Ab<sub>2</sub> immobilization and the synergic effect of Co<sub>3</sub>O<sub>4</sub>@CeO<sub>2</sub>-Au@Pt nanozyme towards H<sub>2</sub>O<sub>2</sub> reduction. This assay offered a LOD of 33 fg per mL [71]. Wei et al also published a similar approach for the quantitative detection of hepatitis B surface antigen using MoS<sub>2</sub>@Cu<sub>2</sub>O-Pt nanozymes [72].

Although nanozyme-based sensors are well known for amplifying the readout signals (i.e., “signal-on”), they can equally be useful in generating a noticeable change in electrochemical response in “signal-off” sandwich immunosensing strategies. For instance, Zhang *et al.* developed a “signal-off” sandwich immunosensor to detect  $\alpha$ -fetoprotein. After the successful immune-recognition of FeS<sub>2</sub>-AuNPs-Ab<sub>2</sub> on the electrode surface, FeS<sub>2</sub>-AuNPs nanozymes catalyze 4-chloro-1-naphthol in the presence of H<sub>2</sub>O<sub>2</sub> to form insoluble precipitation. Thus, a reduced differential pulse voltammetric response of electroactive nickel hexacyanoferrate nanoparticles (NiHCFNPs) was observed [73].

Recently Shiddiky group has developed an immunosensor to detect p53 autoantibody in serum and highlighted that the method could be adopted for virtually any type of protein biomarkers. In this method, the surface of a new class of nanozyme, gold-loaded nanoporous Fe<sub>2</sub>O<sub>3</sub> nanocube (Au-NPFe<sub>2</sub>O<sub>3</sub>NC), was modified with IgG and used them as labels in sandwich immunodetection of autoantibody. As shown in (**Fig. 1.9**), abiotinylated p53 antigen was attached to neutravidin-modified screen-printed carbon

electrode via biotin-neutravidin affinity interaction. This electrode was then incubated with the serum sample to capture the target p53 autoantibody present within the sample. The IgG/Au–NPF<sub>2</sub>O<sub>3</sub>NC is used to recognize electrode-bound autoantibodies. The nanozyme activity of IgG/Au–NPF<sub>2</sub>O<sub>3</sub>NC was to adopt an ELISA-based sensing

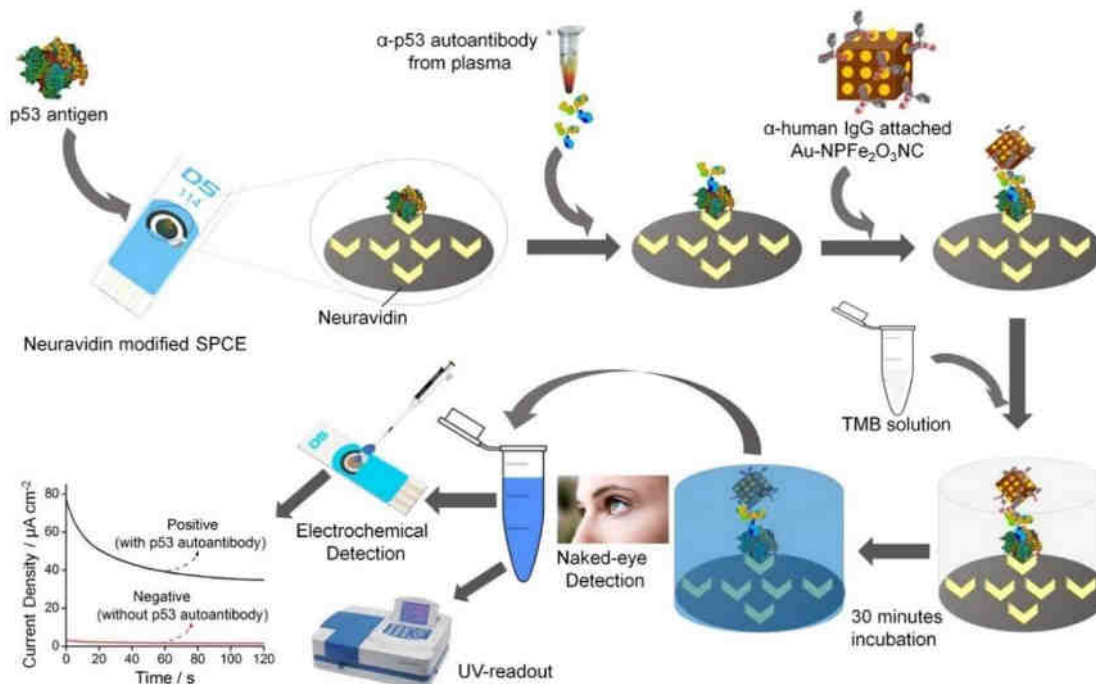


**Figure 1.9** Schematic representation of naked eye and electrochemical detection of p53 autoantibody where target recognition and electrochemical measurement are operated in two separated electrodes. Reprinted from Ref. [33].

protocol where the oxidation of TMB in the presence of hydrogen peroxide was mimicked to generate colored complexes for naked-eye observation and electrochemical detection of target autoantibodies. The electrochemical quantification has been carried out using a new screen-printed electrode. The most attractive feature of this sensor is that the high surface area and enhanced nanozyme activity of the Au–NPF<sub>2</sub>O<sub>3</sub>NC offer enhanced sensitivity (i.e., LOD of 0.08U/mL) in immuno detection of autoantibody in biological fluids. Although this sensitivity is enough to detect p53 autoantibody in the clinical

sample, it cannot obsolete the HRP based sensor having a LOD of 0.02U/mL, previously reported by the same group [33].

### 1.1.4 Aptasensor

Aptamers are ssDNA or RNA molecules synthesized by SELEX (systematized exponentially enriched ligands) with a unique two- or three-dimensional structure that bind to a specific target molecule [75]. Due to their strong affinity (i.e., high specificity

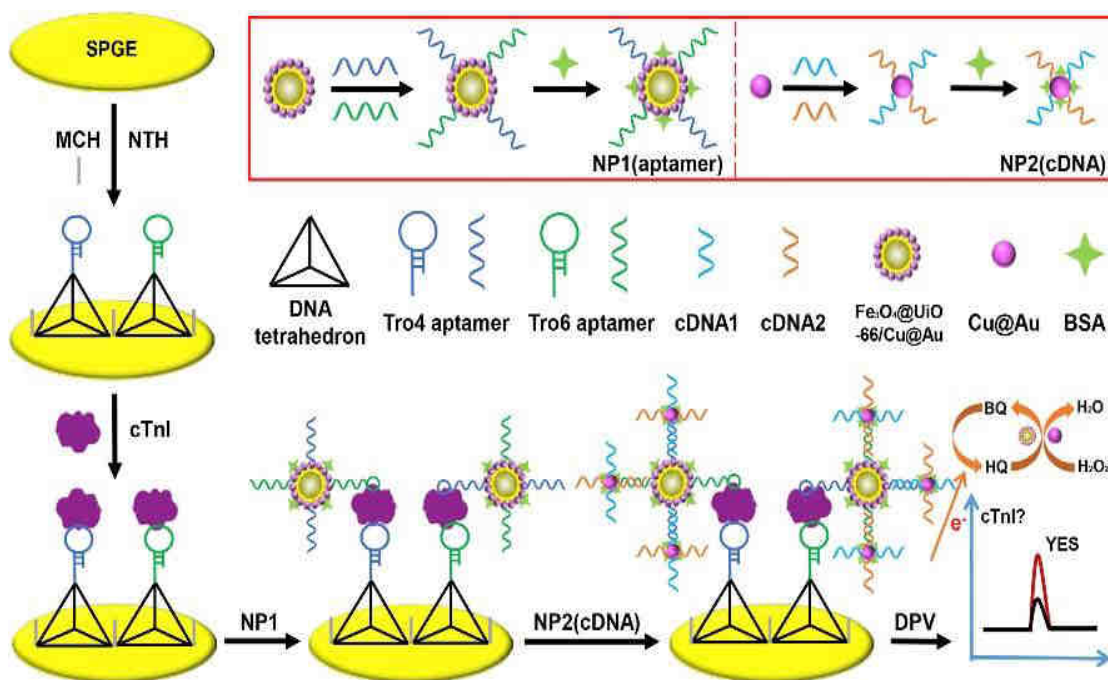


**Figure 1.10** Schematic representation of layer-by-layer (LBL) assembly of the nonenzymatic nanoprobe NP1 (aptamer) and NP2 (cDNA) and NTH-assisted dual-aptamer based electrochemical sensor for detection of cTnI. Reprinted from Ref. [78].

to target), small size, excellent stability, and flexibility in modification, aptamers become a strong competitor of antibody [29-76]. In recent years, nanozyme conjugated aptamers have been used for detecting whole-cell, pathogen [29], and protein [77-79]. Sun *et al.*

developed a method to detect cardiac troponin I (cTnI), a gold standard marker for acute myocardial infarction (AMI) found in the bloodstream, where nanozymes were used for catalytic signal enhancement. This sensor was fabricated by immobilizing nanotetrahedron (NTH) based dual aptamers (Tro4 and Tro6) on the screen-printed gold electrode [78]. After binding of target (cTnI) aptamers modified  $\text{Fe}_3\text{O}_4@\text{UiO-66}/\text{Cu}@Au$  (nanoprobe-1), it was dispensed on the electrode surface to form super-sandwich-like structure. Nanoprobe-1 could oxidize HQ in the presence of  $\text{H}_2\text{O}_2$  through multiple nanozyme activities attributed to  $\text{Fe}_3\text{O}_4@\text{UiO-66}$  and  $\text{Cu}@Au$  (**Fig. 1.10**).

Additionally, attachment of super-sandwich and cDNA (complementary to aptamers) modified  $\text{Cu}@Au$  through hybridization forms a cluster-based nanoprobe, which could further increase the catalytically active sites for the HQ/ $\text{H}_2\text{O}_2$  system, resulting in a more sensitive catalytic response [78]. A more sensitive electrochemical assay for the detection of cTnI was fabricated using co-catalysis of magnetic  $\text{Fe}_3\text{O}_4$  nanocarriers loaded with natural HRP,  $\text{Au}@Pt$  nanozyme and G-quadruplex/hemin DNAzyme (7.5 vs. 16 pg per mL) [80]. In both of the cases, NTH helps to maintain a precise orientation of aptamers on the sensing surfaces, providing native-like microenvironment for cTnI binding.

Recently, gold nanozyme based aptasensors have been developed for detection of pathogens [59]. In 2019, Bansal group developed an electrochemical sensor for the detection of *Pseudomonas aeruginosa* (PA) bacterial pathogen using the nanozyme activity of AuNPs and high affinity and specificity of a PA-specific aptamer (F23) [29,59]. The presence of aptamer inhibits the inherent peroxidase-like activity of GNPs by simple adsorption on to the surface of GNPs. In the presence of target pathogens, the aptamer leaves the AuNPs surface, allowing them to resume their peroxidase-like activity, resulting in oxidation of TMB at screen-printed carbon electrode. The method is sensitive to detect PA with a LOD of  $\sim 60$  CFU per mL in water within 10 min. The authors envisaged that this assay might become a generic platform to detect other molecular and cellular analytes.

### **Synthesis of Common Nanozymes for Biosensing**

Due to the potential applications of nanozymes in electronics [81], therapeutics, optics [82], catalysis [83] and biosensing [84] applications, there has been a demand for the

design and synthesis of nanozymes with high peroxidase-like activities. Over the past few years, many attempts have been made to synthesize nanozymes with well-controlled size, shape, spatial arrangement, and compositions. These methods can be divided into two main categories: top-down and bottom-up approaches. The top-down approach is the solid-state processing of macroscopic materials to nanophasic products. This approach includes mechanical milling, nanolithography, laser ablation, sputtering and thermal decomposition. However, the top-down approach is not suitable to make well-controlled size and shape and may produce many crystallographic defects in the nanostructure. On the contrary, the bottom-up method follows building up of nanostructures through atom-by-atom or cluster-by-cluster or molecule-by-molecule approach. It offers nanomaterials with uniform size, shape, fewer defects and homogeneous chemical compositions. The bottom-up approach mostly includes processes such as sol-gel, reverse micelle, chemical vapour deposition (CVD), pyrolysis, biosynthesis, microwave-assisted, and flow synthesis, and most of these processes refer to as wet chemical synthesis. In the following sections, we highlight the synthesis of metal oxide, metallic and carbon-based nanozymes with different size, shape and morphology using top-down and bottom-up approaches.

### **1.1.5 Synthesis of Metal oxides Nanozymes**

Thermal decomposition (also called thermolysis) is a process where chemical bonds of a compound are subjected to dissociation through thermal energy resulting in the formation of monodispersed nanoparticles in a single step. Usually, an organometallic precursor is heated in a high-boiling point organic solvent in the presence of a suitable surfactant, such as oleic acid, 1-octadecene, 1-tetradecene or oleylamine. As an early attempt to synthesize monodispersed iron oxide nanocrystals, Park *et al.* slowly heated iron-oleate complex in 1-octadecene at different temperatures. They observed that temperature dependence of nucleation and growth kinetics were instrumental in monodisperse nanocrystal formation. They also reported that metal oxide NPs (i.e., Fe<sub>2</sub>O<sub>3</sub>, CoO, MnO, FeO@Fe, and MnFe<sub>2</sub>O<sub>4</sub>) with different sizes could be synthesized by using organic solvents with high boiling points, namely 1-hexadecene and trioctylamine (i.e., these solvents have the boiling point of 274<sup>0</sup>C and 365<sup>0</sup>C respectively). The high yield (>95%) and large-scale production (40g) are two characteristic features that have made this process as state-of-the-art for nanocrystal synthesis [85]. Another study also supported



that high temperature synthesis leads to the increases of the nanoparticle size due to comparatively higher reactivity of the metal complex in the solvent [85-86]. However, the metal oxide NPs with nanozyme activity prepared by this method are usually smaller in size, crystalline and dispersed only in the organic solvent.

The sol-gel process for metal oxides synthesis is a wet chemistry-based technique, which is accomplished at room temperature. This method is comparatively cheaper than other wet chemical methods. In this method, a sol is a stable dispersion of colloidal particles or polymers in a solvent, and a gel consists of a three-dimensional continuous network, which encloses a liquid phase. The sol-gel method involves hydrolysis and condensation of metal alkoxides, leading to the dispersion of metal oxide particles in a sol, followed by drying or gelling through solvent removal or by using a chemical reaction. This method consists of several steps, namely hydrolysis, condensation, drying, and thermal treatment to realize the final product of metal oxide NPs [87-90].

Solvothermal and hydrothermal synthesis methods are other well-established wet chemical methods to produce metal-oxide NPs. These methods are carried out in an autoclave or a Parr bomb at high temperature (100 to 1000<sup>0</sup>C) and high pressure (1 to 10000 bar). The main difference between hydrothermal and solvothermal methods is that water is used as a precursor solvent for hydrothermal synthesis, whereas organic solvents are used in solvothermal synthesis. These methods do not require a protective gas atmosphere and refluxing conditions and are more convenient compared to the coprecipitation and thermal decomposition methods. Metal oxide NPs obtain in these methods are highly pure, selective, reproducible and crystalline. Moreover, the crystalline characteristic of the NPs can be altered by total reaction time. For instance, it was reported that the transformation of hydrothermally produced iron oxide nanozymes from 0D to 3D structure is time-dependent [91]. Li *et al.* applied solvothermal reaction to synthesized metal-ion-doped (such as Sn<sup>4+</sup>, Fe<sup>3+</sup>, Co<sup>2+</sup>, and Ni<sup>2+</sup>) TiO<sub>2</sub> nanocomposites. The size and shape of the TiO<sub>2</sub>NPs were controlled by using lauryl alcohol both as solvent and surfactant for the reaction [92].

Microwave-assisted chemical synthesis process is an alternative wet chemical technique for the synthesis of metal oxides NPs based nanozymes. Recent evidences suggest that this method produced NPs with uniform-size and ultrafine-shape. In a conventional

heating system, it is quite impossible to transfer the heat uniformly to the reactant precursor. In contrast, microwave-assisted synthesis provides uniform heating and thus reduces reaction time by increasing reaction kinetics. This method is safe, convenient and requires less energy for the completion of the reaction because of its fast nucleation and growth rate. Recently, several metal-oxide based nanozymes have been synthesized by using the microwave-assisted method. These include ZnO [93],  $\alpha$ -Fe<sub>2</sub>O<sub>3</sub>,  $\beta$ -Fe<sub>2</sub>O<sub>3</sub>, Fe<sub>3</sub>O<sub>4</sub> [94], CuO [95], Cu<sub>2</sub>O [96], Mn<sub>3</sub>O<sub>4</sub>, MnO<sub>2</sub> [97], TiO<sub>2</sub> [98], and Co<sub>3</sub>O<sub>4</sub> [99]. It is important to note that the phase and shape of the NPs can be altered by the properties of solvents used in the method. Guru *et al* have shown that the synthesis of iron oxide NPs by the microwave-assisted method could be drastically affected by using different glycols [100]. Three different glycols (ethylene glycol, polyethylene glycol and polypropylene glycol) with the same precursor under the same condition, resulted in three NPs with different phases (Fe<sub>3</sub>O<sub>4</sub>,  $\alpha$ -Fe<sub>2</sub>O<sub>3</sub>, and  $\gamma$ -Fe<sub>2</sub>O<sub>3</sub>) and shapes (35, 29.9 and 28.2 nm).

#### **1.1.6 Synthesis of Metallic Nanozymes**

Metallic NPs are synthesized by a range of physical processes, chemical reductions, and biological methods. The commonly used physical processes for the synthesis of metallic NPs include grinding, UV irradiation, microwave irradiation, and laser ablation methods. Chemical reduction is the most widely used technique where metal salts are reduced in the presence of a suitable reducing agent [101-102]. Citrate has been used as a reducing agent for chloroauric acid and silver nitrate to synthesize AuNPs and AgNPs, respectively [103-104]. Metallic NPs produced by this method have the high tendency to aggregate. To stop this tendency, stabilizing agents, such as polyvinyl alcohol, poly vinylpyrrolidone), bovine serum albumin (BSA), citrate and cellulose, are mostly used in the reduction reactions. The size of the NPs can be tuned by changing the ratio of the stabilizing agent and the metal salt [105]. In biological methods, non-toxic and inexpensive microbes are used to produce a variety of metallic NPs with different size, shape and composition. In summary, biological methods are environmentally friendly, whereas chemical reduction methods are hazardous and physical process suffers from high energy input.

### 1.1.7 Synthesis of Carbon-based Nanozymes

In this section, the synthesis of graphene oxide, CNTs, carbon nanodots based nanozymes are discussed. Graphene oxide (GO) is a nonconductive and hydrophilic carbon nanomaterial. In general, synthesis of GO from graphite is a two-step process [106-107]. In the first step, graphite flakes are oxidized to graphite oxide to have oxygen-containing functional groups (*e.g.*, epoxy (C–O–C), hydroxyl (OH), carbonyl (C=O) and carboxyl (R–COOH)) into the basal plane or edge of the graphene sheet. As a result of the oxygen-containing groups, the interlayer distance in GO expands and makes the atomic-thick layers hydrophilic as well. In the second step, oxidized layers can be subjected to the exfoliation under moderate sonication, resulting in releasing GO. In 1859, Brodie first synthesized GO by adding potassium chlorate to a slurry of graphite in the presence of fuming nitric acid. This process needs 3 to 4 days to be completed. In 1898, Staudenmaier improved the Brodie's protocol by adding concentrated sulfuric acid and fuming nitric acid followed by the addition of chlorate in the reaction mixture. This method produces highly oxidized GO. However, these two processes suffer a long reaction time. Most widely used Hummer's method, reported in 1958, avoids this disadvantage where high-quality GO can be produced within 2 h. In this method, graphite is oxidized with  $\text{KMnO}_4$  and  $\text{NaNO}_3$  in concentrated  $\text{H}_2\text{SO}_4$ . Notably, all three methods produce toxic gases:  $\text{ClO}_2$  (g) and/or  $\text{NO}_x$  (g), the former one is explosive. Later, Tour improved the Hummer's method by replacing  $\text{NaNO}_3$  with a mixture of  $9\text{H}_2\text{SO}_4:\text{H}_3\text{PO}_4$ . The reaction mixture was fortified with the doubled amount of  $\text{KMnO}_4$  as compared to Hummer's method. This method does not produce any toxic gas and generates oxidized GO with a more regular carbon framework and larger sheet size [106,108-110]. Over the past several years, GO has widely been used to synthesize different hybrid nanostructured materials to produce a range of GO-based nanozymes. For example, Ruan *et al.* synthesized GO/Fe-MOF nanozyme via mixing the negatively charged GO with the positively charged Fe-MOF. Electrostatic interactions between GO and Fe-MOF hold them together [48]. A similar phenomenon was used for the synthesis of GO-AuNP nanozymes. During the aging step of the synthesis, gold ion was adsorbed on the surface of the GO. This step was followed by a reduction reaction with sodium citrate, resulting in the formation of AuNPs onto the GO (*i.e.*, GO-AuNP hybrid) [41].

There are various methods for the synthesis, purifications, dispersion, and functionalisation of CNT [111]. CNTs are symmetric tubes that are formed from the graphene sheet. The most commonly used methods for synthesizing CNTs are arc discharge [112], laser ablation [113], and chemical vapor deposition (CVD) [114].

These materials offer enormous benefits in real world applications. In particular, they are attractive for uses in bimolecular sensors for environmental and health monitoring [111]. Recent evidences suggest that CNT based materials possess excellent peroxidase-like activities [115]. Qu *et al* synthesised oxygenated-group-enriched carbon nanotubes (o-CNTs) via a one-pot oxidation reflux method [116]. The o-CNTs exhibited enhanced peroxidase-like activity for the catalytic reaction over a broad pH range. It was used to catalyse the formation of hydroxyl radical, killing bacteria efficiently and protecting the tissue against edema and inflammation induced by bacteria infections. Among other CNT based materials, single-walled carbon nanotubes (SWCNT) and multi-walled carbon nanotubes (MWCNT) have widely been used to fabricate metal nanoparticle ( $\text{Fe}_3\text{O}_4$ ,  $\text{ZnO}$ ) or GO based hybrid nanozymes. Compared with their single component, these hybrid materials offered enhanced peroxidase-like activities, presumably resulting from the synergetic effects of metallic nanoparticles or GO and conducting CNT (i.e., SWCNT or MWCNT)

Carbon nanodots (CD) or carbon quantum dots (CQD) are a novel class of carbon nanomaterials with size less than 10 nm but can be as small as 1 nm. These materials have commonly been synthesized by using top-down and bottom-up approaches [117-121]. Each approach has its own advantages and disadvantages. Top-down approaches are widely used for the synthesis of CD due to the adequate amount of raw material, scaled-up production and smooth operation. On the other hand, bottom-up approaches give attractive opportunities to control particle size, shape, and properties. Recently, green synthesis of CD has become more popular than the conventional hydrothermal, solvothermal, electrochemical, and electron-beam lithography methods that usually require toxic chemicals and a large amount of heat energy [122-124]. In green synthesis, the organic precursor is replaced by biomass materials and does not require external energy supply [117,125]. It has been shown that CD, CDQ, doped CD/graphene QDs, and CD/graphene QDs nanocomposites possess peroxidase-like activity. The design,

catalytic process, property study, and bio sensing application of these materials have also been discussed in the literature [115,116,126]. These materials have been used in developing biomolecular sensors for the detection many biologically and environmentally significant targets including glutathione [127], glucose [128], and mercury ions [129].

**Present remarks in the synthesis of nanozymes to approach biomolecule detection:**

It is now well established that the peroxidase-like activity of the nanozymes is mainly dependent on their surface area to volume ratio (i.e., density of the exposed active sites at the surface of the nanozymes) as well as their affinity towards the organic substrates such as TMB and ABTS. The size [130], shape [131], morphology [132], compositions, and surface modification groups [133-134], of the nanozymes can also influence their peroxidase-like activities. The growing number of evidence suggests that size, shape, composition and morphology of the nanostructured materials can be controlled by changing reaction parameters [87,91] precursor amount and volume [135-136], and selecting appropriate synthetic methods and surface modification [137]. Thus, the design and development of advanced nanozymes are emerging topics of research. Among all nanozymes iron oxide nanozymes with peroxidase like activity gain enormous attention due to their biocompatibility, low-cost and unique magnetic properties. Over the past several years, various surface modifications of iron oxide nanozymes *e.g.*, coating with polymers, surfactants, various metallic and non-metallic elements, metal oxides, silica, or even biomolecules, have been reported. These surface modifications increase the stability and dispersibility of nanozymes and also provide an additional capability for further surface functionalization [138]. However, surface modification of iron oxide nanoparticles with target-specific biomolecular probes involves complicated steps and harsh conditions. Therefore, a facile preparation technique of carboxyl group-functionalized iron oxide nanozyme with high catalytic activity and magnetic property is highly desirable to detect disease specific biomarkers.

This research will explore the development of a starch-assisted method for the synthesis of a novel class of carboxyl group functionalized iron oxide nanozymes (C-IONPs) which will follow typical Michaelis-Menten kinetics. Carboxyl group-functionalized iron oxide nanoparticles enable easy immobilization of target-specific biomolecular probes such as antibodies, nucleic acids and aptamers onto their surfaces that will help to improve their

biocompatibility and broadens the scope of their applications in biomolecule detection electrochemically in a simple way. This study is also designed to use C-IONPs as dispersible nano carriers to capture biomolecules from bulk populations and as a nanozymes to generate enzyme catalytic responses for the analysis of biomolecules.

In recent years, exosomes have been used as diagnostic and prognostic markers for a range of diseases, including cancer. Exosomes are nanovesicles released by almost all cell types. This research intends to quantify exosomes from cancer cell line electrochemically using C-IONPs. (In this case, the ovarian cancer cell line OVCAR3 will be used). The assay also will use C-IONPs to avoid using natural enzymes (HRP) for enzymatic reactions that will reduce the assay cost, and this technology will serve the purpose of on-site or (point of care) POC detection.

Recent evidence reveal that quantification of global DNA methylation has emerged as a promising approach for diagnosis and prognosis of cancers. This research will explore liquid biopsy based global DNA methylation analysis applying C-IONPs as a dispersible capture agent, avoiding bisulfate treatment, and will not rely on enzymes for signal generation.

A practical advantage of electrochemical detection will have future implications in translating to cheap assays using single use screen printed electrodes, which is an ideal tool due to their low cost, disposability and design flexibility as compared to traditional electrode materials.

## **Objectives**

The main objectives of the proposed research are:

- i. Synthesis of iron oxide nanoparticles with peroxidase-mimicking activity and magnetic property by adopting facile and eco-friendly gel formation techniques using starch.
- ii. Investigation of enzyme mimicking properties and kinetic parameters along with chemical, structural and morphological characterizations of the synthesized iron oxide nanoparticles.

- iii. Decoration of -COOH group chemically onto magnetic iron oxide nanozymes for isolating bio-molecules (Exosome, and DNA methylation) from body fluid directly.
- iv. Devising nanozyme based electrochemical bio-sensor for the detection of DNA-methylation and exosomes.

## References

- [1] N. Soda, B. H. A. Rehm, P. Sonar, N. T. Nguyen, and M. J. A. Shiddiky, "Advanced liquid biopsy technologies for circulating biomarker detection," *J. Mater. Chem. B*, vol. 7, no. 43, pp. 6670–6704, 2019.
- [2] M. K. Masud *et al.*, "Superparamagnetic nanoarchitectures for disease-specific biomarker detection," *Chem. Soc. Rev.*, vol. 48, no. 24, pp. 5717–5751, Dec. 2019.
- [3] E. O. Blair and D. K. Corrigan, "A review of microfabricated electrochemical biosensors for DNA detection," *Biosens. Bioelectron.*, vol. 134, no. March, pp. 57–67, 2019.
- [4] M. H. Naveen, N. G. Gurudatt, and Y. B. Shim, "Applications of conducting polymer composites to electrochemical sensors: A review," *Appl. Mater. Today*, vol. 9, pp. 419–433, 2017.
- [5] F. Manea, F. B. Houillon, L. Pasquato, and P. Scrimin, "Nanozymes: Gold-nanoparticle-based transphosphorylation catalysts," *Angew. Chemie - Int. Ed.*, vol. 43, no. 45, pp. 6165–6169, 2004.
- [6] J. Wu *et al.*, "Nanomaterials with enzyme-like characteristics (nanozymes): Next-generation artificial enzymes (II)," *Chemical Society Reviews*, vol. 48, no. 4. Royal Society of Chemistry, pp. 1004–1076, Feb. 21, 2019.
- [7] L. Gao *et al.*, "Intrinsic peroxidase-like activity of ferromagnetic nanoparticles," *Nat. Nanotechnol.*, vol. 2, no. 9, pp. 577–583, Sep. 2007.
- [8] Y. Huang, J. Ren, and X. Qu, "Nanozymes: Classification, Catalytic Mechanisms, Activity Regulation, and Applications," *Chem. Rev.*, vol. 119, no. 6, pp. 4357–4412, 2019.
- [9] D. Jiang, D. Ni, Z. T. Rosenkrans, P. Huang, X. Yan, and W. Cai, "Nanozyme: New horizons for responsive biomedical applications," *Chem. Soc. Rev.*, vol. 48, no. 14, pp. 3683–3704, 2019.
- [10] M. Il Kim, Y. Ye, B. Y. Won, S. Shin, J. Lee, and H. G. Park, "A highly efficient electrochemical biosensing platform by employing conductive nanocomposite entrapping magnetic nanoparticles and oxidase in mesoporous carbon foam," *Adv. Funct. Mater.*, vol. 21, no. 15, pp. 2868–2875, 2011.
- [11] N. Alizadeh, A. Salimi, R. Hallaj, F. Fathi, and F. Soleimani, "CuO/WO<sub>3</sub> nanoparticles decorated graphene oxide nanosheets with enhanced peroxidase-like activity for electrochemical cancer cell detection and targeted therapeutics," *Mater. Sci. Eng. C*, vol. 99, no. August 2018, pp. 1374–1383, 2019.
- [12] H. Fang *et al.*, "Enhanced nonenzymatic sensing of hydrogen peroxide released from living cells based on Fe<sub>3</sub>O<sub>4</sub>/self-reduced graphene nanocomposites," *Anal. Methods*, vol. 6, no. 15, pp. 6073–6081, 2014.
- [13] Q. Wang, J. Lei, S. Deng, L. Zhang, and H. Ju, "Graphene-supported ferric porphyrin as a peroxidase mimic for electrochemical DNA biosensing," *Chem. Commun.*, vol. 49, no. 9, pp. 916–918, 2013.



- [14] X. Zheng *et al.*, “Catalytic gold nanoparticles for nanoplasmonic detection of DNA hybridization,” *Angew. Chemie - Int. Ed.*, vol. 50, no. 50, pp. 11994–11998, Dec. 2011.
- [15] W. Luo *et al.*, “Self-catalyzed, self-limiting growth of glucose oxidase-mimicking gold nanoparticles,” *ACS Nano*, vol. 4, no. 12, pp. 7451–7458, Dec. 2010.
- [16] X. Shen, W. Liu, X. Gao, Z. Lu, X. Wu, and X. Gao, “Mechanisms of Oxidase and Superoxide Dismutation-like Activities of Gold, Silver, Platinum, and Palladium, and Their Alloys: A General Way to the Activation of Molecular Oxygen,” *J. Am. Chem. Soc.*, vol. 137, no. 50, pp. 15882–15891, Dec. 2015.
- [17] L. Jin *et al.*, “Ultrasmall Pt Nanoclusters as Robust Peroxidase Mimics for Colorimetric Detection of Glucose in Human Serum,” *ACS Appl. Mater. Interfaces*, vol. 9, no. 11, pp. 10027–10033, 2017.
- [18] Z. Gao, M. Xu, L. Hou, G. Chen, and D. Tang, “Irregular-shaped platinum nanoparticles as peroxidase mimics for highly efficient colorimetric immunoassay,” *Anal. Chim. Acta*, vol. 776, pp. 79–86, 2013.
- [19] R. Polsky, R. Gill, L. Kaganovsky, and I. Willner, “Nucleic acid-functionalized Pt nanoparticles: Catalytic labels for the amplified electrochemical detection of biomolecules,” *Anal. Chem.*, vol. 78, no. 7, pp. 2268–2271, 2006.
- [20] T. Li, Y. Du, and E. Wang, “Polyethyleneimine-functionalized platinum nanoparticles with high electrochemiluminescence activity and their applications to amplified analysis of biomolecules,” *Chem. - An Asian J.*, vol. 3, no. 11, pp. 1942–1948, 2008.
- [21] J. Lan *et al.*, “Colorimetric determination of sarcosine in urine samples of prostatic carcinoma by mimic enzyme palladium nanoparticles,” *Anal. Chim. Acta*, vol. 825, pp. 63–68, May 2014.
- [22] L. Gao, K. Fan, and X. Yan, “Iron oxide nanozyme: A multifunctional enzyme mimetic for biomedical applications,” *Theranostics*, vol. 7, no. 13. Ivyspring International Publisher, pp. 3207–3227, 2017.
- [23] S. H. Hosseini Shokouh *et al.*, “Molybdenum disulfide nanoflake-zinc oxide nanowire hybrid photoinverter,” *ACS Nano*, vol. 8, no. 5, pp. 5174–5181, May 2014.
- [24] R. Bonomi, A. Cazzolaro, A. Sansone, P. Scrimin, and L. J. Prins, “Detection of enzyme activity through catalytic signal amplification with functionalized gold nanoparticles,” *Angew. Chemie - Int. Ed.*, vol. 50, no. 10, pp. 2307–2312, 2011.
- [25] L. Pasquato *et al.*, “N-methylimidazole-functionalized gold nanoparticles as catalysts for cleavage of a carboxylic acid ester,” *Chem. Commun.*, vol. 2, no. 22, pp. 2253–2254, 2000.
- [26] P. Pengo, S. Polizzi, L. Pasquato, and P. Scrimin, “Carboxylate-imidazole cooperativity in dipeptide-functionalized gold nanoparticles with esterase-like activity,” *J. Am. Chem. Soc.*, vol. 127, no. 6, pp. 1616–1617, 2005.

- [27] S. Singh, "Nanomaterials exhibiting enzyme-like properties (Nanozymes): Current advances and future perspectives," *Front. Chem.*, vol. 7, no. FEB, pp. 1–10, 2019.
- [28] A. Rahal *et al.*, "Oxidative Stress, Prooxidants, and Antioxidants: The Interplay," *Biomed Res. Int.*, vol. 2014, p. 19 pages, 2014.
- [29] R. Das, A. Dhiman, A. Kapil, V. Bansal, and T. K. Sharma, "Aptamer-mediated colorimetric and electrochemical detection of *Pseudomonas aeruginosa* utilizing peroxidase-mimic activity of gold NanoZyme," *Anal. Bioanal. Chem.*, vol. 411, no. 6, pp. 1229–1238, 2019.
- [30] J. Wang, X. jiao Chen, K. ming Liao, G. hou Wang, and M. Han, "Pd nanoparticle-modified electrodes for nonenzymatic hydrogen peroxide detection," *Nanoscale Res. Lett.*, vol. 10, no. 1, pp. 1–6, 2015.
- [31] S. Tanaka *et al.*, "Mesoporous Iron Oxide Synthesized Using Poly(styrene-*b*-acrylic acid-*b*-ethylene glycol) Block Copolymer Micelles as Templates for Colorimetric and Electrochemical Detection of Glucose," *ACS Appl. Mater. Interfaces*, vol. 10, no. 1, pp. 1039–1049, 2018.
- [32] R. Bhattacharjee *et al.*, "Porous nanozymes: The peroxidase-mimetic activity of mesoporous iron oxide for the colorimetric and electrochemical detection of global DNA methylation," *J. Mater. Chem. B*, vol. 6, no. 29, pp. 4783–4791, 2018.
- [33] M. K. Masud *et al.*, "Gold-Loaded Nanoporous Ferric Oxide Nanocubes with Peroxidase-Mimicking Activity for Electrocatalytic and Colorimetric Detection of Autoantibody," *Anal. Chem.*, vol. 89, no. 20, pp. 11005–11013, 2017.
- [34] K. Boriachek *et al.*, "Avoiding pre-isolation step in exosome analysis: Direct isolation and sensitive detection of exosomes using gold-loaded nanoporous ferric oxide nanozymes," *Anal. Chem.*, vol. 91, no. 6, pp. 3827–3834, Mar. 2019.
- [35] Z. Zhang, H. Zhu, X. Wang, and X. Yang, "Sensitive electrochemical sensor for hydrogen peroxide using Fe<sub>3</sub>O<sub>4</sub> magnetic nanoparticles as a mimic for peroxidase," *Microchim. Acta*, vol. 174, no. 1, pp. 183–189, 2011.
- [36] J. Mu, X. Zhao, J. Li, E. C. Yang, and X. J. Zhao, "Coral-like CeO<sub>2</sub>/NiO nanocomposites with efficient enzyme-mimetic activity for biosensing application," *Mater. Sci. Eng. C*, vol. 74, pp. 434–442, 2017.
- [37] L. Tian *et al.*, "Copper (II) oxide nanozyme based electrochemical cytosensor for high sensitive detection of circulating tumor cells in breast cancer," *J. Electroanal. Chem.*, vol. 812, no. August 2017, pp. 1–9, 2018.
- [38] K. Shim *et al.*, "Au decorated core-shell structured Au@Pt for the glucose oxidation reaction," *Sensors Actuators, B Chem.*, vol. 278, no. August 2018, pp. 88–96, 2019.
- [39] M. H. Naveen, N. G. Gurudatt, H. B. Noh, and Y. B. Shim, "Dealloyed AuNi Dendrite Anchored on a Functionalized Conducting Polymer for Improved Catalytic Oxygen Reduction and Hydrogen Peroxide Sensing in Living Cells," *Adv. Funct. Mater.*, vol. 26, no. 10, pp. 1590–1601, 2016.

- [40] H. B. Noh, K. S. Lee, P. Chandra, M. S. Won, and Y. B. Shim, "Application of a Cu-Co alloy dendrite on glucose and hydrogen peroxide sensors," *Electrochim. Acta*, vol. 61, pp. 36–43, 2012.
- [41] G. H. Jin *et al.*, "Graphene oxide-gold nanozyme for highly sensitive electrochemical detection of hydrogen peroxide," *Sensors Actuators, B Chem.*, vol. 274, no. March, pp. 201–209, 2018.
- [42] L. Liu *et al.*, "Enhanced His@AuNCs oxidase-like activity by reduced graphene oxide and its application for colorimetric and electrochemical detection of nitrite," *Anal. Bioanal. Chem.*, vol. 411, pp. 2189–2200, 2019.
- [43] A. Umar, S. Kim, R. Kumar, H. Algarni, and M. S. Al-Assiri, "Platinum nanoparticles decorated carbon nanotubes for highly sensitive 2-nitrophenol chemical sensor," *Ceram. Int.*, vol. 42, no. 7, pp. 9257–9263, 2016.
- [44] L. Cui, J. Wu, J. Li, and H. Ju, "Electrochemical Sensor for Lead Cation Sensitized with a DNA Functionalized Porphyrinic Metal-Organic Framework," *Anal. Chem.*, vol. 87, no. 20, pp. 10635–10641, 2015.
- [45] M. S. Kim *et al.*, "N- and B-Codoped Graphene: A Strong Candidate to Replace Natural Peroxidase in Sensitive and Selective Bioassays," *ACS Nano*, vol. 13, no. 4, pp. 4312–4321, 2019.
- [46] C. Li, Y. Yang, D. Wu, T. Li, Y. Yin, and G. Li, "Improvement of enzyme-linked immunosorbent assay for the multicolor detection of biomarkers," *Chem. Sci.*, vol. 7, no. 5, pp. 3011–3016, 2016.
- [47] M. Liang and X. Yan, "Nanozymes: From New Concepts, Mechanisms, and Standards to Applications," *Acc. Chem. Res.*, vol. 52, no. 8, pp. 2190–2200, Aug. 2019.
- [48] X. Ruan *et al.*, "2D Graphene Oxide/Fe-MOF Nanozyme Nest with Superior Peroxidase-Like Activity and Its Application for Detection of Woodsmoke Exposure Biomarker," *Anal. Chem.*, vol. 91, no. 21, pp. 13847–13854, 2019.
- [49] Y. Hu *et al.*, "Nitrogen-Doped Carbon Nanomaterials as Highly Active and Specific Peroxidase Mimics," *Chem. Mater.*, vol. 30, no. 18, pp. 6431–6439, Sep. 2018.
- [50] D. Duan *et al.*, "Nanozyme-strip for rapid local diagnosis of Ebola," *Biosens. Bioelectron.*, vol. 74, pp. 134–141, 2015.
- [51] C. N. Loynachan *et al.*, "Platinum Nanocatalyst Amplification: Redefining the Gold Standard for Lateral Flow Immunoassays with Ultrabroad Dynamic Range," *ACS Nano*, vol. 12, no. 1, pp. 279–288, 2018.
- [52] C. J. Yu, C. Y. Lin, C. H. Liu, T. L. Cheng, and W. L. Tseng, "Synthesis of poly(diallyldimethylammonium chloride)-coated Fe<sub>3</sub>O<sub>4</sub> nanoparticles for colorimetric sensing of glucose and selective extraction of thiol," *Biosensors and Bioelectronics*, vol. 26, no. 2, pp. 913–917, Oct. 2010.

- [53] M. Il Kim, J. Shim, T. Li, J. Lee, and H. G. Park, "Fabrication of Nanoporous Nanocomposites Entrapping Fe<sub>3</sub>O<sub>4</sub> Magnetic Nanoparticles and Oxidases for Colorimetric Biosensing," *Chem. – A Eur. J.*, vol. 17, no. 38, pp. 10700–10707, Sep. 2011.
- [54] Y. Dong *et al.*, "Graphene oxide–Fe<sub>3</sub>O<sub>4</sub> magnetic nanocomposites with peroxidase-like activity for colorimetric detection of glucose," *Nanoscale*, vol. 4, no. 13, pp. 3969–3976, Jun. 2012.
- [55] X. Zhang, C. Ma, K. Wen, and R. Han, "Adsorption of phosphate from aqueous solution by lanthanum modified macroporous chelating resin," *Korean J. Chem. Eng.*, vol. 37, no. 5, pp. 766–775, May 2020.
- [56] M. K. Masud *et al.*, "Nanoarchitected peroxidase-mimetic nanozymes: mesoporous nanocrystalline  $\alpha$ - or  $\gamma$ -iron oxide?," *J. Mater. Chem. B*, vol. 7, no. 35, pp. 5412–5422, Sep. 2019.
- [57] X. Wang *et al.*, "Boosting the peroxidase-like activity of nanostructured nickel by inducing its 3+ oxidation state in LaNiO<sub>3</sub> perovskite and its application for biomedical assays," *Theranostics*, vol. 7, no. 8, pp. 2277–2286, 2017.
- [58] J. Shah, R. Purohit, R. Singh, A. S. Karakoti, and S. Singh, "ATP-enhanced peroxidase-like activity of gold nanoparticles," *J. Colloid Interface Sci.*, vol. 456, pp. 100–107, Oct. 2015.
- [59] P. Weerathunge *et al.*, "Ultrasensitive Colorimetric Detection of Murine Norovirus Using NanoZyme Aptasensor," *Anal. Chem.*, vol. 91, no. 5, pp. 3270–3276, Mar. 2019.
- [60] N. De Acha, C. Elosúa, J. M. Corres, and F. J. Arregui, "Fluorescent Sensors for the Detection of Heavy Metal Ions in Aqueous Media," *Sensors 2019, Vol. 19, Page 599*, vol. 19, no. 3, p. 599, Jan. 2019.
- [61] R. Zhang, S. He, C. Zhang, and W. Chen, "Three-dimensional Fe- and N-incorporated carbon structures as peroxidase mimics for fluorescence detection of hydrogen peroxide and glucose," *J. Mater. Chem. B*, vol. 3, no. 20, pp. 4146–4154, May 2015.
- [62] M. H. Lee, J. S. Kim, and J. L. Sessler, "Small molecule-based ratiometric fluorescence probes for cations, anions, and biomolecules," *Chem. Soc. Rev.*, vol. 44, no. 13, p. 4185, Jul. 2015.
- [63] D. W *et al.*, "Ruthenium Ion-Complexed Carbon Nitride Nanosheets with Peroxidase-like Activity as a Ratiometric Fluorescence Probe for the Detection of Hydrogen Peroxide and Glucose," *ACS Appl. Mater. Interfaces*, vol. 11, no. 32, pp. 29072–29077, Aug. 2019.
- [64] M. K. Masud *et al.*, "Superparamagnetic nanoarchitectures for disease-specific biomarker detection," *Chemical Society Reviews*, vol. 48, no. 24, pp. 5717–5751, Dec. 2019.
- [65] X. Hun, G. Xie, and X. Luo, "Scaling up an electrochemical signal with a catalytic

- hairpin assembly coupling nanocatalyst label for DNA detection,” *Chem. Commun.*, vol. 51, no. 33, pp. 7100–7103, 2015.
- [66] P. Ling, J. Lei, L. Zhang, and H. Ju, “Porphyrin-Encapsulated Metal-Organic Frameworks as Mimetic Catalysts for Electrochemical DNA Sensing via Allosteric Switch of Hairpin DNA,” *Anal. Chem.*, vol. 87, no. 7, pp. 3957–3963, 2015.
- [67] Y. Li, C. Yu, B. Yang, Z. Liu, P. Xia, and Q. Wang, “Target-catalyzed hairpin assembly and metal-organic frameworks mediated nonenzymatic co-reaction for multiple signal amplification detection of miR-122 in human serum,” *Biosens. Bioelectron.*, vol. 102, no. 30, pp. 307–315, 2018.
- [68] C. Zhu, G. Yang, H. Li, D. Du, and Y. Lin, “Electrochemical Sensors and Biosensors Based on Nanomaterials and Nanostructures,” *Analytical Chemistry*, vol. 87, no. 1, pp. 230–249, Jan. 2014.
- [69] L. Tian et al., “An ultrasensitive electrochemical cytosensor based on the magnetic field assisted binanozymes synergistic catalysis of Fe<sub>3</sub>O<sub>4</sub> nanozyme and reduced graphene oxide/molybdenum disulfide nanozyme,” *Sensors and Actuators, B: Chemical*, vol. 260, pp. 676–684, May 2018.
- [70] F. S. Felix and L. Angnes, “Electrochemical immunosensors – A powerful tool for analytical applications,” *Biosens. Bioelectron.*, vol. 102, no. October 2017, pp. 470–478, 2018.
- [71] Y. Li et al., “Ultrasensitive electrochemical immunosensor for quantitative detection of SCCA using Co<sub>3</sub>O<sub>4</sub>@CeO<sub>2</sub>-Au@Pt nanocomposite as enzyme-mimetic labels,” *Biosens. Bioelectron.*, vol. 92, no. January, pp. 33–39, 2017.
- [72] F. Li et al., “Facile synthesis of MoS<sub>2</sub>@Cu<sub>2</sub>O-Pt nanohybrid as enzyme-mimetic label for the detection of the Hepatitis B surface antigen,” *Biosens. Bioelectron.*, vol. 100, no. June 2017, pp. 512–518, 2018.
- [73] L. Zhang, X. Xie, Y. Yuan, Y. Chai, and R. Yuan, “FeS<sub>2</sub>-AuNPs Nanocomposite as Mimicking Enzyme for Constructing Signal-off Sandwich-type Electrochemical Immunosensor Based on Electroactive Nickel Hexacyanoferrate as Matrix,” *Electroanalysis*, vol. 31, no. 6, pp. 1019–1025, 2019.
- [74] S. Yadav et al., “Gold-loaded nanoporous iron oxide nanocubes: A novel dispersible capture agent for tumor-associated autoantibody analysis in serum,” *Nanoscale*, vol. 9, no. 25, pp. 8805–8814, 2017.
- [75] M. Jarczewska, Ł. Górski, and E. Malinowska, “Electrochemical aptamer-based biosensors as potential tools for clinical diagnostics,” *Anal. Methods*, vol. 8, no. 19, pp. 3861–3877, 2016.
- [76] Y. Zhu, P. Chandra, K. M. Song, C. Ban, and Y. B. Shim, “Label-free detection of kanamycin based on the aptamer-functionalized conducting polymer/gold nanocomposite,” *Biosens. Bioelectron.*, vol. 36, no. 1, pp. 29–34, 2012.
- [77] D. Ou, D. Sun, X. Lin, Z. Liang, Y. Zhong, and Z. Chen, “A dual-aptamer-based biosensor for specific detection of breast cancer biomarker HER2 via flower-like

- nanozymes and DNA nanostructures,” *J. Mater. Chem. B*, vol. 7, no. 23, pp. 3661–3669, 2019.
- [78] D. Sun *et al.*, “Electrochemical dual-aptamer-based biosensor for nonenzymatic detection of cardiac troponin I by nanohybrid electrocatalysts labeling combined with DNA nanotetrahedron structure,” *Biosens. Bioelectron.*, vol. 134, no. March, pp. 49–56, 2019.
- [79] Y. Wang *et al.*, “Ultrasensitive sandwich-type electrochemical immunosensor based on dual signal amplification strategy using multifunctional graphene nanocomposites as labels for quantitative detection of tissue polypeptide antigen,” *Sensors Actuators, B Chem.*, vol. 214, pp. 124–131, 2015.
- [80] D. Sun *et al.*, “DNA nanotetrahedron-assisted electrochemical aptasensor for cardiac troponin I detection based on the co-catalysis of hybrid nanozyme, natural enzyme and artificial DNAzyme,” *Biosens. Bioelectron.*, vol. 142, no. May, p. 111578, 2019.
- [81] P. Weerathunge *et al.*, “Ultrasensitive Colorimetric Detection of Murine Norovirus Using NanoZyme Aptasensor,” *Anal. Chem.*, vol. 91, no. 5, pp. 3270–3276, 2019.
- [82] M. E. Franke, T. J. Koplín, and U. Simon, “Metal and Metal Oxide Nanoparticles in Chemiresistors: Does the Nanoscale Matter?,” *Small*, vol. 2, no. 3, pp. 301–301, Mar. 2006.
- [83] S. Brovelli, N. Chiodini, R. Lorenzi, A. Lauria, M. Romagnoli, and A. Paleari, “Fully inorganic oxide-in-oxide ultraviolet nanocrystal light emitting devices,” *Nat. Commun.*, vol. 3, 2012.
- [84] Z. Zhang *et al.*, “Stabilized Copper(I) Oxide Nanoparticles Catalyze Azide-Alkyne Click Reactions in Water,” *Adv. Synth. Catal.*, vol. 352, no. 10, pp. 1600–1604, Jun. 2010.
- [85] V. Urbanova, M. Magro, A. Gedanken, D. Baratella, F. Vianello, and R. Zboril, “Nanocrystalline iron oxides, composites, and related materials as a platform for electrochemical, magnetic, and chemical biosensors,” *Chem. Mater.*, vol. 26, no. 23, pp. 6653–6673, 2014.
- [86] J. Park *et al.*, “Ultra-large-scale syntheses of monodisperse nanocrystals,” *Nat. Mater.*, vol. 3, no. 12, pp. 891–895, 2004.
- [87] S. Sun *et al.*, “Monodisperse MFe<sub>2</sub>O<sub>4</sub> (M = Fe, Co, Mn) Nanoparticles,” *J. Am. Chem. Soc.*, vol. 126, no. 1, pp. 273–279, Jan. 2004.
- [88] J. Xu *et al.*, “Preparation and magnetic properties of magnetite nanoparticles by sol–gel method,” *Journal of Magnetism and Magnetic Materials*, vol. 309, no. 2, pp. 307–311, Feb. 2007.
- [89] H. Cui and W. Ren, “Low temperature and size controlled synthesis of monodispersed  $\gamma$ -Fe<sub>2</sub>O<sub>3</sub> nanoparticles by an epoxide assisted sol–gel route,” *Journal of Sol-Gel Science and Technology 2008 47:1*, vol. 47, no. 1, pp. 81–84, Feb. 2008.

- [90] H. Qi, B. Yan, W. Lu, C. Li, and Y. Yang, "A Non-Alkoxide Sol-Gel Method for the Preparation of Magnetite (Fe<sub>3</sub>O<sub>4</sub>) Nanoparticles," *Current Nanoscience*, vol. 7, no. 3, pp. 381–388, May 2011.
- [91] M. Sangermano *et al.*, "Photo-cured epoxy networks functionalized with Fe<sub>3</sub>O<sub>4</sub> generated by non-hydrolytic sol-gel process," *Macromol. Chem. Phys.*, vol. 214, no. 4, pp. 508–516, Feb. 2013.
- [92] N. M. Abdul Rashid *et al.*, "Structural- and optical-properties analysis of single crystalline hematite ( $\alpha$ -Fe<sub>2</sub>O<sub>3</sub>) nanocubes prepared by one-pot hydrothermal approach," *CrystEngComm*, vol. 18, no. 25, pp. 4720–4732, 2016.
- [93] X. L. Li, Q. Peng, J. X. Yi, X. Wang, and Y. Li, "Near monodisperse TiO<sub>2</sub> nanoparticles and nanorods," *Chem. - A Eur. J.*, vol. 12, no. 8, pp. 2383–2391, Mar. 2006.
- [94] X. Hu, J. Gong, L. Zhang, and J. C. Yu, "Continuous size tuning of monodisperse ZnO colloidal nanocrystal clusters by a microwave-polyol process and their application for humidity sensing," *Advanced Materials*, vol. 20, no. 24, pp. 4845–4850, Dec. 2008.
- [95] W.-W. Wang, Y.-J. Zhu, and M.-L. Ruan, "Microwave-assisted synthesis and magnetic property of magnetite and hematite nanoparticles," *Journal of Nanoparticle Research 2006 9:3*, vol. 9, no. 3, pp. 419–426, Apr. 2006.
- [96] W. W. Wang, Y. J. Zhu, G. F. Cheng, and Y. H. Huang, "Microwave-assisted synthesis of cupric oxide nanosheets and nanowhiskers," *Materials Letters*, vol. 60, no. 5, pp. 609–612, Mar. 2006.
- [97] A. v. Nikamet *al.*, "pH-Dependent Single-Step Rapid Synthesis of CuO and Cu<sub>2</sub>O Nanoparticles from the Same Precursor," *Crystal Growth and Design*, vol. 14, no. 9, pp. 4329–4334, Sep. 2014.
- [98] I. Bilecka, I. Djerdj, and M. Niederberger, "One-minute synthesis of crystalline binary and ternary metal oxide nanoparticles," *Chemical Communications*, no. 7, pp. 886–888, Feb. 2008.
- [99] M. I. Daret *al.*, "Controlled synthesis of TiO<sub>2</sub> nanoparticles and nanospheres using a microwave assisted approach for their application in dye-sensitized solar cells," *J. Mater. Chem. A*, vol. 2, no. 6, pp. 1662–1667, Feb. 2014.
- [100] T. Hyeon, Su Seong Lee, J. Park, Y. Chung, and Hyon Bin Na, "Synthesis of highly crystalline and monodisperse maghemite nanocrystallites without a size-selection process," *J. Am. Chem. Soc.*, vol. 123, no. 51, pp. 12798–12801, Dec. 2001.
- [101] S. Guru, D. Mishra, S. S. Amritphale, and S. Joshi, "Influence of glycols in microwave assisted synthesis of ironoxide nanoparticles," *Colloid Polym. Sci.*, vol. 294, no. 1, pp. 207–213, Jan. 2016.
- [102] D. A. Giljohann, D. S. Seferos, W. L. Daniel, M. D. Massich, P. C. Patel, and C. A. Mirkin, "Gold nanoparticles for biology and medicine," *Angewandte Chemie - International Edition*, vol. 49, no. 19, pp. 3280–3294, Apr. 26, 2010.

- [103] M. Hayat, *Colloidal gold: principles, methods, and applications*. 2012.
- [104] J. Turkevich, P. Stevenson, J. H.-D. of the Faraday, and undefined 1951, “A study of the nucleation and growth processes in the synthesis of colloidal gold,” *pubs.rsc.org*, Accessed: Dec. 12, 2019.
- [105] J. Bonsak, J. Mayandi, A. Thøgersen, E. Stensrud Marstein, and U. Mahalingam, “Chemical synthesis of silver nanoparticles for solar cell applications,” *Phys. Status Solidi Curr. Top. Solid State Phys.*, vol. 8, no. 3, pp. 924–927, Mar. 2011.
- [106] J. W. Guo, T. S. Zhao, J. Prabhuram, and C. W. Wong, “Preparation and the physical/electrochemical properties of a Pt/C nanocatalyst stabilized by citric acid for polymer electrolyte fuel cells,” *Electrochim. Acta*, vol. 50, pp. 1973–1983, 2005.
- [107] S. Sali, H. R. Mackey, and A. A. Abdala, “Effect of graphene oxide synthesis method on properties and performance of polysulfone-graphene oxide mixed matrix membranes,” *Nanomaterials*, vol. 9, no. 5, p. 769, 2019.
- [108] S. Pei and H. M. Cheng, “The reduction of graphene oxide,” *Carbon N. Y.*, vol. 50, no. 9, pp. 3210–3228, 2012.
- [109] M. H. Naveen, H. B. Noh, M. S. Al Hossain, J. H. Kim, and Y. B. Shim, “Facile potentiostatic preparation of functionalized polyterthiophene-anchored graphene oxide as a metal-free electrocatalyst for the oxygen reduction reaction,” *J. Mater. Chem. A*, vol. 3, no. 10, pp. 5426–5433, 2015.
- [110] D. C. Marcano *et al.*, “Improved synthesis of graphene oxide,” *ACS Nano*, vol. 4, no. 8, pp. 4806–4814, 2010.
- [111] P. P. Brisebois and M. Siaj, “Harvesting graphene oxide-years 1859 to 2019: A review of its structure, synthesis, properties and exfoliation,” *J. Mater. Chem. C*, vol. 8, no. 5, pp. 1517–1547, 2020.
- [112] Dimitrios Tasis, Nikos Tagmatarchis, § and Alberto Bianco, and Maurizio Prato, “Chemistry of Carbon Nanotubes,” *Chem. Rev.*, vol. 106, no. 3, pp. 1105–1136, Mar. 2006.
- [113] S. Iijima, “Helical microtubules of graphitic carbon,” *Nature*, vol. 354, pp. 56–58, 1991.
- [114] T. Guo, P. Nikolaev, A. Thess, D. T. Colbert, and R. E. Smalley, “Catalytic growth of single-walled nanotubes by laser vaporization,” *Chem. Phys. Lett.*, vol. 243, no. 1–2, pp. 49–54, Sep. 1995.
- [115] M. José-Yacamán, M. Miki-Yoshida, L. Rendón, and J. G. Santiesteban, “Catalytic growth of carbon microtubules with fullerene structure,” *Appl. Phys. Lett.*, vol. 62, no. 6, pp. 657–659, 1993.
- [116] V. Schroeder, S. Savagatrup, M. He, S. Lin, and T. M. Swager, “Carbon Nanotube Chemical Sensors,” *Chem. Rev.*, vol. 119, no. 1, pp. 599–663, Jan. 2018.



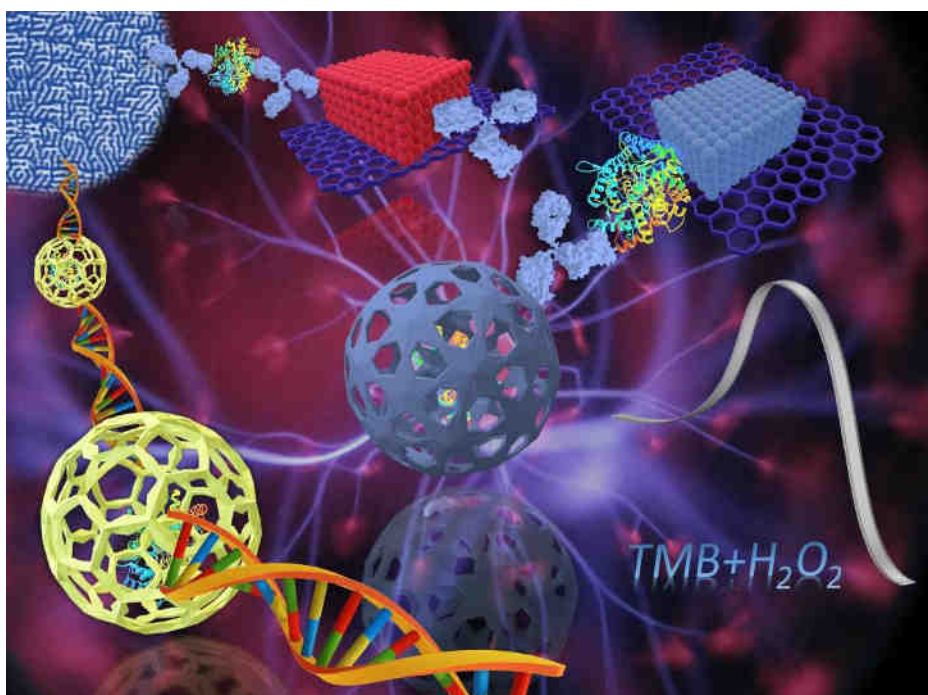
- [117] H. Wang *et al.*, “Unraveling the Enzymatic Activity of Oxygenated Carbon Nanotubes and Their Application in the Treatment of Bacterial Infections,” *Nano Lett.*, vol. 18, no. 6, pp. 3344–3351, Jun. 2018.
- [118] H. Ming *et al.*, “Large scale electrochemical synthesis of high quality carbon nanodots and their photocatalytic property,” *Dalt. Trans.*, vol. 41, no. 31, pp. 9526–9531, Aug. 2012.
- [119] L. Hu *et al.*, “Nitrogen and sulfur co-doped chiral carbon quantum dots with independent photoluminescence and chirality,” *Inorg. Chem. Front.*, vol. 4, no. 6, pp. 946–953, Jun. 2017.
- [120] L. Liet *al.*, “Focusing on luminescent graphene quantum dots: current status and future perspectives,” *Nanoscale*, vol. 5, no. 10, pp. 4015–4039, May 2013.
- [121] H. Li *et al.*, “Water-soluble fluorescent carbon quantum dots and photocatalyst design,” *Angew. Chemie - Int. Ed.*, vol. 49, no. 26, pp. 4430–4434, Jun. 2010.
- [122] H. Li, Z. Kang, Y. Liu, and S.-T. Lee, “Carbon nanodots: synthesis, properties and applications,” *Journal of Materials Chemistry*, vol. 22, no. 46, pp. 24230–24253, Nov. 2012.
- [123] M. X. Gao *et al.*, “A surfactant-assisted redox hydrothermal route to prepare highly photoluminescent carbon quantum dots with aggregation-induced emission enhancement properties,” *Chem. Commun.*, vol. 49, no. 73, pp. 8015–8017, Sep. 2013.
- [124] D. Pan *et al.*, “Cutting sp<sup>2</sup> clusters in graphene sheets into colloidal graphene quantum dots with strong green fluorescence,” *J. Mater. Chem.*, vol. 22, no. 8, pp. 3314–3318, Feb. 2012.
- [125] J. Deng *et al.*, “Electrochemical synthesis of carbon nanodots directly from alcohols,” *Chem. - A Eur. J.*, vol. 20, no. 17, pp. 4993–4999, Apr. 2014.
- [126] S. Y. Lim, W. Shen, and Z. Gao, “Carbon quantum dots and their applications,” *Chem. Soc. Rev.*, vol. 44, no. 1, pp. 362–381, 2015.
- [127] Y. Lv, M. Ma, Y. Huang, and Y. Xia, “Carbon Dot Nanozymes: How to Be Close to Natural Enzymes,” *Chem. - A Eur. J.*, vol. 25, no. 4, pp. 954–960, Jan. 2019.
- [128] M. Shamsipur, A. Safavi, and Z. Mohammadpour, “Indirect colorimetric detection of glutathione based on its radical restoration ability using carbon nanodots as nanozymes,” *Sensors and Actuators B: Chemical*, vol. 199, pp. 463–469, Aug. 2014.
- [129] W. Shi, Q. Wang, Y. Long, Z. Cheng, ... S. C.-C., and undefined 2011, “Carbon nanodots as peroxidase mimetics and their applications to glucose detection,” *pubs.rsc.org*, vol. 47, no. 23, pp. 6695–6697, Jun. 2011.
- [130] Z. Mohammadpour, A. Safavi, and M. Shamsipur, “A new label free colorimetric chemosensor for detection of mercury ion with tunable dynamic range using carbon nanodots as enzyme mimics,” *Chemical Engineering Journal*, vol. 255, pp.

1–7, Nov. 2014.

- [131] J. Lee, H. Jeon, H. Shin, J. K.-C. Communications, and undefined 2012, “Superparamagnetic Fe<sub>3</sub>O<sub>4</sub> nanoparticles–carbon nitride nanotube hybrids for highly efficient peroxidase mimetic catalysts,” *pubs.rsc.org*, vol. 48, pp. 422–424, 2012.
- [132] Nagaprasad Puvvada, P. Kumar Panigrahi, Dhritabrata Mandal, and Amita Pathak, “Shape dependent peroxidase mimetic activity towards oxidation of pyrogallol by H<sub>2</sub>O<sub>2</sub>,” *RSC Adv.*, vol. 2, no. 8, pp. 3270–3273, Mar. 2012.
- [133] C. Ge *et al.*, “Facet Energy versus Enzyme-like Activities: The Unexpected Protection of Palladium Nanocrystals against Oxidative Damage,” *ACS Publ.*, vol. 10, no. 11, pp. 10436–10445, Nov. 2016.
- [134] J. Park *et al.*, “Ultra-large-scale syntheses of monodisperse nanocrystals,” *Nature Materials 2004 3:12*, vol. 3, no. 12, pp. 891–895, Nov. 2004.
- [135] N. Abu Tarboushet *et al.*, “Functional importance of tyrosine 294 and the catalytic selectivity for the Bis-Fe(IV) state of MauG revealed by replacement of this axial heme ligand with histidine,” *Biochemistry*, vol. 49, no. 45, pp. 9783–9791, Nov. 2010.
- [136] J. Xu *et al.*, “Preparation and magnetic properties of magnetite nanoparticles by sol–gel method,” *Journal of Magnetism and Magnetic Materials*, vol. 309, no. 2, pp. 307–311, Feb. 2007.
- [137] N. M. Abdul Rashid *et al.*, “Structural- and optical-properties analysis of single crystalline hematite ( $\alpha$ -Fe<sub>2</sub>O<sub>3</sub>) nanocubes prepared by one-pot hydrothermal approach,” *CrystEngComm*, vol. 18, no. 25, pp. 4720–4732, 2016.
- [138] J. Park *et al.*, “Ultra-large-scale syntheses of monodisperse nanocrystals,” *Nature Materials 2004 3:12*, vol. 3, no. 12, pp. 891–895, Nov. 2004.
- [139] Shouheng Sun *et al.*, “Monodisperse MFe<sub>2</sub>O<sub>4</sub> (M = Fe, Co, Mn) Nanoparticles,” *J. Am. Chem. Soc.*, vol. 126, no. 1, pp. 273–279, Jan. 2003.
- [140] L. Gao *et al.*, “Intrinsic peroxidase-like activity of ferromagnetic nanoparticles,” *Nat. Nanotechnol. 2007 29*, vol. 2, no. 9, pp. 577–583, Aug. 2007.
- [141] W. Wu, Q. He, and C. Jiang, “Magnetic Iron Oxide Nanoparticles: Synthesis and Surface Functionalization Strategies,” *Nanoscale Res. Lett. 2008 311*, vol. 3, no. 11, pp. 397–415, Oct. 2008.

# CHAPTER TWO

Synthesis and Characterization of –COOH-Functionalized Magnetic Iron oxide Nanozymes



## CHAPTER TWO

---

### 2 Synthesis and Characterization of –COOH Functionalized Magnetic Iron oxide Nanozymes

#### 2.1 Introduction

Rationally engineered nanomaterials with intrinsic enzyme-like characteristics, termed as nanozymes, have attracted widespread interest in recent decades as low cost and stable alternatives to naturally occurring enzymes [1-3]. Nanozymes offer several advantages compared to natural enzymes such as high stability, controllable and tunable catalytic activity, robustness even in harsh environments, low cost and easy mass-production, and capability for straightforward functionalization (bioconjugation) [4]. These inherent functional advantages of iron oxide nanomaterials (e.g., Fe<sub>3</sub>O<sub>4</sub> nanoparticles) coupled with recent advances in computational materials design and elucidation of catalytic mechanisms have enabled broad applications of nanozymes in industrial catalysis, neuroprotection, stem cell growth, biosensing, and environmental remediation.

Redox-based nanozymes are one of the most widely researched groups and include oxidases, catalases, superoxide dismutases, and peroxidases [1]. Peroxidase-mimicking nanomaterials (e.g., Fe<sub>3</sub>O<sub>4</sub>NPs) were among the earliest discovered nanozymes that exhibited the intrinsic ability to oxidize peroxidase substrates [3]. Using H<sub>2</sub>O<sub>2</sub> as an oxidizing agent, catalytic oxidation of colorless substrates [3,3',5,5'-tetramethylbenzidine (TMB), diazoaminobenzene, and *o*-phenylenediamine] generates the corresponding colored products and has been widely used in biomolecule sensing studies using both natural horseradish peroxidase (HRP) and peroxidase mimicking nanozymes as the reaction catalysts. Various metallic (e.g., Au, Fe, Ag, Pt), nonmetallic (carbon quantum dots, graphene etc.), and metal -derived (such as metal oxides/hydroxides/sulfides, metal-organic frameworks (MOFs), and multi-metals) nanomaterials with peroxidase mimetic activity have been reported [2]. However, due to their great potential in biomedical applications, iron-based nanomaterials, particularly magnetic Fe<sub>3</sub>O<sub>4</sub>, have been one of the most studied and engineered peroxidase mimetic materials.

The biocompatibility and unique magnetic properties of iron oxide nanoparticles (IONPs) offer several advantages in biomedical applications, particularly biosensing. Peroxidase-mimicking iron oxide can simultaneously provide multiple functions, i.e., capture and magnetic purification of the target analyte from a complex medium, and nanozyme activity for target detection [4]. Detailed analysis of catalytic activity of iron oxide based nanozymes suggests a double displacement mechanism and higher affinity towards TMB with lower affinity towards  $H_2O_2$  compared to HRP [2]. However, despite their huge potential, there are several challenges to their biomedical applications. Precise control of nanoparticles size and shape, the stability and dispersibility under physiological conditions are some of the major challenges that need to be addressed [5]. Over the past several years, various surface modifications of iron oxide nanozymes for example, coating with polymers, surfactants, various metallic and non-metallic elements, metal oxides, silica, or even biomolecules, have been reported [5]. These surface modifications increase stability and dispersibility of nanozymes and also provide an additional capability for further surface functionalization. Over the past several years, synthesis, characterization, and application of a large number of iron oxide based nanozymes such as mesoporous  $Fe_2O_3$  [6], mesoporous  $\gamma$ - &  $\alpha$ - $Fe_2O_3$  [7],  $Fe_3O_4$  NPs [3], platinum decorated  $Fe_3O_4$  [8], Prussian blue modified  $\gamma$ -  $Fe_2O_3$ [9], gold-loaded iron oxide nanocubes [10], Prussian blue- $Fe_2O_3$  [11], and graphene oxide modified- $Fe_2O_3$  [12], have been reported (comprehensively reviewed in refs 13 and 14) [13-14].

Magnetic property of these nanozymes can be used for easy separation of target biomolecules from complex biological systems. Despite promising platform of nanozymes applications in life science and biosensor, nanozyme synthesis generally suffer from technical challenges associated with both low catalytic activities and specificity. In recent year, considerable effort has been applied to the design and controlled fabrication of nanomaterial surface with functional group achieving specific functional properties. However, surface modification of iron oxide nanoparticles with target-specific biomolecular probes involves cumbersome steps and harsh conditions. Thus, developing a facile method of carboxyl group-functionalized iron oxide nanozyme with high catalytic activity and magnetic property would be transformative in the clinical research of biomolecule detection.

Herein, I have introduced an environment friendly gel formation method for the synthesis of a new class of carboxyl group-functionalized magnetic iron oxide nanoparticles (C-IONPs) with peroxidase mimicking activity. The particles were synthesized using a starch-assisted method followed by surface functionalization, and characterized by scanning electron microscopy (SEM), transmission electron microscopy (TEM), dynamic light scattering (DLS), Raman spectroscopy, X-ray diffraction (XRD), and X-ray photoelectron spectroscopy (XPS) analysis. Scanning electron microscopy and transmission electron microscopy analysis confirmed that particles sizes possess in nanoscale with porous shape. X-ray diffraction revealed their inverse spinel crystal structure. X-ray photoelectron spectroscopy analysis and Raman spectroscopy emerged surface functionalization by COOH group.

## **Experimental**

### **2.1.1 Reagents and Materials**

All reagents and chemicals were of analytical grade and used without further purification. Ferric nitrate nonahydrate  $\text{Fe}(\text{NO}_3)_3 \cdot 9\text{H}_2\text{O}$  and starch (soluble) were purchased from Merck (Germany). Dopamine hydrochloride, succinic anhydride, toluene, hydrogen peroxide (30% w/w in  $\text{H}_2\text{O}$ ), acetic acid ( $\text{CH}_3\text{-COOH}$ ), sodium acetate ( $\text{NaCH}_3\text{COO}$ ,  $\geq 99\%$ ) and tris buffer were purchased from Sigma Aldrich. Dimethyl sulfoxide (DMSO) from Chem-Supply (Australia), and TMB  $\geq 98.0\%$  were purchased from Sigma Life Science (Australia). Acetate buffer solution 0.1 M, pH 3.6 was prepared by mixing  $\text{NaCH}_3\text{COO}$  and  $\text{CH}_3\text{COOH}$  stock solutions in appropriate quantities.

### **2.1.2 Synthesis of -COOH Functionalized $\text{Fe}_2\text{O}_3$ Magnetic Nanoparticles (C-IONPs)**

Iron oxide magnetic nanoparticles ( $\text{Fe}_2\text{O}_3$ ) were synthesized by starch assisted gel formation method using  $\text{Fe}(\text{NO}_3)_3 \cdot 9\text{H}_2\text{O}$  as a source of iron and starch as gel forming agent (Fig. 2.1). 50 mL of 0.248 M  $\text{Fe}(\text{NO}_3)_3 \cdot 9\text{H}_2\text{O}$  solution was added slowly to 400 mL of 12% starch solution using a burette, followed by heating at  $70^\circ\text{C}$  under vigorous magnetic stirring. The heating and stirring were continued until the formation of thick reddish gel was observed ( $\sim 9$  h). The gel was dried at  $60^\circ\text{C}$  for 48 h in a hot air oven. The

dried gel was grounded physically in an agate mortar and heat treated at 650°C in a muffle furnace for 4 h in the presence of air. 100 mg of the synthesized Fe<sub>2</sub>O<sub>3</sub> nanoparticles were dispersed in 50 ml DI water using sonication. Then 100 mg of dopamine hydrochloride and 60.65 mg of tris buffer (pH 8.5) were mixed with nanoparticles and subjected to continuous stirring for 24 h at room temperature for polymerization of dopamine hydrochloride to polydopamine (PD). The PD-coated magnetic iron oxide (Fe<sub>2</sub>O<sub>3</sub>@PD) was separated and washed with DI water and ethanol several times.

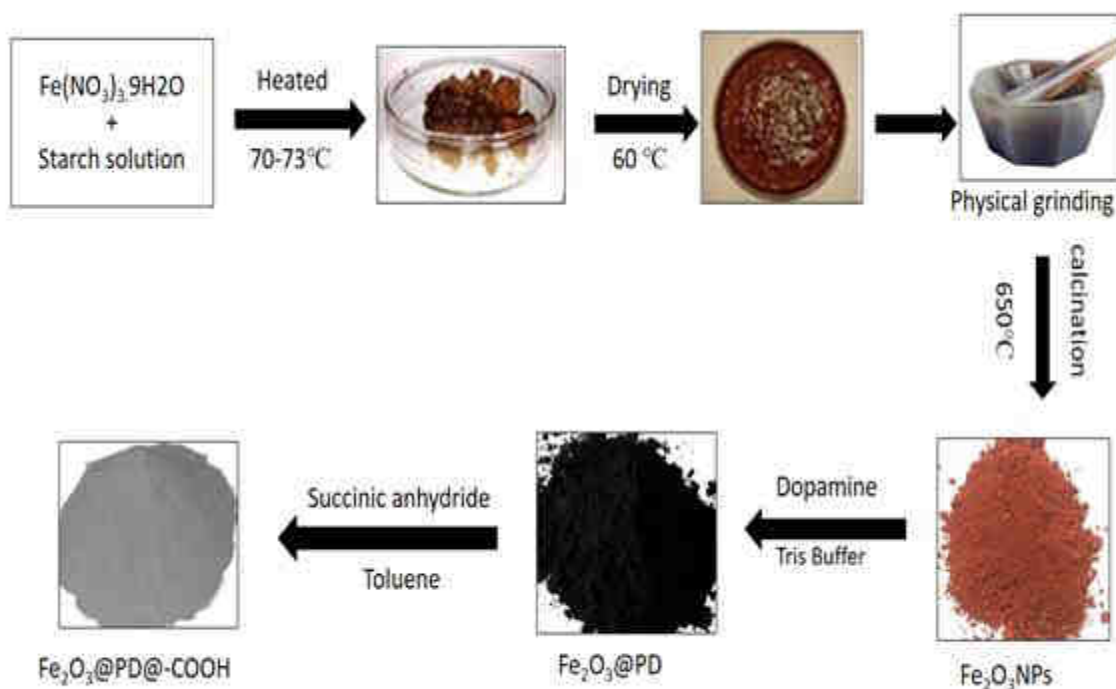


**Figure 2.1** Flowchart diagram describing the workflow for the synthesis of -COOH functionalized iron oxide.

The -COOH group was then introduced on Fe<sub>2</sub>O<sub>3</sub>@PD surface with succinic anhydride. 150 mg of Fe<sub>2</sub>O<sub>3</sub>@PD was dispersed in 100 mL toluene and 750 mg succinic anhydride was added in the suspension under sonication and the mixture was placed in the dark for 2 h. The prepared -COOH functionalized magnetic Fe<sub>2</sub>O<sub>3</sub> particles (C-IONPs) were separated and washed with toluene several times and dried in the ventilating cabinet overnight.

### 2.1.3 Characterization of C-IONPs

The surface morphology and particle size of C-IONPs were investigated using SEM and TEM. A TESCAN MIRA3 FEG-SEM with an in-beam detector was used for SEM analysis while TEM images were obtained with a JEOL 2100 TEM, operated at an accelerating voltage of 200 KV. The surface composition of the samples was analyzed by X-ray photoelectron spectroscopy (XPS). The XPS spectra were measured in AXIS Supra photoelectron spectrometer (Kratos Analytical, UK) with aluminum anode to produce X rays. [Al K $\alpha$  (hV = 1486.7 eV)]. All the samples were drop casted on aluminum foil, which is grounded with the carbon tape to prevent charging. Charge compensation was also used to record the wide and high-resolution data from each sample. The crystalline structure of the synthesized nanoparticles was characterized by X-ray diffraction (XRD), PW3040, X'Pert Pro, Philips, Amsterdam, and The Netherland) using Rigaku CuK $\alpha$  radiation source at 40 kV, 30 mA, within the range of 20°-75° at a rate of 1°/min. The vibrational spectra of molecular bonds of sample were obtained by using inVia<sup>TM</sup> (Renishaw) Raman spectrometer with a laser source of wavelength 785 nm. Hydrodynamic size of C-IONPs was measured by DLS using a DynaPro<sup>®</sup> Plate Reader III (Wyatt Technology, CA, USA) at 25 °C and the results were analyzed by DYNAMICS software (Wyatt Technology). Magnetic measurements were performed using a Mini cryogen-free 5 T system (Cryogenics Ltd. London, UK). Magnetization of the IONPs and C-IONPs was measured using a vibrating-sample magnetometer (VSM) at room temperature (295K) with a sensitivity of 10<sup>-6</sup> emu and a maximum magnetic field of 5 T.

### 2.1.4 Peroxidase-like Activity of C-IONPs

The peroxidase-like activity of C-IONPs was examined through the catalytic oxidation of TMB in the presence of H<sub>2</sub>O<sub>2</sub>. The TMB stock solution was prepared in dimethylsulfoxide (DMSO) while H<sub>2</sub>O<sub>2</sub> solution was prepared in 0.2 M sodium acetate (NaOAc) buffer (pH 3.6). Unless otherwise stated, all C-IONPs/TMB/H<sub>2</sub>O<sub>2</sub> reactions were performed in dark, at room temperature, for 20 min, and in a total reaction volume of 50  $\mu$ L. Initially, five different quantities of the nanozyme, 5, 10, 15, 20, and 25  $\mu$ g were examined to determine the optimal nanoparticle amount for catalytic reaction (**Fig. 2.2**). The reaction was carried out in the presence of final concentrations of H<sub>2</sub>O<sub>2</sub> and TMB as 700 mM and 800  $\mu$ M respectively. For steady-state kinetics analysis, a fixed



concentration of H<sub>2</sub>O<sub>2</sub> (700 mM) was used while TMB concentration was varied between 100 and 1000 μM. similarly, at a fixed TMB concentration of 900 μM, the concentration of H<sub>2</sub>O<sub>2</sub> was varied from 100 to 1000 mM.

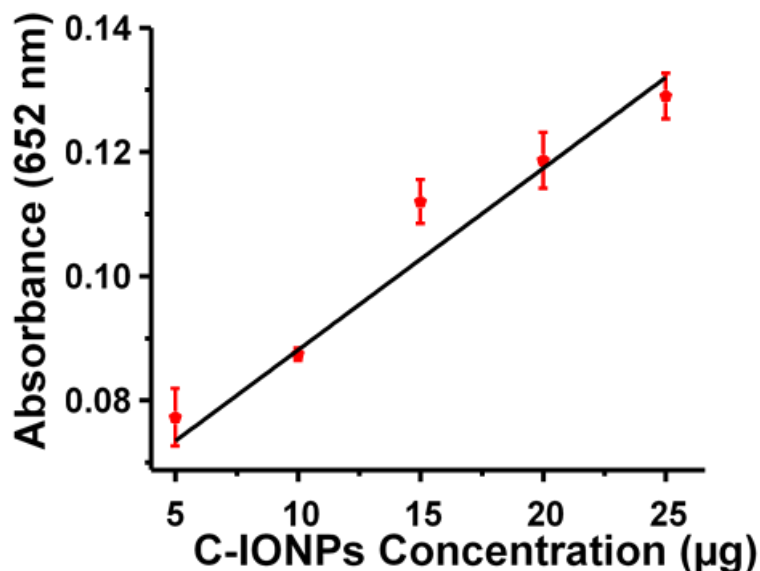


**Figure 2.2** Optimization of C-IONPs concentration. Mean responses of absorbance obtained for the designated concentration of (5, 10, 15, 20, and 25 μg) of C-IONPs. Peroxidase-mimicking activity C-IONPs was performed in the presence of 800 μM TMB and 700 mM H<sub>2</sub>O<sub>2</sub>, in 0.2 M acetate buffer (pH 3.6) at room temperature. UV-vis absorbance was recorded at 652 nm.

A separate set of experiments were conducted to compare the catalytic activity of HRP where two concentrations of TMB 500 μM and 1000 μM were tested in the presence of 700 mM H<sub>2</sub>O<sub>2</sub>, and 0.5 ng HRP (diluted in PBS, pH 7.4). Development of blue color was observed with naked eye, and additionally the intensity (absorbance at 652 nm) of the colored solution was measured using benchtop ELISA plate reader Infinite 200 PRO (Tecan Life Science) in time scan mode (**Fig. 2.3**) The apparent kinetic parameters were estimated based on the simplified Michaelis–Menten and Lineweaver-Burk equations ( $1/V_0 = K_M/V_{Max} / [S] + 1/V_{Max}$ ) as previously described [7-9] where  $V_0$  is the initial velocity,  $K_M$  is the Michaelis constant,  $V_{Max}$  is the maximal reaction velocity, and [S] is the concentration of the substrate [15]. The initial velocity ( $V_0$ ) was converted to molar

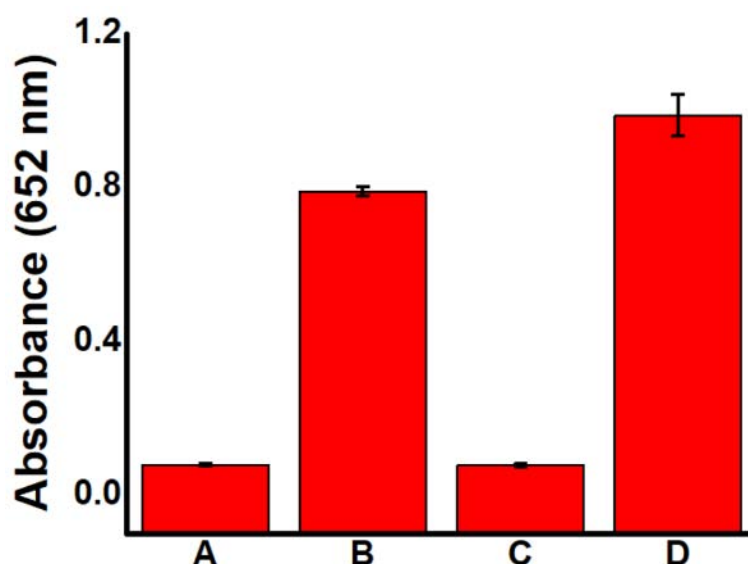


**Figure 2.3** Comparison of nanozyme catalytic activity of C-IONPs with HRP. For (A), TMB = 500  $\mu$ M, H<sub>2</sub>O<sub>2</sub>= 700 mM and Fe<sub>2</sub>O<sub>3</sub>= 15  $\mu$ g; (B), TMB = 500  $\mu$ M, H<sub>2</sub>O<sub>2</sub>= 700 mM and HRP = 0.5 ng; (C), TMB = 1000  $\mu$ M, H<sub>2</sub>O<sub>2</sub>= 700 mM and Fe<sub>2</sub>O<sub>3</sub>= 15  $\mu$ g/ $\mu$ L, and (D), TMB = 1000  $\mu$ M, H<sub>2</sub>O<sub>2</sub>= 700 mM and HRP = 0.5 ng).

change from UV-vis absorbance data using the Beer-Lambert Law,  $A = \epsilon bC$  ( $\epsilon$  is absorbance coefficient,  $b$  is path length of vitric cuvettes, and  $C$  is the molar concentration of oxidation product of TMB) with  $\epsilon = 3.9 \times 10^4 \text{ M}^{-1}\text{cm}^{-1}$  and  $b = 1 \text{ cm}$ . [1,16]

## Results and Discussion

### 2.1.5 Preparation and Electron Microscopic Characterization of C-IONPs

We adopted a novel starch assisted gel formation method to prepare C-IONPs. Most of the currently available iron oxide nanoparticles synthesis methods are either costly or involve high energy consumption and high ecological footprint. In comparison, our method is eco-friendly because it uses low-cost abundant materials like starch for synthesis of iron oxide. (Fig. 2.4) schematically shows the overall process for the formation of C-IONPs. Detailed mechanisms of nanoparticle formation through our starch-assisted method is currently not clear. Earlier reports have suggested that starch captures the Fe<sup>3+</sup> ions into amylose surface, which is a helix-like structure, and allows the formation of Fe-O bond. When high temperature heat treatment is applied in the presence

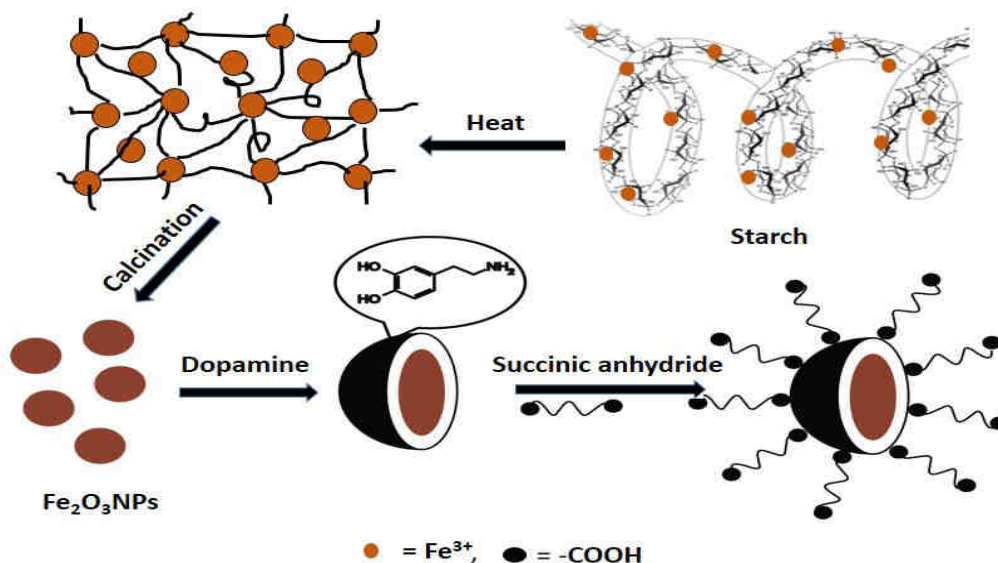


**Figure 2.4** schematic diagram of synthesis and functionalization of iron oxide.

of air, starch molecules are pyrolyzed by removing water and carbon dioxide, and the Fe-O bond is converted to Fe<sub>2</sub>O<sub>3</sub> nanoparticles [17]. It can be assumed that in our method, the nucleation and growth of particles start from ions adsorbed on the helical surface of amylose. These amylose chains, in the presence of water, form a gel upon heating most probably due to the intermolecular and intramolecular hydrogen bonding and formation of coordination bonds with metal ions, thus providing a suitable environment for the formation of oxide with a controlled growth of particles.

In order to functionalize the Fe<sub>2</sub>O<sub>3</sub> nanoparticles surface by -COOH group a mussel-inspired technique was employed Fe<sub>2</sub>O<sub>3</sub> surface was first modified by polydopamine (PD) via self-polymerization of dopamine at basic condition (pH >7.0) [18]. Dopamine can form a polydopamine coating on virtually all types of materials even under wet conditions. Dopamine creates a five-membered metallocycle chelate with Fe<sub>2</sub>O<sub>3</sub> by improved orbital overlap (**Fig. 2.5**) and reduces the steric hindrance of the iron complex [19]. The PD surface has unique chemical characteristics with active amine functional groups, and the presence of amine functional groups on Fe<sub>2</sub>O<sub>3</sub> surface enable further surface modifications. I used succinic anhydride to introduce -COOH groups to the Fe<sub>2</sub>O<sub>3</sub> surface. Succinic anhydride is a five-membered cyclic structure that is highly reactive

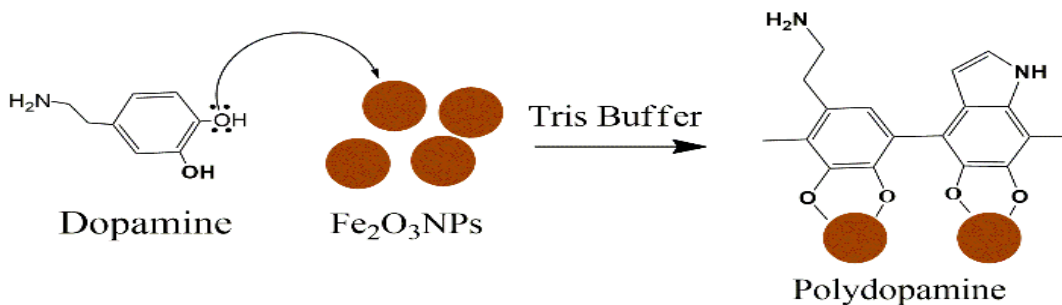


**Figure 2.5** Mechanism of reaction between the iron oxide nanoparticles and dopamine.

towards a nucleophilic functional group like amine. The nucleophile can easily attack at one of the carbonyl groups resulting in opening of the anhydride ring which leads to the formation of a covalent bond and releasing of the other carbonyl group which ultimately generates the  $-\text{COOH}$  on the surface of PD coated  $\text{Fe}_2\text{O}_3$  (**Fig. 2.6**).

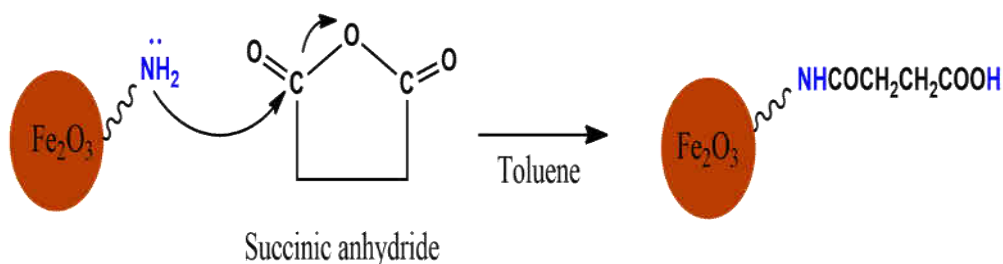


**Figure 2.6** Mechanism of reaction between the amine group of polydopamine and succinic anhydride to produce free carboxyl group on the iron oxide surface.

The morphology and size of the nanoparticles was examined by SEM and high-resolution TEM imaging analysis. Typical SEM and TEM images of  $\text{Fe}_2\text{O}_3$  nanoparticles and C-IONPs are shown in (**Fig 2.7**) and indicate that  $\text{Fe}_2\text{O}_3$  nanoparticles exhibit size in below 100 nm and porous structure and C-IONPs reveal uniform size distribution and spherical shape. The average diameter of the C-IONPs was observed to be approximately 250 nm. After functionalization particle size increased due to the presence of inter molecular bond of  $\text{COOH}$  and  $\text{NH}_2$  functional groups. TEM image of C-IONPs revealed surface functionalization of  $\text{Fe}_2\text{O}_3$  nanoparticles clearly. The bright field TEM image (**Fig. 2.7d**)

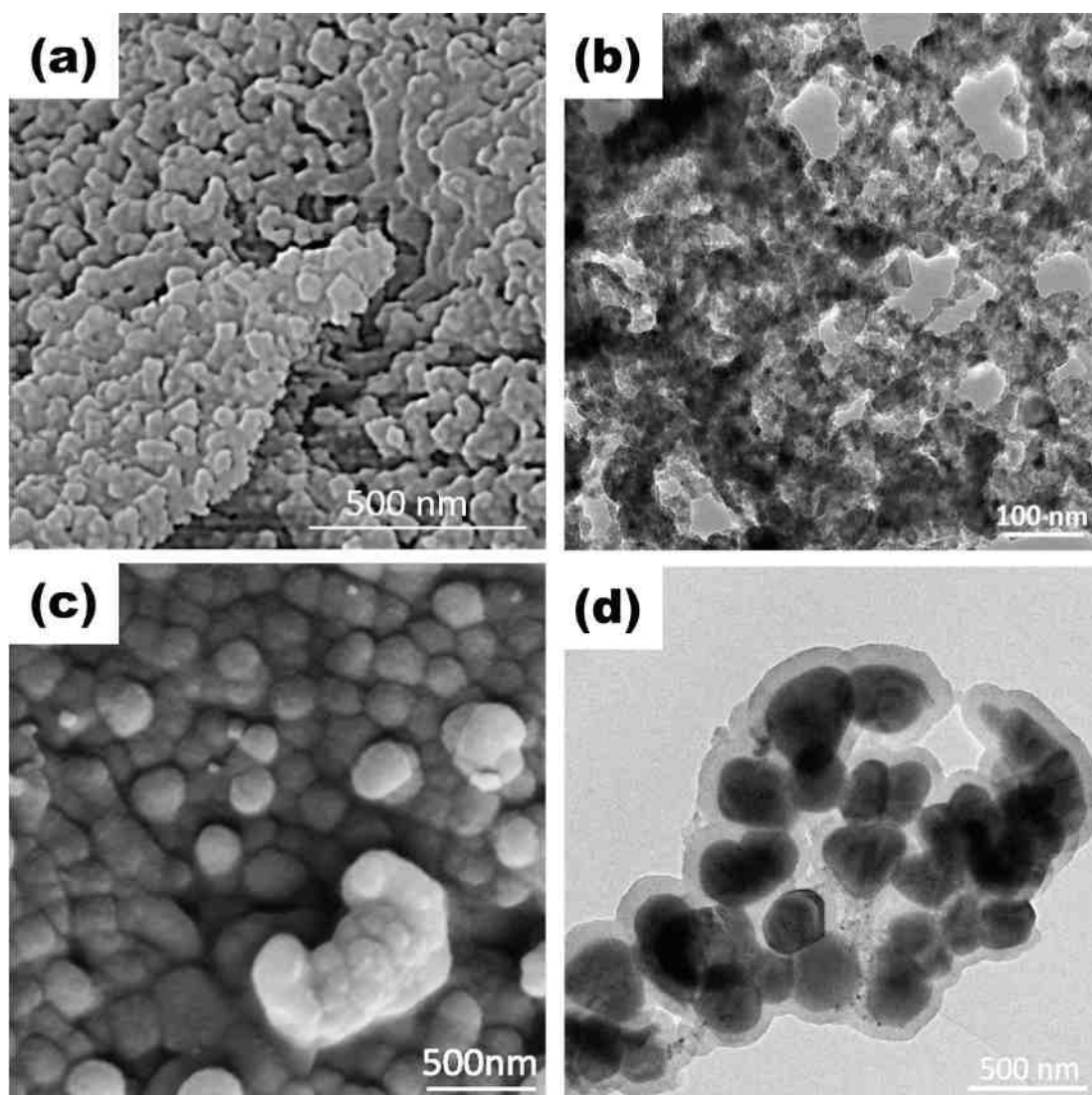


**Figure 2.7** SEM (a) and TEM (b) image of  $\text{Fe}_2\text{O}_3$  nanoparticles, SEM(c) and TEM (d) image of C-IONPs.

shows dark spots around particles, which is caused by the oxidation of  $-\text{COOH}$  ligands by high energy electron beams. To further investigate the process of the functionalization of  $\text{Fe}_2\text{O}_3$  by carbon-based ligand, energy dispersive spectrum was used within TEM to map the selected area for elemental analysis (**Fig. 2.8**). The C  $K\alpha$  signal in Figure 2.8 corroborates our assumption of functionalized  $\text{Fe}_2\text{O}_3$  nanoparticles, with Fe and O as other elements present in the sample.

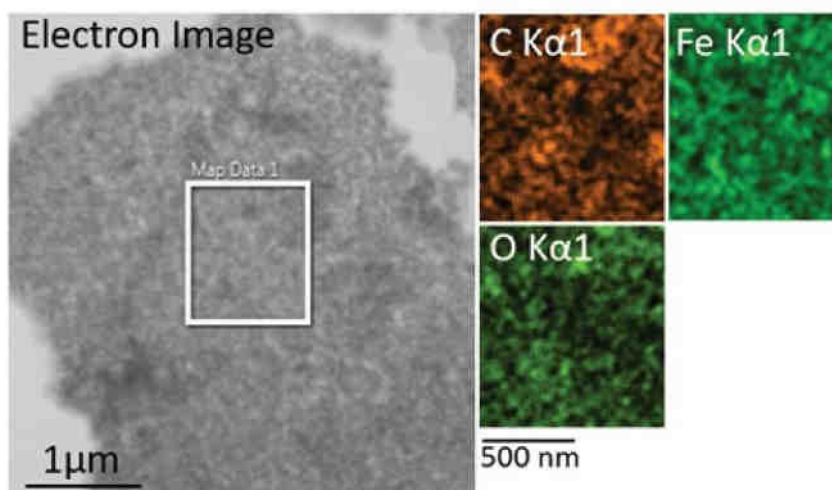


**Figure 2.8** Energy dispersive X ray mapping of elements (C, Fe and O) in sample of carboxyl group-functionalized magnetic  $\text{Fe}_2\text{O}_3$  nanoparticles (i.e., C-IONPs).

The selected area electron diffraction (SAED) indicates the crystalline nature of nanoparticles (**Fig. 2.9**). The d-spacing from the microgram was calculated and was found to be comparable to the d-spacing of a standard  $\text{Fe}_2\text{O}_3$  sample (JCPDS card 39-1346).

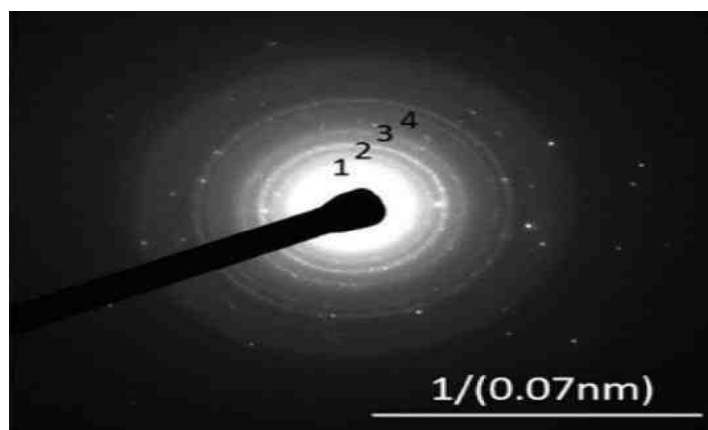


**Figure 2.9** SAED pattern of C-IONPs

A comparison of our nanoparticles with the standard sample along with the hkl indexes is shown in Table 1.

**Table 1** d-space values calculated from electron diffraction pattern and standard atomic spacing obtained of Fe<sub>2</sub>O<sub>3</sub> along with their hkl indexes from JCPDS card (39-1346).

Ring	Calculated d spacing	JCPDS card	Hkl
1	3.39	3.411	211
2	2.52	2.5177	311
3	2.06	2.08	400
4	1.60	1.6073	511

In addition, DLS analysis also revealed uniform hydrodynamic size distribution of the nanoparticles. Hydrodynamic radius of the C-IONPs was found to be  $318.4 \pm 13.58$  nm with a polydispersity of  $41.25\% \pm 6.86$  (**Fig. 2.10**). As is evident from imaging analysis, our novel starch assisted gel formation method was able to provide a precise control over the shape and size of the C-IONPs, similar to the sol-gel method, because gel formation in our method occurs under suitable conditions. Morphological uniformity observed in the imaging analysis not only indicates that the polydopamine capping remains intact during the synthesis and post-synthesis processing, it also shows stability of the nanoparticles against agglomeration. Physicochemical properties of nanoparticles like reactivity, magnetization, catalytic activity etc. are highly dependent on their morphology, and therefore precise control over nanoparticle shape and size is highly important. Moreover, considering the potential application of these nanoparticles for magnetic capture of biomolecules, a spherical shape may provide an additional advantage as spherical magnetic nanoparticles can be magnetized homogeneously in any direction. Fe<sub>2</sub>O<sub>3</sub> nanoparticles tend to aggregate and form large clusters losing their dispersibility in the absence of proper surface coating because of their large surface area and hydrophobic interactions between the nanoparticles. Bare Fe<sub>2</sub>O<sub>3</sub> nanoparticles also tend to lose their magnetism due to oxidation in air. Therefore, various surface coating approaches have been introduced to address this challenge. Surface functionalization of Fe<sub>2</sub>O<sub>3</sub> with organic materials is one of the most common methods used for passivation of

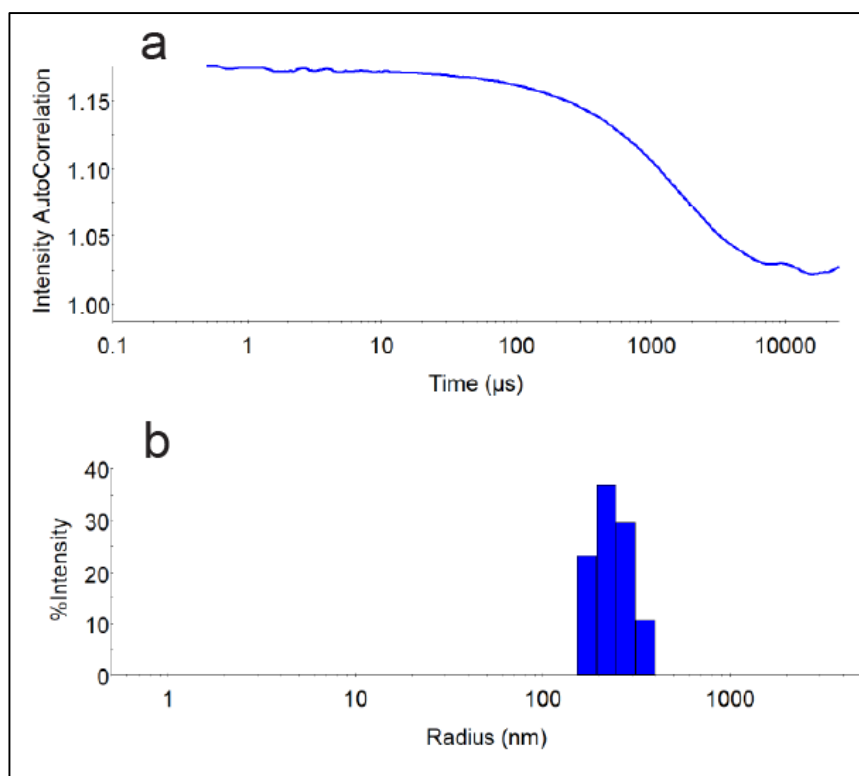


**Figure 2.10** Dynamic Light Scattering (DLS) analysis of C-IONPs. **(a)** Correlation function of C-IONPs **(b)** Hydrodynamic size of C-IONPs. The hydrodynamic radius of nanoparticles was found to be  $318.4 \pm 13.58$  nm.

nanoparticle surface as in addition to providing chemical stability; they can introduce various surface functional groups thus further expanding the application of  $\text{Fe}_2\text{O}_3$  nanoparticles.  $-\text{COOH}$  groups coating on magnetic nanoparticles is one of the most sought-after surface functionalizations because they can prove to be extremely useful for medical and bio-analytical research. The  $-\text{COOH}$  group functionalized materials have several advantages including (i)  $-\text{COOH}$  group is hydrophilic in nature therefore  $\text{COOH}@ \text{Fe}_2\text{O}_3$  can be easily dispersed in water thus increasing their capacity to capture the analyte and (ii)  $-\text{COOH}$  group can be covalently bonded with primary amines. Each polypeptide chain carries primary amines ( $-\text{NH}_2$ ) at the N-terminus and in the side chains of lysine amino acids. In proteins, primary amines are usually found outward facing, making them more accessible for conjugation without denaturing protein structure. Furthermore, the size of commercially available  $-\text{COOH}$  functionalized magnetic beads is in the range of  $1\text{-}5\mu\text{m}$  whereas our synthesized C-IONPs particles have much less



diameter (in the range of 250 nm) and further reduction of the size can be achieved by modifying synthesis protocols and applying suitable preparation techniques.

### 2.1.6 X-Ray Photoelectron Spectroscopic (XPS), Raman Spectroscopy and X-ray Diffraction (XRD) Pattern Analysis of C-IONPs

In order to further investigate the oxidation state of Fe and the chemical composition of the sample, XPS studies of the sample were done. The XPS survey spectra (**Fig. 2.11a**) of C-IONPs show that Iron (Fe 2p, 711 eV), Carbon (C1, 285 eV), and Oxygen (O1s, 531 eV) elements are contained in functionalized Fe<sub>2</sub>O<sub>3</sub> nanoparticles. Since C-IONPs are functionalized with –COOH functional groups, a considerable amount of carbon (16.61%) was observed apart from Fe (26.58%) and oxygen (50.89%). The high content of carbon could be due to the presence of the starch network. The small signal was observed at 74.0 eV and it represents aluminum substrate.

The high-resolution O1s spectrum (**Fig. 2.11b**) can be deconvoluted into two peaks. The peak at 535.94 eV (89.41%) corresponds to C-O bond present on the surface of nanoparticles due to ligand. The second peak at 532.09 (10.59%) can be associated with Fe-O bond of core. The deconvoluted peak of O1s at 530.5 eV and 534.6 eV could be indexed to Fe-O and C-O, respectively compared with previous reports as well [6,20-21]. It should be noted that initially the XPS signal from core was not obtained. The sample was sputtered with helium ion cluster to remove the ligand from the surface for depth profiling and the signal was recorded afterward.

The recorded survey scan after each interval of profiling is shown in (**Fig. 2.11c**). It is clear from depth profiling of C-IONPs that they were coated by carbon-based ligands. After each interval of etching the sample with helium ion cluster beam, the wide scan was again recorded. The etching removes the ligand layer around the passivated nanoparticles and hence Fe signal from core begins to increase corresponding to carbon (**Fig. 2.11c**). Moreover, in the high-resolution scan of Fe 2p, it is evident that the energy separation of Fe2p<sub>3/2</sub> between the envelope (713 eV) and satellite (721.3 eV) was 8.3 eV, in the case of Fe 2p<sub>1/2</sub>, it was 8.9 eV between the envelope (727.5 eV) and satellite (736.4 eV) as shown in **Fig. 2.11d**. The energy separation value is in accordance with oxidation state of Fe<sup>3+</sup>,

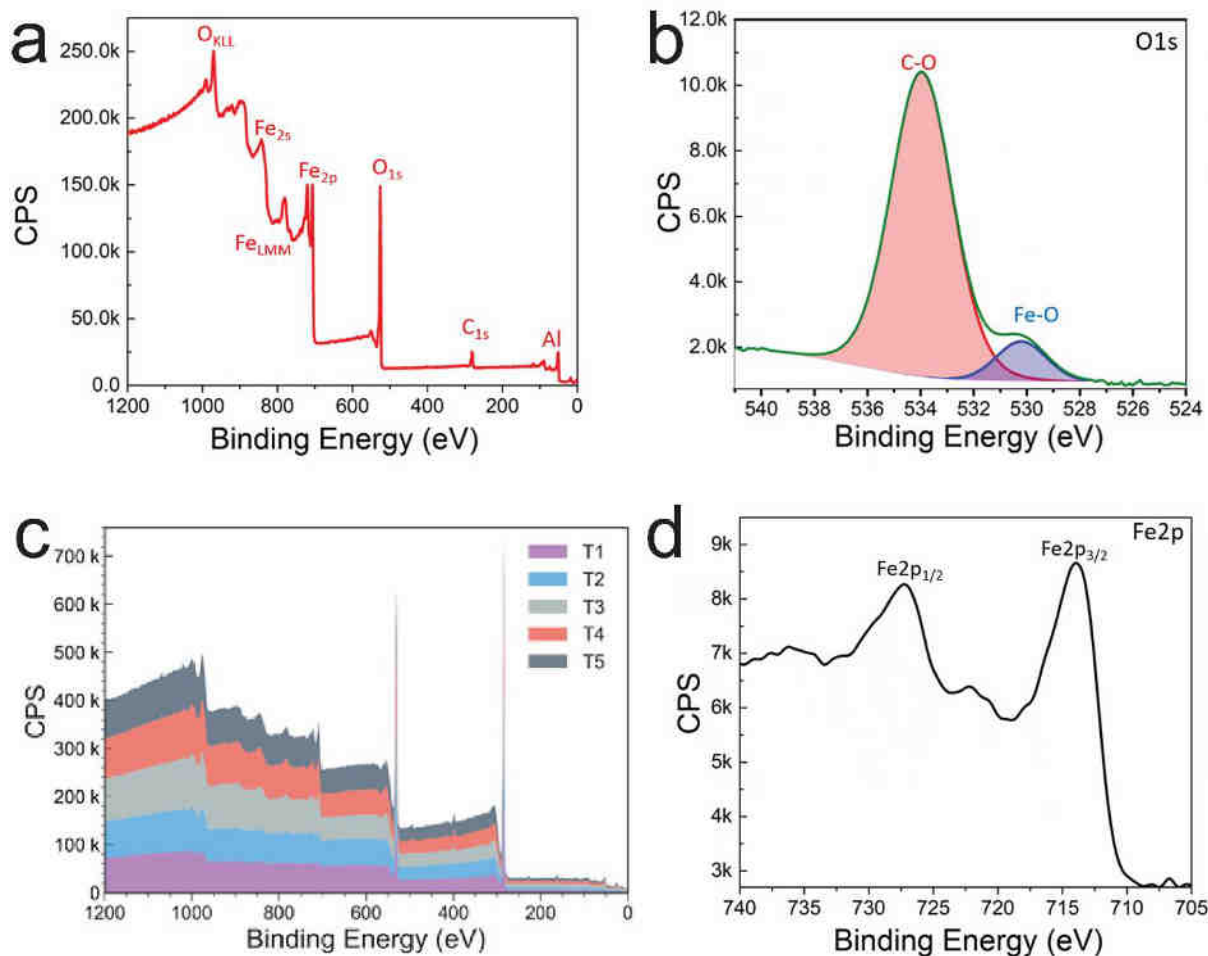


**Figure 2.11**(a) XPS survey spectrum of C-IONPs; (b) deconvoluted O1s, and (c) the XPS wide signal recorded at interval T1, T2, T3, T4 and T5 after etching with cluster beam of helium ions; (d) deconvoluted Fe 2p.

which is different from  $\text{Fe}^{2+}$  value ( $\sim 5$  eV). No other forms of iron ions ( $\text{Fe}^0$  and  $\text{Fe}^{2+}$ ) were detected, confirming that the obtained iron oxide is  $\text{Fe}_2\text{O}_3$ .

A wide-angle XRD measurement was performed for confirming the crystal structure and phases of the synthesized materials. **Fig. 2.12** shows the XRD pattern of  $\text{Fe}_2\text{O}_3$ ,  $\text{Fe}_2\text{O}_3$ @PD and C-IONPs. The position and relative intensities of the reflection peaks of  $\text{Fe}_2\text{O}_3$  nanoparticles were found to be well consistent with the XRD diffraction peaks of standard  $\gamma\text{-Fe}_2\text{O}_3$  sample [JCPDC card no 39-1346].

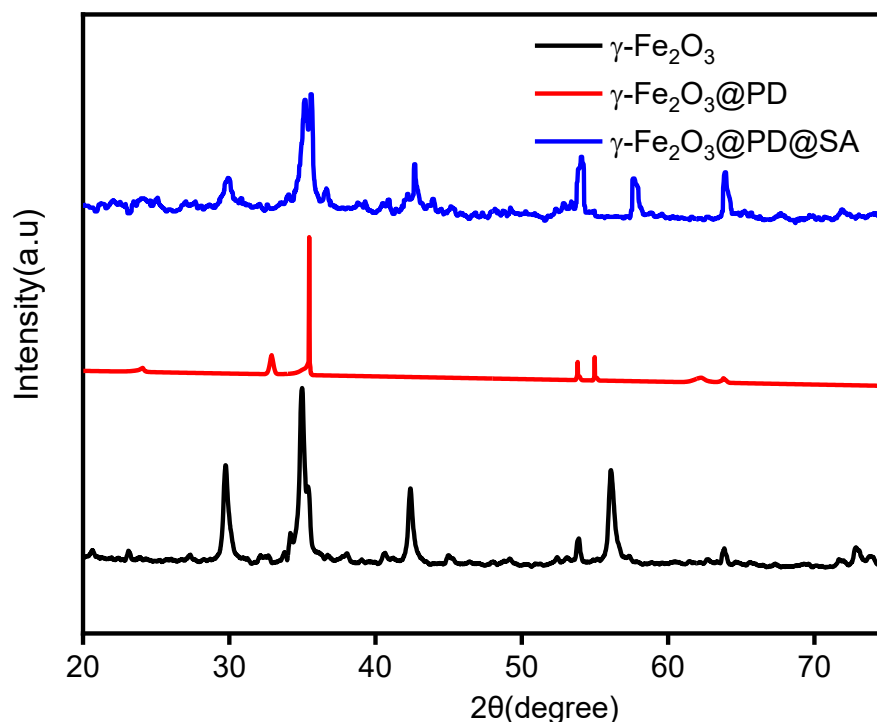


**Figure 2.12** XRD diffraction peaks for  $\text{Fe}_2\text{O}_3$  (black),  $\text{Fe}_2\text{O}_3@PD$  (red) and C-IONPs (blue).

The peaks of synthesized  $\text{Fe}_2\text{O}_3$  at  $2\theta = 30^\circ, 36^\circ, 43^\circ, 54^\circ, 57^\circ, 64^\circ$  and  $75^\circ$  are assigned to (220), (311), (400), (422), (511), (440) and (444) plane respectively of the  $\gamma\text{-Fe}_2\text{O}_3$  inverse spinel structure. The major peaks of the  $\text{Fe}_2\text{O}_3@PD$  and C-IONPs are similar to the  $\gamma\text{-Fe}_2\text{O}_3$ . The PD and succinic anhydride coating on the iron oxide do not bring any significant change in the peak position. The XRD data reveals that the effect of the surface modification on the crystalline structure of  $\gamma\text{-Fe}_2\text{O}_3$  is negligible. Peroxidase catalytic activity of iron oxide nanoparticles immensely depends on their crystalline phases, such as wustite ( $\text{FeO}$ ), goethite ( $\text{FeOOH}$ ), magnetite ( $\text{Fe}_3\text{O}_4$ ), hematite ( $\alpha\text{-Fe}_2\text{O}_3$ ) and meghematite ( $\gamma\text{-Fe}_2\text{O}_3$ ). Among them, meghematite ( $\gamma\text{-Fe}_2\text{O}_3$ ) shows higher peroxidase mimicking activity as compared to the other polymorphs of iron oxide because of their inverse spinel crystal structure, which possess cation vacancies that facilitate the rate-limiting step of Fenton and Harber-Weiss reaction mechanisms [7,22]. In  $\gamma\text{-Fe}_2\text{O}_3$ , all iron atoms are perfectly ordered and iron cations are in trivalent state. These perfectly ordered

vacancies of iron oxide, which follow P4212 crystal space group, may contribute towards the achievement of higher peroxidase activity at room temperature [23].

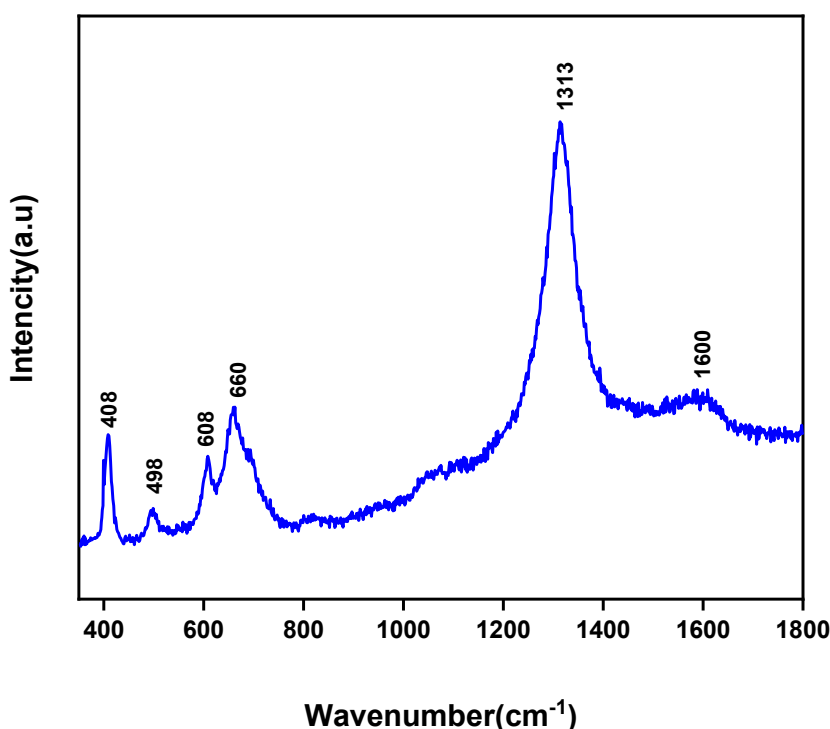


**Figure 2.13** Raman spectrum of C-IONPs.

Raman spectra were obtained for the identification of the phase and surface coating of the C-IONPs (**Fig. 2.13**). The bands observed at 408, 498, and 660 cm<sup>-1</sup> are closely matched with the Raman active phonon modes of the inverse spinel structure of  $\gamma$ -Fe<sub>2</sub>O<sub>3</sub> at 365 cm<sup>-1</sup> (T<sub>2g</sub>), 500cm<sup>-1</sup> (E<sub>g</sub>) and 700 cm<sup>-1</sup> (A<sub>1g</sub>), respectively [24-25]. The inverse spinel structure of the C-IONPs was also confirmed by XRD analysis as described before. The band at 608 cm<sup>-1</sup> could be associated with the splitting of 700 cm<sup>-1</sup> band. The intense and broad band at around 1313cm<sup>-1</sup> could be due to the coupling of C=C stretching and N-H bending, confirming the presence of poly dopamine structure on the particle surface [26]. Furthermore, the characteristic band found near 1600 cm<sup>-1</sup> was due to the C=O stretching of carboxylic acid groups present on the C-IONPs surface [27].

### 2.1.7 Magnetic Properties of C-IONPs

In order to understand the influence of -COOH group on magnetic properties of Fe<sub>2</sub>O<sub>3</sub> nanoparticle, we studied the magnetization of bare IONPs and C-IONPs as a function of applied magnetic field. **Fig. 2.14** shows a comparison of magnetization curves obtained for bare IONPs and carboxyl functionalized nanoparticles C-IONPs at room temperature. It can be seen that both bare IONPs and carboxyl-functionalized nanoparticles C-IONPs demonstrate superparamagnetic characteristics with small hysteresis, remanence and coercivity. A remanent magnetization and coercivity of  $M_{rs} = 2.39$  emu/g and 1.97 emu/g and  $H_c = 0.013$  T are obtained for bare and C-IONPs, respectively. The open hysteresis loops of magnetization as a function of magnetic field indicate a ferrimagnetic ordering at room temperature for both bare IONPs and C-IONPs. The magnetic saturation values are 18.98 and 10.45 emu/g for bare IONPs and C-IONPs, respectively. The decrease in magnetic saturation for C-IONPs is attributed to the enhancement of the nonmagnetic mass due to the effect of functionalized IONPs on the surface of magnetic nanoparticles.

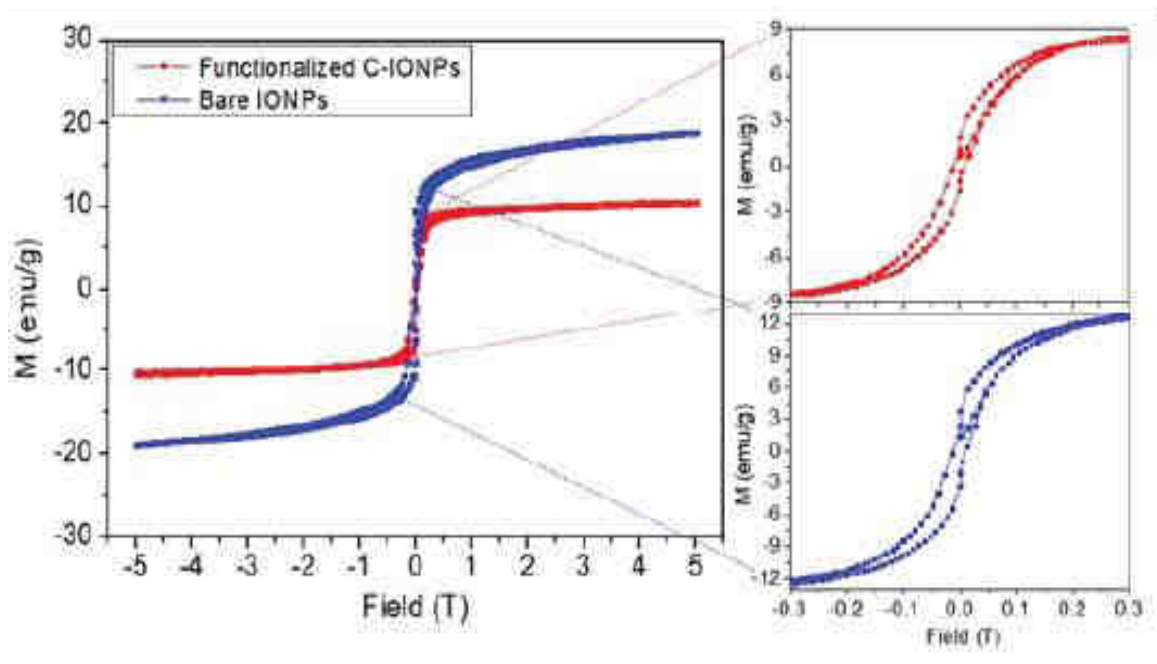


**Figure 2.14** Room temperature field dependent magnetization curve of the bare IONPs and C-IONPs. The inset shows the hysteresis loops of the bare IONPs and C-IONPs.

### 2.1.8 Peroxidase like Activity of C-IONPs.

In order to demonstrate the peroxidase-like activity of C-IONPs, a set of experiments were initially conducted in the presence and absence of C-IONPs. The TMB/H<sub>2</sub>O<sub>2</sub> substrate solution was incubated in the dark for 20 min at room temperature with or without C-IONPs. As shown in **Fig 2.15a**, the reaction with C-IONPs generated a clear blue colored solution at the end of incubation while no color change was observed in the reaction without C-IONPs (negative control). Similarly, as shown in **Fig. 2.15b**, UV-Vis analysis showed seven-time higher absorbance at 652 nm for the sample with C-IONPs as compared to the negative control sample.

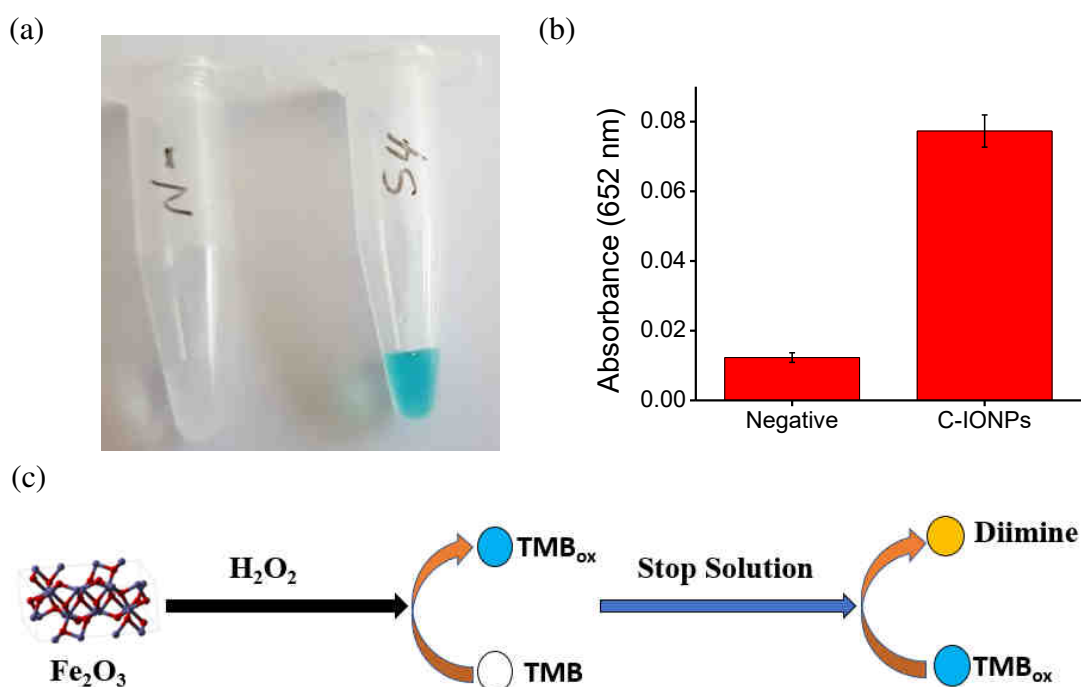


**Figure 2.15** Peroxidase-mimicking activity of C-IONPs; **(a)** a typical photograph of C-IONPs catalyzed oxidation of TMB in the presence of H<sub>2</sub>O<sub>2</sub> (blue color, positive control; colorless, negative control); **(b)** absorbance (UV-vis) data for the negative and positive control samples. The experiments were carried out using 15 μg of C-IONPs, 800 μM TMB and 700 mM H<sub>2</sub>O<sub>2</sub> in 0.2 M acetate buffer (pH 3.6) at room temperature; **(c)** schematic illustration of the peroxidase-mimicking activity of C-IONPs for the oxidation of TMB.

Catalytic oxidation of TMB produces a blue colored cation free charge transfer complex, which shows maximum absorbance at 652 nm. The addition of strong acids (2.0 M HCl) to the reaction yields the yellow colored diimine oxidation product with an absorbance maximum at 450 nm. While both colored compounds can be monitored visually as well as via UV-Vis spectrophotometry, yellow colored product is electroactive. Thus, the nanozyme catalyzed TMB reaction can be used for the development of quantitative biosensing platforms based on the electrochemical quantification of the yellow-colored product [14].

As the concentration of enzyme has a direct effect on the rate of reaction, we first determined the optimal amount of C-IONPs needed for subsequent kinetics studies. We set up a series of experiments whereby the concentration (quantity) of the C-IONPs was varied from 5 – 25  $\mu\text{g}$  keeping the concentrations of TMB and  $\text{H}_2\text{O}_2$  constant (700 mM  $\text{H}_2\text{O}_2$  and 800  $\mu\text{M}$  TMB). As shown in **Fig. 2.2**, in the presence of excess substrate amounts, the absorbance values obtained at the end of a 20 min incubation increased proportionally with the increasing amount of C-IONPs. A higher absorbance indicates a higher amount of blue colored complex, which in turn indicates a proportional increase in the rate of reaction as the reactions were incubated for an equal amount of time. As is evident from the **Fig. 2.2**, the relationship between the nanozyme concentration and reaction rate remained linear within the range of C-IONPs quantities and substrate concentrations tested. 15  $\mu\text{g}$  was selected as the optimum C-IONPs quantity for subsequent steady-state kinetics analysis.

In order to further elucidate the peroxidase mimicking activity of C-IONPs, steady-state kinetics of C-IONPs towards TMB and  $\text{H}_2\text{O}_2$  oxidation were evaluated by the method of initial rates. The TMB concentrations were varied between 100 and 1000  $\mu\text{M}$  keeping  $\text{H}_2\text{O}_2$  concentration constant (700 mM) while for  $\text{H}_2\text{O}_2$  the concentrations were varied from 100 to 1000 mM in the presence of 900  $\mu\text{M}$  TMB. Michaelis–Menten curves were constructed for C-IONPs within the examined concentration ranges for both TMB (**Fig. 2.16a**) and  $\text{H}_2\text{O}_2$  (**Fig. 2.16b**).

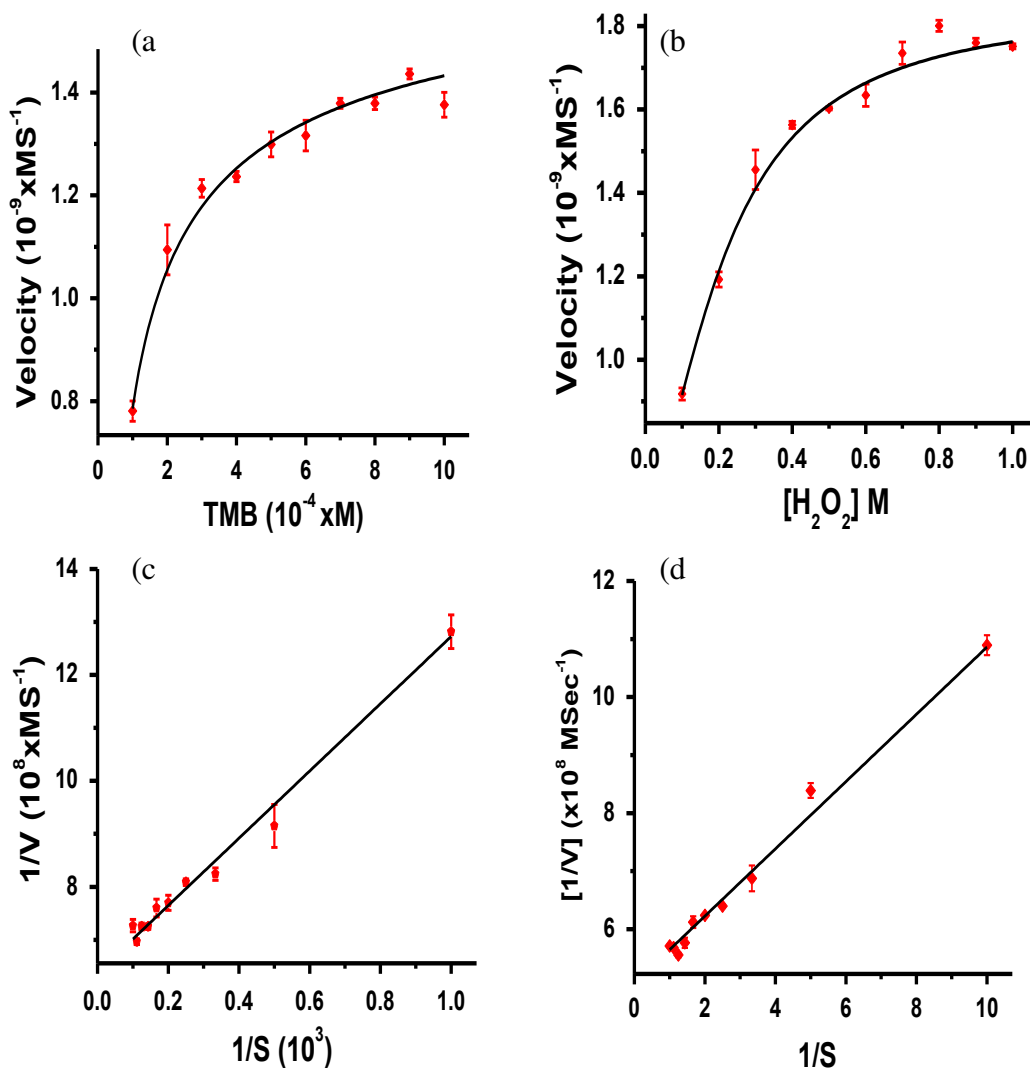


**Figure 2.16** Steady-state kinetic analysis using the Michaelis-Menten model (**a, b**) and Lineweaver–Burk double-reciprocal model (**c, d**) for 15 μgμL<sup>-1</sup> C-IONPs; (**a**) TMB = 100-1000 μM, H<sub>2</sub>O<sub>2</sub> = 700 mM and (**b**) TMB = 900 μM, H<sub>2</sub>O<sub>2</sub> = 100-1000 mM).

The reaction kinetic parameters are represented as  $K_M$  (Michaelis-Menten constant) and  $V_{Max}$  (maximal rate of reaction). The  $K_M$  value is identified as an indicator of enzyme affinity towards the substrate: a lower  $K_M$  value indicates higher substrate affinity and vice versa [7,28]. The higher the  $V_{Max}$  value, the faster the activity (desirable for a rapid response and to minimize sample background effects). The corresponding values of  $K_M$  and  $V_{Max}$  were estimated from double reciprocal plots (**Fig. 2.16c and 2.16d**). These



values were found to be 0.0992 mM and  $0.156 \times 10^{-8} \text{ Ms}^{-1}$  for TMB and 114 mM and  $0.197 \times 10^{-8} \text{ Ms}^{-1}$  for  $\text{H}_2\text{O}_2$ , respectively.

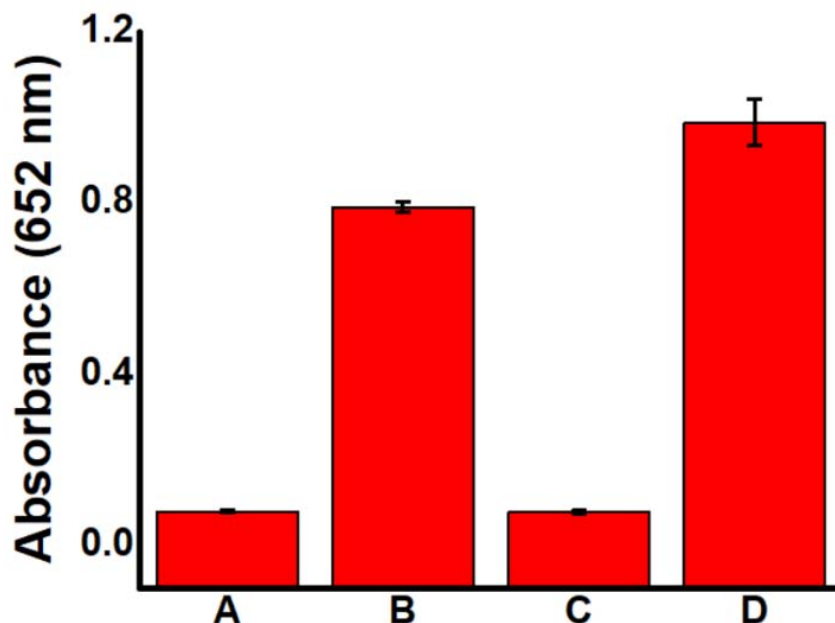


**Figure 2.17** Comparison of nanozyme catalytic activity of C-IONPs with HRP. For (A), TMB = 500  $\mu\text{M}$ ,  $\text{H}_2\text{O}_2$  = 700 mM and  $\text{Fe}_2\text{O}_3$  = 15  $\mu\text{g}$ ; (B), TMB = 500  $\mu\text{M}$ ,  $\text{H}_2\text{O}_2$  = 700 mM and HRP = 0.5 ng; (C), TMB = 1000  $\mu\text{M}$ ,  $\text{H}_2\text{O}_2$  = 700 mM and  $\text{Fe}_2\text{O}_3$  = 15  $\mu\text{g}/\mu\text{L}$ , and (D), TMB = 1000  $\mu\text{M}$ ,  $\text{H}_2\text{O}_2$  = 700 mM and HRP = 0.5 ng).

I also calculated the catalytic constant ( $K_{\text{cat}}$ ) using the following relationship [29].  $K_{\text{cat}} = V_{\text{MAX}} / [\text{E}]$ , where [E] represents the nanoparticle concentration. The calculated values for the  $K_{\text{cat}}$  were found to be  $1.04 \times 10^{-4} \text{ Ms}^{-1} \text{ g}^{-1}$  for TMB and  $1.31 \times 10^{-4} \text{ Ms}^{-1} \text{ g}^{-1}$  for  $\text{H}_2\text{O}_2$ . Finally, I compared the catalytic activity of natural peroxidase horseradish peroxidase (HRP) with C-IONPs. As expected, HRP showed a higher peroxide-like activity compared to C-IONPs (around 10 times with 500  $\mu\text{M}$  and 13 times with 1000  $\mu\text{M}$  TMB) as illustrated in **Fig. 2.17**. However, the values of  $K_{\text{M}}$  and  $V_{\text{Max}}$  for C-IONPs clearly indicate their strong potential as HRP substitutes.

Several iron oxide-based peroxidase-mimicking nanomaterials have been reported in the past. **Table 2** compares the findings of current research work with previous reports.

**Table 2** The obtained kinetic parameters of Fe<sub>2</sub>O<sub>3</sub> in comparison with the previous findings

Catalyst	Substrate	$K_M$ (mM)	$V_{Max}(10^{-8}Ms^{-1})$	Ref
C-IONPs	TMB	0.0992	0.156	This work
	H <sub>2</sub> O <sub>2</sub>	114	0.197	
Fe <sub>3</sub> O <sub>4</sub> MNPs	TMB	0.098	3.44	3
	H <sub>2</sub> O <sub>2</sub>	154	9.78	
Mesoporous $\gamma$ -Fe <sub>2</sub> O <sub>3</sub>	TMB	0.0997	52	5
	H <sub>2</sub> O <sub>2</sub>	144.30	1.84	
Mesoporous $\alpha$ -Fe <sub>2</sub> O <sub>3</sub>	TMB	0.5304	5.43	7
	H <sub>2</sub> O <sub>2</sub>	127.92	3.77	
Mesoporous Fe <sub>2</sub> O <sub>3</sub>	TMB	0.298	7.36	6
	H <sub>2</sub> O <sub>2</sub>	146.7	6.37	
Prussian Blue modified $\gamma$ -Fe <sub>2</sub> O <sub>3</sub>	TMB	0.307	1.06	8
	H <sub>2</sub> O <sub>2</sub>	323.6	1.17	
Au-NPFe <sub>2</sub> O <sub>3</sub> NC	TMB	0.0429	5.882	9
	H <sub>2</sub> O <sub>2</sub>	138.5	4.770	
PB-Fe <sub>2</sub> O <sub>3</sub>	TMB	0.009	12.3	10
	H <sub>2</sub> O <sub>2</sub>	15	22.8	
Graphene oxide (GO)-Fe <sub>2</sub> O <sub>3</sub>	TMB	0.118	5.38	11
	H <sub>2</sub> O <sub>2</sub>	305	1.01	

The obtained values of  $K_M$  and  $V_{Max}$  for our C-IONPs were in many cases comparable to previously reported Fe<sub>2</sub>O<sub>3</sub>-based nanoparticles. For example  $K_M$  value towards TMB of a recently reported mesoporous  $\gamma$ -Fe<sub>2</sub>O<sub>3</sub> nanoparticles was shown to be 0.0997 which is comparable to the C-IONPs reported in this work while for  $\alpha$ -Fe<sub>2</sub>O<sub>3</sub> it was reported as 0.5304 which is significantly higher than our C-IONPs [7]. Similarly, affinity of our C-IONPs towards TMB was comparable to the peroxidase mimicking Fe<sub>3</sub>O<sub>4</sub> magnetic nanoparticles reported by Gao *et al.* in their pioneering work [3]. Likewise, C-IONPs reported in this study showed significantly lower  $K_M$  values towards H<sub>2</sub>O<sub>2</sub> as compared to these three nanozymes (Table 2). While Prussian blue-modified Fe<sub>2</sub>O<sub>3</sub> reported by

Dutta *et al.* showed much better affinities towards both TMB and H<sub>2</sub>O<sub>2</sub> in comparison to that of our C-IONPs, our C-IONPs offer the additional advantage of –COOH groups for easy conjugation to proteins and –NH<sub>2</sub>-terminated DNA probes, indicating their immense potential for biosensing applications

## Conclusions

In this work, a new class of carboxyl group-functionalized magnetic Fe<sub>2</sub>O<sub>3</sub> nanoparticles have been synthesized applying starch-assisted method and showed that they exhibit intrinsic peroxidase-mimetic activity towards TMB and H<sub>2</sub>O<sub>2</sub>. Scanning electron and transmission electron microscopy analysis revealed that the nanoparticles possess a spherical shape with an average size of ~ 250 nm. X-Ray Photoelectron Spectroscopic (XPS), and X-ray Diffraction (XRD) Pattern analysis showed that the obtained iron oxide is Fe<sub>2</sub>O<sub>3</sub> that possess inverse spinal structure. Raman spectroscopy emerged that –COOH group present on the nanoparticles surface. Peroxidase-mimicking activity of C-IONPs was investigated through catalytic oxidation of 3,3',5,5'-tetramethylbenzidine (TMB) in the presence of H<sub>2</sub>O<sub>2</sub>. The results showed that nanoparticles follow typical Michaelis-Menten kinetics and exhibit excellent affinity towards TMB and H<sub>2</sub>O<sub>2</sub> with estimated  $K_M$  and  $V_{Max}$  values of 0.0992 mM and  $0.156 \times 10^{-8} \text{ Ms}^{-1}$  for TMB, and 114 mM and  $0.197 \times 10^{-8} \text{ Ms}^{-1}$  for H<sub>2</sub>O<sub>2</sub>, respectively. The particles showed comparable or superior peroxidase-mimetic activity compared to other iron oxide-based nanomaterials. The presence of carboxylic acid –COOH groups on to their surface, the C-IONPs can potentially be conjugated to various antibodies and DNA based probes and hence offer immense potential in biomolecule detection.

## References

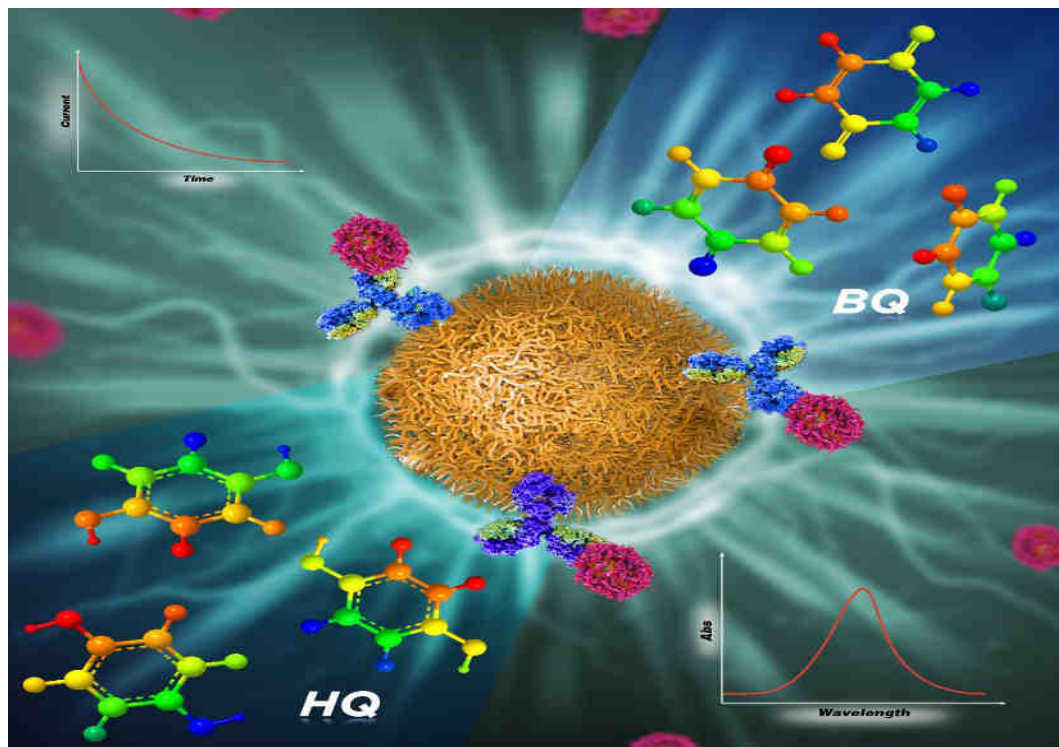
- [1] H. Wei and E. Wang, “Nanomaterials with enzyme-like characteristics (nanozymes): next-generation artificial enzymes,” *Chem. Soc. Rev.*, vol. 42, no. 14, pp. 6060–6093, Jun. 2013.
- [2] J. Wu *et al.*, “Nanomaterials with enzyme-like characteristics (nanozymes): Next-generation artificial enzymes (II),” *Chemical Society Reviews*, vol. 48, no. 4. Royal Society of Chemistry, pp. 1004–1076, Feb. 2019.
- [3] L. Gao *et al.*, “Intrinsic peroxidase-like activity of ferromagnetic nanoparticles,” *Nat. Nanotechnol.* 2007 29, vol. 2, no. 9, pp. 577–583, Aug. 2007.
- [4] M. Liang and X. Yan, “Nanozymes: From New Concepts, Mechanisms, and Standards to Applications,” *Acc. Chem. Res.*, vol. 52, no. 8, pp. 2190–2200, Aug. 2019.
- [5] W. Wu, Q. He, and C. Jiang, “Magnetic Iron Oxide Nanoparticles: Synthesis and Surface Functionalization Strategies,” *Nanoscale Res. Lett.* 2008 311, vol. 3, no. 11, pp. 397–415, Oct. 2008.
- [6] R. Bhattacharjee *et al.*, “Porous nanozymes: The peroxidase-mimetic activity of mesoporous iron oxide for the colorimetric and electrochemical detection of global DNA methylation,” *J. Mater. Chem. B*, vol. 6, no. 29, pp. 4783–4791, 2018.
- [7] M. K. Masud *et al.*, “Nanoarchitected peroxidase-mimetic nanozymes: mesoporous nanocrystalline  $\alpha$ - or  $\gamma$ -iron oxide?,” *J. Mater. Chem. B*, vol. 7, no. 35, pp. 5412–5422, Sep. 2019.
- [8] Z. Yang *et al.*, “Hollow platinum decorated Fe<sub>3</sub>O<sub>4</sub> nanoparticles as peroxidase mimetic couple with glucose oxidase for pseudobienzyme electrochemical immunosensor,” *Sensors Actuators B Chem.*, vol. 193, pp. 461–466, Mar. 2014.
- [9] X.-Q. Zhang, S.-W. Gong, Y. Zhang, T. Yang, C.-Y. Wang, and N. Gu, “Prussian blue modified iron oxide magnetic nanoparticles and their high peroxidase-like activity,” *J. Mater. Chem.*, vol. 20, no. 24, pp. 5110–5116, Jun. 2010.
- [10] M. K. Masud *et al.*, “Gold-Loaded Nanoporous Ferric Oxide Nanocubes with Peroxidase-Mimicking Activity for Electrocatalytic and Colorimetric Detection of Autoantibody,” *Anal. Chem.*, vol. 89, no. 20, pp. 11005–11013, Oct. 2017.
- [11] A. K. Dutta *et al.*, “Peroxidase-like activity and amperometric sensing of hydrogen peroxide by Fe<sub>2</sub>O<sub>3</sub> and Prussian Blue-modified Fe<sub>2</sub>O<sub>3</sub> nanoparticles,” *J. Mol. Catal. A Chem.*, vol. 360, pp. 71–77, Aug. 2012.
- [12] L. Song *et al.*, “Graphene oxide-based Fe<sub>2</sub>O<sub>3</sub> hybrid enzyme mimetic with enhanced peroxidase and catalase-like activities,” *Colloids Surfaces A Physicochem. Eng. Asp.*, vol. 506, pp. 747–755, Oct. 2016.
- [13] M. Hasanzadeh, N. Shadjou, and M. de la Guardia, “Iron and iron-oxide magnetic nanoparticles as signal-amplification elements in electrochemical biosensing,” *TrAC Trends Anal. Chem.*, vol. 72, pp. 1–9, Oct. 2015.

- [14] M. K. Masud *et al.*, “Superparamagnetic nanoarchitectures for disease-specific biomarker detection,” *Chem. Soc. Rev.*, vol. 48, no. 24, pp. 5717–5751, Dec. 2019.
- [15] H. Lineweaver and D. Burk, “The Determination of Enzyme Dissociation Constants,” *J. Am. Chem. Soc.*, vol. 56, no. 3, pp. 658–666, Mar. 2002.
- [16] Y. Fan, W. Shi, X. Zhang, and Y. Huang, “Mesoporous material-based manipulation of the enzyme-like activity of CoFe<sub>2</sub>O<sub>4</sub> nanoparticles,” *J. Mater. Chem. A*, vol. 2, no. 8, pp. 2482–2486, Feb. 2014.
- [17] J. Livage, M. Henry, and C. Sanchez, “Sol-gel chemistry of transition metal oxides,” *Progress in Solid State Chemistry*, vol. 18, no. 4, pp. 259–341, Jan. 1988.
- [18] B. P. Upoma, F. Mahnaz, W. Rahman Sajal, N. Zahan, M. S. Hossain Firoz, and M. S. Azam, “Bio-inspired immobilization of silver and gold on magnetic graphene oxide for rapid catalysis and recyclability,” *J. Environ. Chem. Eng.*, vol. 8, no. 3, p. 103739, Jun. 2020.
- [19] M. Shultz, J. Reveles, S. K.-J. of the, and undefined 2007, “Reactive nature of dopamine as a surface functionalization agent in iron oxide nanoparticles,” *ACS Publ.*, vol. 129, no. 9, pp. 2482–2487, Mar. 2007.
- [20] Y. Wu *et al.*, “Fast and Simple Preparation of Iron-Based Thin Films as Highly Efficient Water-Oxidation Catalysts in Neutral Aqueous Solution,” *Angew. Chemie Int. Ed.*, vol. 54, no. 16, pp. 4870–4875, Apr. 2015.
- [21] M. Chen *et al.*, “An Iron-based Film for Highly Efficient Electrocatalytic Oxygen Evolution from Neutral Aqueous Solution,” *ACS Appl. Mater. Interfaces*, vol. 7, no. 39, pp. 21852–21859, Oct. 2015.
- [22] A. B. Seabra, M. T. Pelegriño, and P. S. Haddad, “Antimicrobial Applications of Superparamagnetic Iron Oxide Nanoparticles: Perspectives and Challenges,” *Nanostructures Antimicrob. Ther. Nanostructures Ther. Med. Ser.*, pp. 531–550, Jan. 2017.
- [23] L. MacHala, J. Tuček, and R. Zbořil, “Polymorphous transformations of nanometric iron(III) oxide: A review,” *Chem. Mater.*, vol. 23, no. 14, pp. 3255–3272, Jul. 2011.
- [24] A. M. Jubb and H. C. Allen, “Vibrational Spectroscopic Characterization of Hematite, Maghemite, and Magnetite Thin Films Produced by Vapor Deposition,” *ACS Appl. Mater. Interfaces*, vol. 2, no. 10, pp. 2804–2812, Oct. 2010.
- [25] M. A. G. Soler and F. Qu, “Raman Spectroscopy of Iron Oxide Nanoparticles,” *Raman Spectrosc. Nanomater. Charact.*, vol. 9783642206207, pp. 379–416, Mar. 2012.
- [26] J. Ryu, S. Ku, H. Lee, C. P.-A. F. Materials, and undefined 2010, “Mussel-inspired polydopamine coating as a universal route to hydroxyapatite crystallization,” *Wiley Online Libr.*, vol. 20, no. 13, pp. 2132–2139, Jul. 2010.
- [27] J. A. Luceño-Sánchez and A. M. Díez-Pascual, “Grafting of Polypyrrole-3-carboxylic Acid to the Surface of Hexamethylene Diisocyanate-Functionalized

- Graphene Oxide,” *Nanomater.* 2019, Vol. 9, Page 1095, vol. 9, no. 8, p. 1095, Jul. 2019.
- [28] T. Xue *et al.*, “Graphene-Supported Hemin as a Highly Active Biomimetic Oxidation Catalyst,” *Angew. Chemie*, vol. 124, no. 16, pp. 3888–3891, Apr. 2012.
- [29] P. Weerathunge *et al.*, “Ultrasensitive Colorimetric Detection of Murine Norovirus Using NanoZyme Aptasensor,” *Anal. Chem.*, vol. 91, no. 5, pp. 3270–3276, Mar. 2019.

# CHAPTER THREE

## Direct Isolation and Detection of Exosomes Using Functionalized Iron oxide (C-IONPs) Nanozymes



## CHAPTER THREE

---

### 3 Direct Isolation and Detection of Exosomes Using Functionalized Iron oxide (C-IONPs) Nanozymes

#### Introduction

Exosomes are small membrane-bound extracellular nanovesicles (30-150 nm) released by almost all cell types by fusion of an intermediate endocytic compartment. Consequently, exosomes can be found in various body fluids like blood, urine, and saliva [1-5]. Exosomes were first coined nearly 30 years ago since then used as a cell-to-cell communication and transmission of disease states. Due to their high cell-of-origin specificity, exosomes have increasingly been recognized as promising biomarkers for a range of disease conditions, including cancers. In addition to the exosomes themselves, biomolecules like proteins, DNA, and RNA which are packed inside the exosomes have also been demonstrated as powerful disease biomarkers [6-11].

Thus isolation, detection and quantification of exosomes have gained immense research interest, particularly for the development of minimally invasive disease diagnosis platforms. Over the past decades, plenty of conventional methods such as Western blotting, Enzyme-linked immunosorbent assays (ELISAs), Immunoaffinity-based method, commercial isolation kit and differential centrifugation have been used extensively for the analysis of exosomes in body fluids [12-18]. Western blotting and Enzyme-linked immunosorbent assays (ELISAs) usually require a large amount of sample and extensive technical steps for Exosome detection. Although Differential centrifugation methods are inexpensive, these need several preparation steps and long assay time from several hours to overnight. While commercially available kit-based isolation methods incur additional costs and rely on bulky instruments. Immuni-affinity-based exosomes analysis have been revealing as a promising strategy to isolate exosomes of a specific origin, using the affinity interaction between exosomal proteins and their specific antibodies. However, the efficiency of these methods is highly dependent on exosomes membrane markers and respective antibodies. Boriachek et al. developed a method for direct isolation and detection of disease specific exosomes using super-



paramagnetic gold-loaded ferric oxide nanocubes. Without any pre-isolation steps, the method achieved a high sensitivity of detecting  $10^3$  exosomes/mL directly from the complex cell culture media [19-17]. However, current exosome detection methods are cumbersome and expensive. In order to circumvent these issues, a facial, sensitive single-step method is inevitable to detect exosomes that would be transformative in the clinical research of exosomal biomarkers.

With the advent of nanotechnology, nanozymes have gained enormous interest in biomedical applications. The biocompatibility and unique magnetic properties of iron oxide nanoparticles (IONPs) offer several advantages in biomedical applications, particularly biosensing. Peroxidase-mimicking iron oxide can simultaneously provide multiple functions, i.e., capture and magnetic purification of the target analyte from a complex medium, and nanozyme activity for target detection [20]. Detailed analysis of catalytic activity of iron oxide based nanozymes suggests a double displacement mechanism; higher affinity towards TMB with a lower affinity towards  $H_2O_2$  compared to HRP.

In this study, a simple and direct exosomes isolation method was developed based on synthesized carboxyl group-functionalized magnetic iron oxide nanoparticles (C-IONPs). The particles were synthesized using a starch-assisted method followed by surface functionalization, and characterized by different spectroscopy methods that have been explained comprehensively in previous chapter (**chapter two**). The peroxidase-like activity of C-IONPs was investigated by studying the catalytic oxidation of peroxidase substrate TMB in the presence of  $H_2O_2$  at room temperature (**chapter two**). Herein, I demonstrated the applicability of C-IONPs both as (i) “dispersible nanocarriers” to capture bulk populations of exosomes and (ii) nanozymes to generate enzyme catalytic responses for the analysis of cancer-specific exosomes. C-IONPs were initially modified with a generic antibody CD9 and used as “dispersible nanocarriers” to capture exosomes directly from cell culture media. Captured exosomes were subsequently immobilized onto screen printed carbon electrodes (SPCEs) pre-functionalized with ovarian cancer specific CA125 antibody, then followed by chronoamperometric detection exploiting the peroxidase-mimicking activity of C-IONPs via the hydrogen peroxide/ hydroquinone ( $H_2O_2/HQ$ ) system.

## **Experimental**

### **3.1.1 Reagents and Materials**

Unless otherwise stated, the reagents used for the experiments were of analytical grade and purchased from Sigma Aldrich (Australia). Anti-CD9 and anti-CA125 antibodies were purchased from Abcam, Ultrapure DNase/RNase-free distilled water (Invitrogen, Australia) was used to carry out the experiments. Extraavidin-modified screen-printed carbon electrodes (DRP110XTR) were purchased from Dropsens (Spain). Hydroquinone and hydrogenperoxide solution were purchased from thermo Fisher Scientific Australia. Ovarian cancer cell line OVCAR3 and non-cancerous mesothelial cell line MeT-5A were purchased from American Type Culture Collection (ATCC),

### **3.1.2 Cell Culture and Isolation of Exosomes**

Ovarian cancer cell line OVCAR3 and non-cancerous mesothelial cell line MeT-5A were maintained in phenol red-free RPMI 1640 medium supplemented with 10% heat-inactivated fetal bovine serum (FBS), 100 U/mL penicillin, and 100 mg/mL streptomycin. Cultures were maintained in a humidified incubator at 37 °C with 5% CO<sub>2</sub>. After they reached 70% confluence, the media was removed and cells were washed with 1X phosphate-buffered saline (PBS) and finally supplemented with growth medium containing 10% exosome depleted FBS and 1% penicillin/streptomycin (exosome media). Cells were incubated for another 60 h and the conditioned medium (containing exosomes) was collected. Cells and debris were removed from the conditioned media by centrifuging at 2000 g for 30 min and supernatant was transferred to clean 1.5 mL microcentrifuge tubes in 50 µL of phosphate-buffered saline (PBS; 10 mM, pH 7.4) and stored at -20 °C for further use.

### **3.1.3 Cryo-Transmission Electron Microscopy (Cryo-TEM)**

For cryo-TEM, 4 µL of exosome isolated from the cell-culture media were directly adsorbed onto lacey carbon grids (Quantifoil, Germany) and plunged into liquid ethane, using an FEI Vitrobot Mark 3 (FEI Company, The Netherlands). Grids were blotted at 100% humidity at 4 °C for about 3-4 s. Frozen/vitrified samples were imaged using Tecnai T12 Transmission Electron Microscope (FEI Company) operating at an acceleration

voltage of 120 kV. Images were taken at 30,000x magnification, (approximate dose of 13.6 electrons/Å<sup>2</sup>), using an FEI Eagle 4k CCD (FEI Company), and SerialEM image acquisition software.

#### **3.1.4 Preparation of Anti-CD9 Conjugated C-IONPs**

Antibodies against CD9 were conjugated to –COOH functionalized iron oxide nanoparticles through standard EDC/NHS coupling following previously published protocol [21-22]. Briefly, 1 mg C-IONPs were dispersed in 0.1 M MES buffer, pH 5. Using DynaMag 2 magnetic separation rack (Thermo Fisher Scientific Australia) the nanoparticles were washed 3 times with MES buffer and finally resuspended evenly in 500 µL MES buffer by repeated pipetting up and down. To activate the –COOH modified Fe<sub>2</sub>O<sub>3</sub>, EDC and NHS were added in the ratio MNPs: EDC: NHS = 1:4:6 mg and incubated for 15 mins at 37 °C with continuous rotation. C-IONPs were separated magnetically from the reaction mixture and 500 µL of anti-CD9 antibody (10 µg mL<sup>-1</sup>) diluted in 10 mM PBS buffer pH 7.4 was mixed with activated C-IONPs (C-IONPs: Ab = 1mg: 5µg). The activated C-IONPs/anti-CD9 mixture was incubated at 4 °C overnight with continuous rotation followed by magnetic separation and 3 X washing with PBS buffer. Anti-CD9 conjugated C-IONPs were finally resuspended in 1 mL PBS buffer. To verify the successful conjugation of C-IONPs with the anti-CD9 antibody FTIR spectra for both conjugated and unconjugated C-IONPs were recorded in the range of 500 - 3500 cm<sup>-1</sup> on a Nicolet 5700 FT-IR spectrometer (Nicolet Inc., Madison, USA) by transmission FTIR spectroscopy

#### **3.1.5 Direct Isolation of Exosomes from Cell Culture Media and Plasma Samples**

100 µL of conditioned cell media was mixed with 5 µL of anti-CD9 conjugated C-IONPs and incubated for 30 min at room temperature on a reciprocating shaker. The exosomes attached C-IONPs were magnetically isolated and washed three times with 1X PBS. Isolated exosomes were finally transferred to CA-125 antibody functionalized screen SPCEs. For negative control (no template control, NTC) 100 µL of fresh exosome media was used instead of conditioned media. For known spike of exosomes in plasma samples, they were initially isolated from OVCAR3 derived exosome conditioned media using a commercially available Total Exosome Isolation Reagent (from cell culture media) (Cat

# 4478359, ThermoFisher Scientific, Australia) as per manufacturer's instructions. Known concentrations of exosomes were spiked in human plasma (Cat # P9523, Sigma Aldrich). Exosomes were isolated directly from 100  $\mu$ L of spiked in plasma samples using anti-CD9 conjugated C-IONPs as described above.

### **3.1.6 Fabrication of Sensor and Chronoamperometric Detection of Exosomes**

Unless otherwise stated, all incubation steps were carried out at room temperature with shaking at 300 rpm, and electrodes were washed with 1X PBS and air dried between each step. The sensor for exosome detection was fabricated by incubating 10  $\mu$ L of 10  $\mu$ g mL<sup>-1</sup> of biotinylated anti-CA125 onto extravidin modified SPCE (DRP-110XTR, DropSens) for 30 min. The free surface was passivated by incubating the electrode with 10  $\mu$ L of 1% BSA for 20 min. Magnetically isolated exosomes were then added onto the sensor surface and incubated for 30 min. Exosomes were chronoamperometrically detected at the potential of -200 mV vs Ag/AgCl for 200 sec. 35  $\mu$ L of freshly prepared 1.0 mM solution of hydroquinone (HQ) was added onto the sensor surface and the chronoamperometry was run. After the stabilisation of the background current (around 50 sec), 35  $\mu$ L of 0.1 M H<sub>2</sub>O<sub>2</sub> was added onto the electrode surface and the reaction was allowed to continue until the steady-state current was achieved (at >200 sec). The difference between the steady-state currents for the sample and corresponding background ( $\Delta i$ ) was calculated. In a separate set of experiments, exosomes isolated from OVCAR3 cell culture media using a commercial kit were directly deposited onto the sensor surface. In this case, HRP-conjugated anti-CD9 antibody was used to catalyze the HQ/H<sub>2</sub>O<sub>2</sub> reaction and the chronoamperometric response was recorded as above.

## **Results and Discussion**

### **3.1.7 Size and Vesicular Compartments of Exosomes**

Cryo-TEM analysis suggested that the isolated exosomes contained double-walled lipid membrane layers (**Fig. 3.1**) with the average size estimated to be  $120 \pm 5.17$  nm. The morphological characteristics obtained here corroborate with previous evidence, suggesting that these vesicles are probably of exosomal origin [19-23].

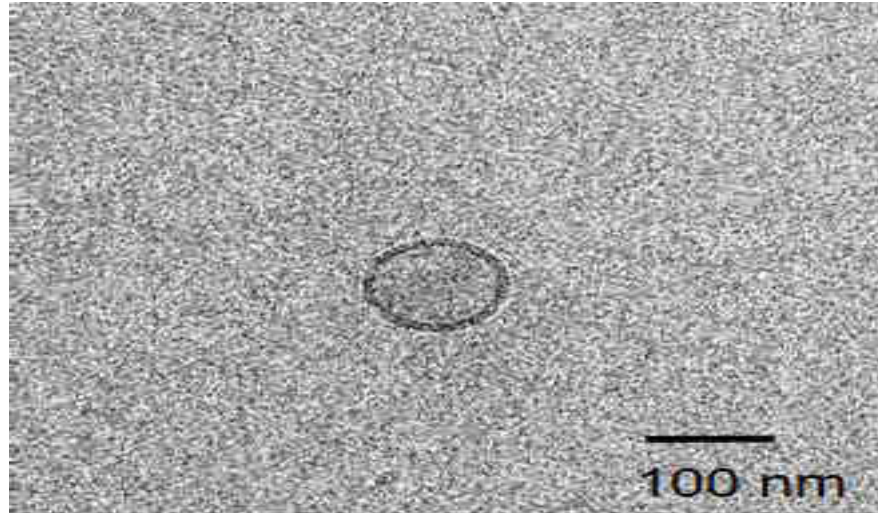


**Figure 3.1** Cryo-TEM images of OVCAR3 cell derived exosomes demonstrating size and vesicular compartments such as membrane layers.

### **3.1.8 FTIR Analysis of C-IONPs and Anti-CD9/C-IONPs**

As can be seen in **Figure 3.2**, FTIR analysis provided the evidence both for the presence of surface  $\text{-COOH}$  groups on unconjugated C-IONPs as well as successful crosslinking reaction. For unconjugated C-IONPs, strong broad peak between 3300-2500 was observed indicative of O-H stretching in  $\text{-COOH}$  group present on the nanoparticle surface. Similarly, strong C=O stretching peak around  $1706\text{ cm}^{-1}$  was also observed. In contrast, several new peaks emerged in anti-CD9 conjugated C-IONPs. Most important among these, considered to be the characteristic peaks of amide bonds, were a strong peak at  $1661\text{ cm}^{-1}$ ,  $1551\text{ cm}^{-1}$ , and  $1361\text{ cm}^{-1}$  due to stretching of associated C=O primary amide I, amide II, amide III respectively and a medium peak around  $3113\text{ cm}^{-1}$  attributable to amide B N-H stretch.

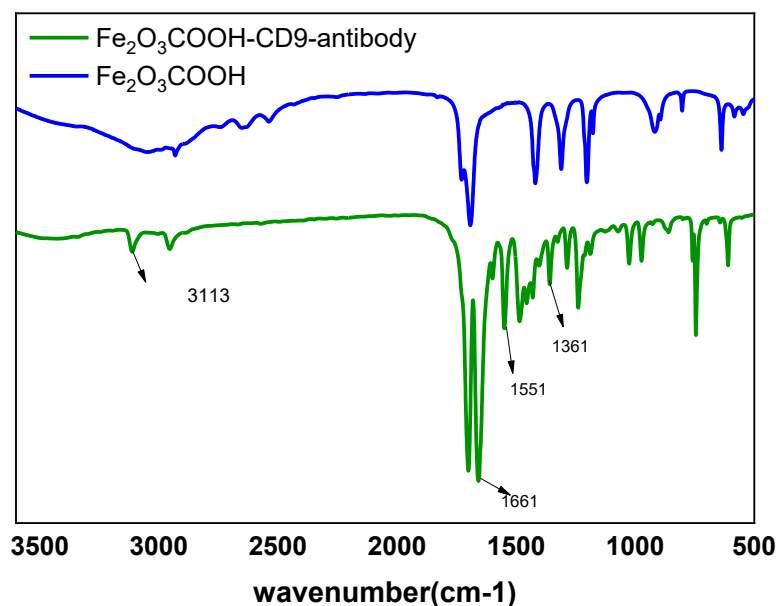


**Figure 3.2** FTIR analysis of C-IONPs and anti-CD9/C-IONPs.

### 3.1.9 Direct Isolation and Detection of Exosomes

Taking advantage of the magnetic collection/separation and peroxidase mimetic activities of C-IONPs as well as the presence of –COOH group on the nanoparticle surface, we designed an assay for direct capture and electrochemical detection of exosomes derived from ovarian cancer cells. The schematic representation of steps involved in the isolation and detection of exosomes is depicted in **Fig. 3.3**. In the first step, C-IONPs were functionalized with exosome specific CD9 antibody (hereafter referred to as C-IONPs/anti-CD9) via standard *N*-(3-Dimethylaminopropyl)-*N'*-ethylcarbodiimide hydrochloride (EDC)/*N*-hydroxysuccinimide (NHS) coupling reaction. CD9 is an exosomes specific protein that is found on the membrane of almost all types of exosomes. I therefore used C-IONPs/anti-CD9 to capture the bulk exosomes population from cell culture media. First, I dispersed C-IONPs/anti-CD9 into the cell culture media to selectively bind to the exosomes population (referred to as C-IONPs/anti-CD9/Exo). The C-IONPs/anti-CD9/Exo were magnetically purified with

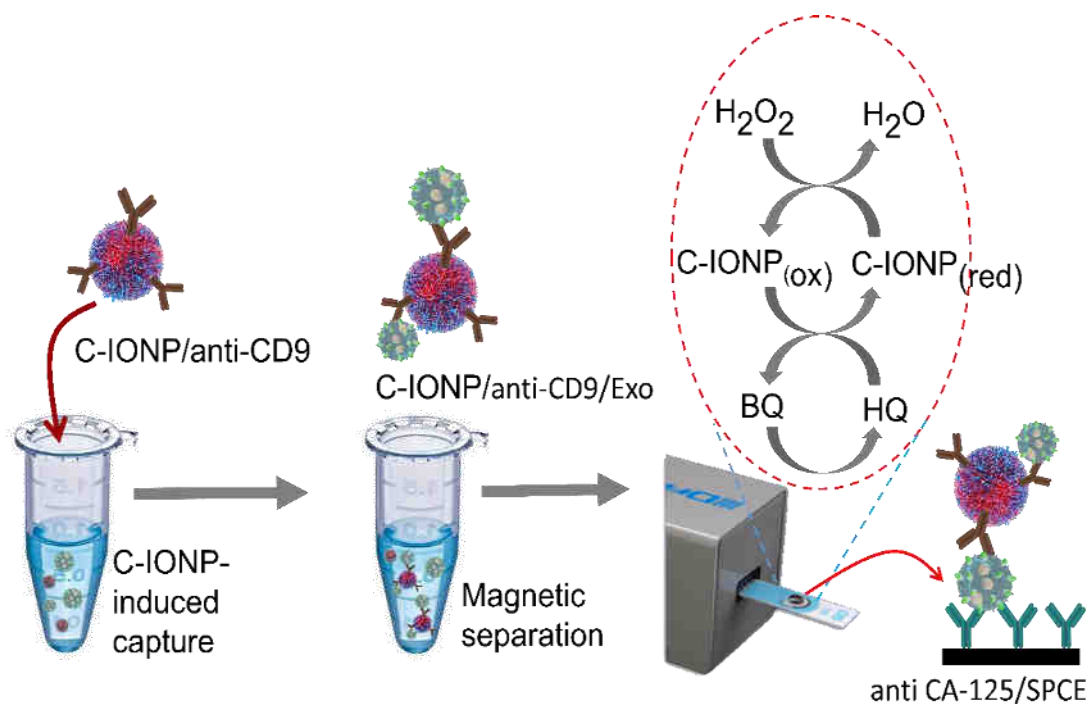


**Figure 3.3** Schematic representation of the assay for the direct detection of ovarian cancer cell-derived exosomes. CD-9 antibody functionalised-C-IONPs were dispersed in the conditioned exosome media derived from OVCAR3 or Met5a cell lines. After magnetic isolation and separation, the exosome-bound C-IONPs were incubated onto an extravidin-modified screen-printed carbon electrode pre-functionalized with biotinylated anti-CA-125. The immunocomplex formed on the electrode surface (C-IONPs/anti-CD9/Exo/anti-CA-125/SPCE) was then treated with  $\text{H}_2\text{O}_2/\text{HQ}$  and chronoamperometric measurement at 0.2V (vs. Ag/AgCl) was used to get the amperometric current.

multiple magnetic washing and isolation steps and collected by pipetting out supernatant solutions. In the second step, extravidin modified SPCEs were functionalized with biotinylated CA-125 antibody (referred to as anti-CA-125/SPCE) through standard biotin-avidin chemistries [24]. Anti-CA-125 is a well-known ovarian cancer biomarker and is overexpressed in ovarian cancer derived exosomes. Thus, ovarian cancer specific exosomes present in the captured bulk population were sub-populated via incubating purified C-IONPs/anti-CD9/Exo with anti-CA-125/SPCE (referred to as C-IONPs/anti-CD9/Exo/anti-CA-125/SPCE). The amount of sandwiched exosomes between surface bound CA-125 and C-IONPs-attached CD9 antibodies were detected by measuring the cathodic current generated by HQ mediated enzymatic reduction of  $\text{H}_2\text{O}_2$ .

### 3.1.10 Assay Functionality and Specificity

To check the assay functionality, the levels of the CA-125-specific exosomes present in the positive and negative samples were studied by comparing the chronoamperometric currents. The positive control samples contain as prepared exosomes-derived from ovarian cancer cell line OVCAR3 with the defined bulk exosomes concentration of  $1 \times 10^7$  exosomes/mL, where the negative control (referred to as NTC) contains exosomes-derived from non-cancerous mesothelial cell line MeT-5A. As can be seen in **Fig 3.4a**, the amperometric current for the positive sample is over 11-times higher than that of the NTC sample (change in current for positive and negative samples are 386 and 35 nA respectively). In another experiment without the use of the CD9 antibody on the C-IONPs surface (referred to as “no antibody control”; NAC), the assay protocol for analyzing as-prepared OVCAR3-derived exosomes (i.e.,  $1 \times 10^7$  exosomes/mL) resulted in a significantly low level of the amperometric signal (22 nA). This low response could be due to the absence of C-IONPs nanozymes on the anti-CA-125/SPCE surface. A slightly higher current (27nA) was observed in a control experiment, when no exosomes were present in the sample (referred to as Blank).

The slightly higher current in the Blank experiment could be explained by the fact that C-IONPs/anti-CD9 could be nonspecifically attached onto the anti-CA-125/SPCE surface. In the last control experiment, CD9 antibody without conjugation with the C-IONPs (i.e., no nanoparticle control, NNPC) was mixed with the as-prepared (undiluted) exosome samples. The samples were then processed identically to the positive sample and resulted in a very low level of amperometric current (i.e., 15 nA). Clearly, the lowest level of the response was due to the absence of C-IONPs onto the anti-CA-125/SPCE surface. The level of the amperometric signals generated in these control experiments was significantly lower than that of the positive control. The higher response obtained for the CA-125-specific exosomes could be explained by considering the fact that (**a**) covalent attachment of CD9 antibody onto



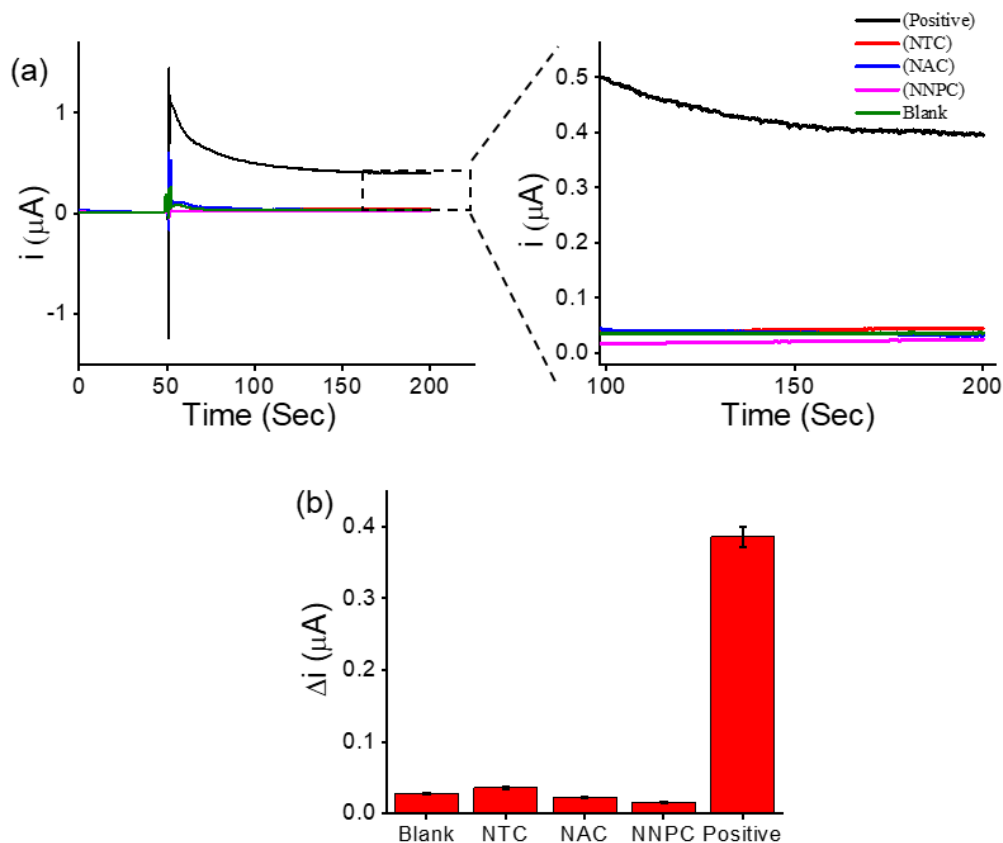


**Figure 3.4** Chronoamperometric responses obtained for positive and four control experiments. Positive = undiluted conditioned exosome media derived from OVCAR3 cells, NTC = Undiluted conditioned exosome media derived from Met5a cells, NAC = no-antibody control, NNPC = no-nanoparticle control. Inset in (a), enlarged view of the amperograms. (b) Corresponding  $\Delta i$ . Error bars represent the standard deviation of three repetitive experiments.

the surface of nanoscale C-IONPs (i.e. large surface area nanoscale C-IONPs allows a large number of CD9 antibodies on the surface) enhance the capture of the target exosomes via strong immunoaffinity interaction between a large number of active sites of C-IONPs/anti-CD9 and exosomes and (b) magnetic nanoparticle-based mixing, separation and purification steps further enhance the sensitivity by increasing capture efficiency and separating the target exosomes from the nontarget species present in the samples. This magnetic nanoparticle-based purification and collection of C-IONPs/anti-

CD9/Exo could also be one of the key factors to achieve such low background responses in the control experiments mentioned above. The direct immobilization of anti-CA-125 onto the extravidin-modified SPCE surfaces was followed by the blocking with 1% Bovine serum albumin (BSA) for 20 min. This step could also contribute to reduce the nonspecific adsorption of biological molecules onto the anti-CA-125/SPCE surfaces.

### 3.1.11 Assay Sensitivity

The sensitivity of our assay was tested by analyzing designated concentrations of OVCAR3-derived exosomes present in the cell-culture conditioned media. The samples were prepared by serial dilution of the media from 1:1 to 1:16 in the buffer, correlating to  $1 \times 10^7$  to  $6.2 \times 10^5$  exosomes/mL. The concentration of the exosomes present in the conditioned media was calculated using nanoparticle-tracking analysis (NTA) as outlined in previous report [19]. These samples were subjected to capture by the C-IONPs/anti-CD9 conjugates and subsequent identification by surface-bound CA-125 antibodies. We observed an increasing steady-state current (and thus an increased  $\Delta i$ ;  $\Delta i$  = steady-state current for an exosome solution – steady-state current for black response) with increases in the exosome concentration in the media (**Fig.3.5**).

This was attributed to the higher amount of the CA-125-specific exosomes being isolated and subsequently bound onto the electrode surface. The relative standard deviation (% RSD) of three independent measurements for the chronoamperometric readouts was calculated to be <5.0%, suggesting good reproducibility of our assay. This data clearly suggests that our approach could detect as low as  $1.25 \times 10^6$  exosomes/mL CA-125(+) exosomes from cell-culture media (based on the signal to background noise = 3). This limit of detection is much lower in magnitude than those of the existing immuno-affinity-based methods that rely on microfluidic-based isolation and/or plasmonic-based readouts [25-26], electrochemical biosensors [24-27], or conventional methods such as enzyme-linked immunosorbent assay (ELISA). The detection limit for ELISA methods is in the order of  $10^7$  exosomes/mL. The detection limit of our assay is also comparable to the ExoSearch microfluidic chip [28], NTA or qNano [29] methods (all are in the order of  $10^5$  exosomes/mL).

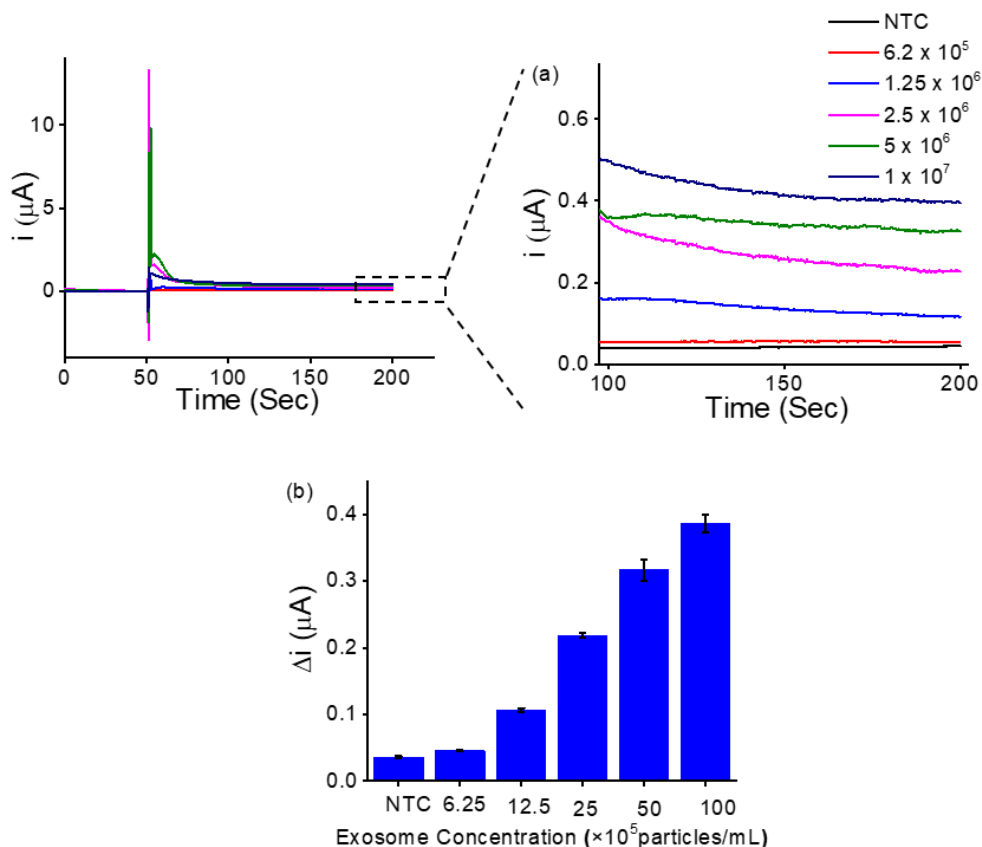


**Figure 3.5** Amperometric responses obtained for serially diluted conditioned media derived from OVCAR3 cells with known concentration of exosomes ( $1 \times 10^7$  to  $6.2 \times 10^5$  exosomes/mL). Inset in (a), enlarge view of the amperograms. (b) Corresponding  $\Delta i$ . Error bars represent the standard deviation of three repetitive experiment

However, this detection limit is several orders of magnitudes less sensitive than that of the highly sensitive electrochemical methods based on gold-loaded nanozymes ( $10^3$  exosomes/mL) [19], aptamer recognition-induced multi-DNA release and cyclic enzymatic amplification (70 exosomes/ $\mu\text{L}$ ) [30] and nanointerdigitated electrodes (5 extracellular vesicles / $\mu\text{L}$ ) [31].

We also compared the catalytic activity of natural enzyme such as horseradish peroxidase (HRP) towards HQ/ $\text{H}_2\text{O}_2$  reaction with that of C-IONPs used in our assay. Known concentrations of exosomes isolated using commercial kit were directly added to the anti-

CA-125 functionalized electrodes. Subsequently, HRP-conjugated anti-CD9 were added onto the sensor and chronoamperometric detection of exosomes was carried out using the optimal parameters described above. A much higher current response was obtained for HRP-catalysed HQ/H<sub>2</sub>O<sub>2</sub> reaction as compared to the C-IONPs used in our assay. A head-to-head comparison of current response obtained by using HRP with that of C-IONPs is shown in **Fig.3.6** and indicates that HRP catalyzed reaction generated much higher current response (i.e., approximately 10-times) and can provide higher sensitivity. Of note, HRP catalyzed reaction generated remarkably higher signal to background noise ratio for the lowest concentration of exosomes tested ( $6.25 \times 10^5$  exosomes/mL) as compared C-IONPs based assay.

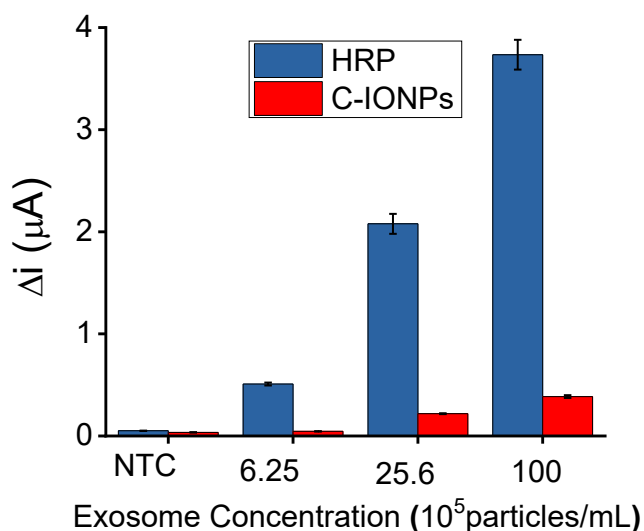


**Figure 3.6** Comparison of HRP and C-IONPs catalyzed HQ/H<sub>2</sub>O<sub>2</sub> reaction and the corresponding current response generated. HRP catalyzed reaction provided 9-11 times higher current response compared C-IONPs. Error bars represent the relative standard deviation of three experiments.

### 3.1.12 Analysis of Known concentration of Spiked Exosomes in Plasma Samples

Despite lower sensitivity in detection of exosomes in comparison to the HRP-based assay, our method offered a significant advantage in terms of kit-free direct isolation and

detection of exosomes from target samples. In order to demonstrate the applicability of our assay in direct isolation of exosomes from complex biological fluids, known concentrations of exosomes were spiked in human plasma samples. Two different known concentrations of exosomes ( $1.25 \times 10^6$  and  $1 \times 10^7$  exosomes/mL) were spiked with commercially obtained human plasma. Exosomes were then isolated from the spiked samples using C-IONPs/anti-CD9.

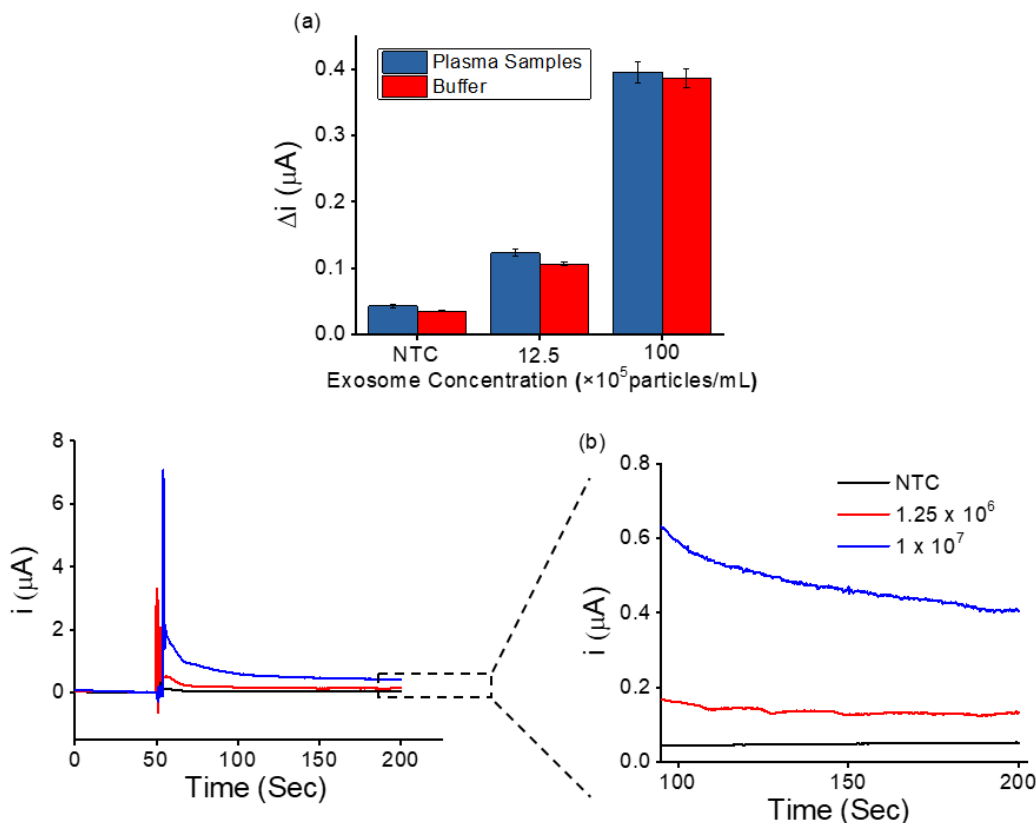


**Figure 3.7** Amperometric responses obtained for the analysis of known concentration of exosomes ( $1 \times 10^7$  and  $1.25 \times 10^6$  exosomes/mL). NTC corresponds to samples without exosomes. **(a)** Comparison of current responses obtained for spiked-in plasma and buffer (PBS) exosome samples. The inset in **(b)**, shows the enlarged view of the corresponding amperograms. Error bars represent the relative standard deviation of three experiments.

**Fig. 3.7a** shows a comparison of chronoamperometric response ( $\Delta i$ ) obtained for the exosomes isolated from spiked plasma samples, with that of buffer samples. As can be seen in **Fig. 3.7a**, an almost similar response was obtained for exosomes isolated from plasma samples as compared to buffer spiked samples for both the concentrations tested.

It is worthwhile to note here that for negative control (plasma samples without exosomes), a slightly higher but negligible current response was observed. The slightly higher response may indicate interference from non-specific biological molecules present in the complex sample matrix. However, similar to the buffer spiked exosome samples, our assay was still able to obtain a signal to background noise ratio of  $>3$  for the lowest concentration tested ( $1.25 \times 10^6$  exosomes/mL) indicating the potential of our assay for analyzing real samples. The corresponding chronoamperograms of spiked-in plasma samples are shown in **Fig. 3.7b**.

## Conclusions

In this work, carboxyl group-functionalized magnetic C-IONPs nanoparticles were used to develop a simple method for the direct isolation and quantification of disease-specific exosomes. Due to the presence of carboxylic acid  $-\text{COOH}$  groups on to their surface, the C-IONPs can potentially be conjugated to generic CD9 antibodies thus offer immense potential to be used as dispersible capture agents for exosomes separation and purification from complex sample media. In a proof-of-concept method, this study demonstrated the applicability of these nanoparticles for direct isolation and detection of CA-125 (+)-specific exosomes from the ovarian cell culture media. The method can specifically detect approximately  $6.2 \times 10^5$  exosomes/mL in the cell culture media. Although not demonstrated in this study, the detection limit of the method is highly suitable for analyzing disease-specific exosomes present in clinical samples (the average number of exosomes in most clinical samples ranges from  $1.0 \times 10^5$  to  $1 \times 10^9$  exosomes/ $\mu\text{L}$ ). The main advantage of this method is the use of C-IONPs both as dispersible nanocarrier and nanozymes. The method is not limited to the direct isolation and detection of CA-125 (+) exosomes, and can be extended to other exosomes derived from a diverse range of tumor types. Once the C-IONPs are synthesized and characterized, the method could be performed within 90 min and at a relatively cheap cost of less than US\$5 per run. Electrochemical detection using disposable screen-printed electrodes has other benefits. The use of these electrodes eliminates the need for a laborious and time-consuming electrode cleaning process typically used for conventional disk electrodes. The assay also avoids using natural enzymes for HQ/ $\text{H}_2\text{O}_2$  reaction, and thus reduces the cost, handling, and storage facilities generally required for natural enzymes such as HRP. As C-IONPs

shows high peroxidase-like activity for the oxidation of TMB in the presence of  $H_2O_2$  (TMB is a substrate for HRP in ELISAs), an additional advantage of these new materials would be to develop a wide range of ELISA-type sensing methods for various biomedical, plant, agriculture, and environmental applications.

## References

- [1] S. el Andaloussi, I. Mäger, X. O. Breakefield, and M. J. A. Wood, “Extracellular vesicles: biology and emerging therapeutic opportunities,” *Nature Reviews Drug Discovery* 2013 12:5, vol. 12, no. 5, pp. 347–357, Apr. 2013.
- [2] M. Yáñez-Mó, P. Siljander, ... Z. A.-J. of, and undefined 2015, “Biological properties of extracellular vesicles and their physiological functions,” *Taylor Fr.*, vol. 4, no. 2015, pp. 1–60, 2015.
- [3] M. Colombo, C. Moita, G. Van Niel, ... J. K.-J. of cell, and undefined 2013, “Analysis of ESCRT functions in exosome biogenesis, composition and secretion highlights the heterogeneity of extracellular vesicles,” *journals.biologists.com*, vol. 126, no. 24, pp. 5553–5565, Dec. 2013.
- [4] A. F *et al.*, “Tumor-derived exosomes: a new source of tumor rejection antigens,” *Vaccine*, vol. 20 Suppl 4, no. SUPPL. 4, Dec. 2002.
- [5] K. Boriachek *et al.*, “Biological Functions and Current Advances in Isolation and Detection Strategies for Exosome Nanovesicles,” *Small*, vol. 14, no. 6, p. 1702153, 2018.
- [6] K. O’Brien, K. Breyne, S. Ughetto, L. C. Laurent, and X. O. Breakefield, “RNA delivery by extracellular vesicles in mammalian cells and its applications,” *Nature Reviews Molecular Cell Biology* 2020 21:10, vol. 21, no. 10, pp. 585–606, May 2020.
- [7] A. S. Azmi, B. Bao, and F. H. Sarkar, “Exosomes in cancer development, metastasis, and drug resistance: A comprehensive review,” *Cancer Metastasis Rev.*, vol. 32, no. 3–4, pp. 623–642, Dec. 2013.
- [8] X. Zhang, X. Yuan, H. Shi, L. Wu, H. Qian, and W. Xu, “Exosomes in cancer: small particle, big player,” *J. Hematol. Oncol.* 2015 81, vol. 8, no. 1, pp. 1–13, Jul. 2015.
- [9] S. Principe, A. Hui, J. Bruce, A. Sinha, ... F. L.-, and undefined 2013, “Tumor-derived exosomes and microvesicles in head and neck cancer: Implications for tumor biology and biomarker discovery,” *Wiley Online Libr.*, vol. 13, no. 10–11, pp. 1608–1623, May 2013.
- [10] Y. S, C. H, S. B, and F. J, “Tumor-derived exosomes in cancer progression and treatment failure,” *Oncotarget*, vol. 6, no. 35, pp. 37151–37168, 2015.
- [11] H. Peinado, M. Alečković, S. Lavotshkin, I. M.-N. medicine, and undefined 2012, “Melanoma exosomes educate bone marrow progenitor cells toward a pro-metastatic phenotype through MET,” *nature.com*, vol. 18, no. 6, 2012.
- [12] A. Clayton *et al.*, “Analysis of antigen presenting cell derived exosomes, based on immuno-magnetic isolation and flow cytometry,” *J. Immunol. Methods*, vol. 247, no. 1–2, pp. 163–174, Jan. 2001.
- [13] T. C, A. S, R. G, and C. A, “Isolation and characterization of exosomes from cell culture supernatants and biological fluids,” *Curr. Protoc. cell Biol.*, vol. Chapter 3, no. 1, Mar. 2006.
- [14] D. Taylor, W. Zacharias, C. G.-T.-S. proteomics, and undefined 2011, “Exosome isolation for proteomic analyses and RNA profiling,” *Springer*, vol. 728, pp. 235–246, 2011.
- [15] M. L. Merchant *et al.*, “Microfiltration isolation of human urinary exosomes for



- characterization by MS,” *PROTEOMICS – Clin. Appl.*, vol. 4, no. 1, pp. 84–96, Jan. 2010.
- [16] S. Viswanathan, C. Rani, and J. A. A. Ho, “Electrochemical immunosensor for multiplexed detection of food-borne pathogens using nanocrystal bioconjugates and MWCNT screen-printed electrode,” *Talanta*, vol. 94, pp. 315–319, May 2012.
- [17] F. Y. Kong, B. Y. Xu, J. J. Xu, and H. Y. Chen, “Simultaneous electrochemical immunoassay using CdS/DNA and PbS/DNA nanochains as labels,” *Biosensors and Bioelectronics*, vol. 39, no. 1, pp. 177–182, Jan. 2013.
- [18] C. Frigerio, D. Ribeiro, ... S. R.-A. chimica, and undefined 2012, “Application of quantum dots as analytical tools in automated chemical analysis: a review,” *Elsevier*, vol. 735, pp. 9–22, 2012.
- [19] K. Boriachek *et al.*, “Avoiding pre-isolation step in exosome analysis: Direct isolation and sensitive detection of exosomes using gold-loaded nanoporous ferric oxide nanozymes,” *Anal. Chem.*, vol. 91, no. 6, pp. 3827–3834, Mar. 2019.
- [20] M. Liang and X. Yan, “Nanozymes: From New Concepts, Mechanisms, and Standards to Applications,” *Acc. Chem. Res.*, vol. 52, no. 8, pp. 2190–2200, Aug. 2019.
- [21] M. J. A. Shiddiky, M. A. Rahman, and Y. B. Shim, “Hydrazine-catalyzed ultrasensitive detection of DNA and proteins,” *Anal. Chem.*, vol. 79, no. 17, pp. 6886–6890, Sep. 2007.
- [22] M. J. A. Shiddiky, S. Rauf, P. H. Kithva, and M. Trau, “Graphene/quantum dot bionanoconjugates as signal amplifiers in stripping voltammetric detection of EpCAM biomarkers,” *Biosensors and Bioelectronics*, vol. 35, no. 1, pp. 251–257, May 2012.
- [23] de V. J *et al.*, “Quantification of nanosized extracellular membrane vesicles with scanning ion occlusion sensing,” *Nanomedicine (Lond.)*, vol. 8, no. 9, pp. 1443–1458, 2013.
- [24] S. Yadav *et al.*, “An Electrochemical Method for the Detection of Disease-Specific Exosomes,” *ChemElectroChem*, vol. 4, no. 4, pp. 967–971, Apr. 2017.
- [25] R. Vaidyanathan *et al.*, “Detecting Exosomes Specifically: A Multiplexed Device Based on Alternating Current Electrohydrodynamic Induced Nanoshearing,” *Anal. Chem.*, vol. 86, no. 22, pp. 11125–11132, Nov. 2014.
- [26] A. A. I. Sina, R. Vaidyanathan, S. Dey, L. G. Carrascosa, M. J. A. Shiddiky, and M. Trau, “Real time and label free profiling of clinically relevant exosomes,” *Sci. Reports 2016 61*, vol. 6, no. 1, pp. 1–9, Jul. 2016.
- [27] X. Doldán, P. Fagúndez, A. Cayota, J. Laíz, and J. P. Tosar, “Electrochemical Sandwich Immunosensor for Determination of Exosomes Based on Surface Marker-Mediated Signal Amplification,” *Anal. Chem.*, vol. 88, no. 21, pp. 10466–10473, Nov. 2016.
- [28] Z. Zhao, Y. Yang, Y. Zeng, and M. He, “A microfluidic ExoSearch chip for multiplexed exosome detection towards blood-based ovarian cancer diagnosis,” *Lab Chip*, vol. 16, no. 3, pp. 489–496, Jan. 2016.
- [29] E. Koritzinsky, J. Street, ... R. S.-J. of cellular, and undefined 2017, “Quantification of exosomes,” *Wiley Online Libr.*, vol. 232, no. 7, pp. 1587–1590, Jul. 2017.
- [30] H. Dong, H. Chen, J. Jiang, H. Zhang, C. Cai, and Q. Shen, “Highly Sensitive

Electrochemical Detection of Tumor Exosomes Based on Aptamer Recognition-Induced Multi-DNA Release and Cyclic Enzymatic Amplification,” *Anal. Chem.*, vol. 90, no. 7, pp. 4507–4513, Apr. 2018.

- [31] D. Mathew, P. Beekman, S. Lemay, H. Z.-N., and undefined 2019, “Electrochemical detection of tumor-derived extracellular vesicles on nanointerdigitated electrodes,” *ACS Publ.*, vol. 20, no. 2, pp. 820–828, Feb. 2019.

## CHAPTER FOUR

Detection and quantification of DNA methylation using functionalized iron oxide (C-IONPs) based nanozymes



## CHAPTER FOUR

---

### **4 Detection and quantification of DNA methylation using functionalized iron oxide (C-IONPs) based nanozymes**

#### **Introduction**

Formation and maintenance of specific DNA methylation patterns is a prerequisite for proper cellular functioning. Thus, aberrations in normal DNA methylation patterns and levels underlie a range of diseases including cancers [1]. Altered DNA methylation is a defining feature in almost all types of cancers and is considered to be among the earliest aberrations that lead to malignant transformation of cells. Cancer cells are characterized by two distinct yet concurrent changes in DNA methylation: an overall genome-wide decrease in DNA methylation levels (i.e., global hypomethylation), and focal hypermethylation mostly at gene promoter associated CpG islands (i.e., regional hypermethylation). Because of the key role that it plays in carcinogenesis and ubiquitous occurrence in a variety of cancers, there has been a great deal of interest in exploring the potential of DNA methylation as diagnostic and prognostic biomarker for cancers [2-3]. Likewise, development of methods for DNA methylation analysis have also been a major research focus in recent years.

Although locus specific changes in DNA methylation are an important cancer marker, extensive efforts may be required to identify and validate aberrantly methylated genomic regions which can provide a highly specific cancer diagnosis. Patterns of aberrant regional methylation differ significantly between various cancers. There is also a considerable interpatient variation in these DNA methylation marks between patients suffering from same type of cancer, or even intra-patient variation depending upon the stage of the disease. Global hypomethylation of the genome was the first epigenetic abnormality described in human cancers and is associated with genomic instability, reactivation of retrotransposons, and loss of imprinting. In contrast to locus specific hypo- or hypermethylation, global hypomethylation is a ubiquitous early-stage marker common to almost all cancers. It has been reported that global hypomethylation may appear at early stages of cancers, in some cases even in benign precursors of malignant tumors. Therefore, global hypomethylation is a promising universal biomarker for early detection of cancer and can potentially be used in development of platforms for rapid assessment of disease progression as well as prognostic and theragnostic outcomes [4].

Biggest challenge in analysis of global DNA methylation levels via conventional methods is that most of them require several micrograms of DNA sample. For example HPLC based methods require anywhere between 3-50  $\mu\text{g}$  of DNA [5]. LC-MS/MS-based assays or Luminometric Methylation Assay (LUMA) is among the most commonly used methods for analysis of global DNA methylation levels. However, it relies on specialized instrumentation and enzymatic treatment of DNA [6]. Similarly, spectroscopic/fluorescent detection based [7-8], or dark-field microscopy-based methods [9] have also been reported but they involve enzymatic treatment and amplification [10], cumbersome processing [11], or in other case bulky equipment is required [12]. Pyrosequencing of LINE-1 repeat regions is an excellent method that has been used to indirectly estimate the global DNA methylation levels. However, it requires bisulfite conversion, which may degrade up to 99% of the DNA, as well PCR amplification thus increasing the cost and processing time. Immunoquantification of global 5mC content via enzyme-linked immunosorbent assay (ELISA) is a well-established method. ELISA may require as little as 10 ng of input genomic DNA and is well suited for routine clinical analysis. However, in a comprehensive comparison of various DNA methylation analysis methods conducted by The BLUEPRINT consortium, it was found that ELISA results did not agree well with the characteristics of the reference samples, raising questions about the reliability of its application in complex samples [13]. Therefore, a simple yet efficient and robust method that can utilize relatively lower amounts of input DNA may be required for global DNA methylation analysis.

In recent years, electrochemical biosensors have been developed as promising low cost and simpler alternatives for biomarker detection, including DNA methylation, in biological samples. Ergo, a large number of electrochemical platforms for DNA methylation analysis have been reported over the years [14-18], including a series of platforms our group has previously reported for profiling both locus specific and global DNA methylation levels [19-23] Likewise, optical (including colorimetric) [24-25], surface enhanced Raman spectroscopy (SERS) based [26], and surface plasmon resonance (SPR) based DNA methylation analysis platforms have been developed [27].

Nanomaterials-driven biomolecule sensing methods have also emerged as up-and-coming approaches due to the inherent versatility and facile tunability of nanomaterials. Nanomaterials in biosensing have been used as optical probes, electronic conductors, as well as nanozymes [28-29]. Moreover, several multifunctional nanomaterials have been developed in recent years

that can be easily bioconjugated to DNA and antibody probes and thus can selectively capture and isolate target analytes from complex samples [30]. Leveraging these multifaceted characteristics of rationally designed nanomaterials, efforts have been made to develop efficient epigenetic analysis platforms for various applications [23,31-33]. I have synthesized a novel class of carboxyl group ( $-\text{COOH}$ ) functionalized magnetic iron oxide nanoparticles (C-IONPs) that was discussed in the previous chapter (**in chapter 2**). These particles are magnetic and therefore can easily be used as dispersible capture agents to isolate circulating biomarkers present in biological samples. These C-IONPs can be efficiently conjugated to  $-\text{NH}_2$  group containing biomolecules (e.g., antibodies). Moreover, these C-IONPs exhibit peroxidase mimicking activity and can be used as nanozymes. These functionalities of C-IONPs have been used to develop a method for direct isolation and detection of exosomes in complex biological samples (**in chapter 3**).

Herein, I report a proof-of-concept method for analysis of global DNA methylation in synthetic samples as well as DNA derived from cultured cells. This method utilizes C-IONPs covalently conjugated to anti-5mC antibodies via EDC/NHS coupling chemistries. First, anti-5mC/C-IONPs were mixed with target DNA. Acting as nanosized capture agents the anti-5mC/C-IONPs specifically bind to the methylated fraction of genome. The methylated DNA molecules are subsequently magnetically isolated followed by direct adsorption onto a gold electrode via gold-DNA affinity interaction [34]. The electrochemical quantification of global DNA methylation levels was achieved by differential pulse voltammetric measurement of reduction current of target-bound cationic  $[\text{Ru}(\text{NH}_3)_6]^{3+}$  which was electrostatically attached with the anionic phosphate backbone of the adsorbed target DNA.

## **Materials and methods**

### **4.1.1 Materials**

All reagents and chemicals were of analytical grade and used without further purification. CpG Methylated Human Genomic DNA (100% methylated DNA, mDNA) was purchased from ThermoFisher Scientific (Cat # SD1131). REPLI-g whole genome amplification (WGA) mini kit (Cat # 150025), QIAquick PCR purification kit, and Blood and Cell Culture DNA Mini Kit (Cat # 13323) were acquired from Qiagen (Hilden, Germany). Ferric nitrate nonahydrate  $\text{Fe}(\text{NO}_3)_3 \cdot 9\text{H}_2\text{O}$  and starch (soluble) were purchased from Merck (Germany). Dopamine

hydrochloride, succinic anhydride, toluene, and tris buffer were purchased from Sigma Aldrich (Australia). Dimethyl sulfoxide (DMSO) from Chem-Supply and TMB  $\geq 98.0\%$  were purchased from Sigma Life Science (Australia). Screen-printed gold electrodes (SPGE, DRP-250BT) were acquired from Metrohm Dropsens (Spain).

#### **4.1.2 Preparation of DNA Samples**

Ovarian cancer cell lines SKOV3 and OVCAR3 and one non-cancerous cell line Met5a were purchased from American Type Culture Collection (ATCC), USA. Cells were cultured in RPMI-1640 growth medium supplemented with 10% fetal bovine serum (FBS) and 1% penicillin/streptomycin (Life Technologies, Australia) in a humidified incubator at 37 °C with 5% CO<sub>2</sub>. DNA was isolated from the cells using Blood and Cell Culture DNA Mini Kit. Fully unmethylated (0% methylated) genomic DNA (umDNA) was prepared by whole genome amplification (WGA) of SKOV3 DNA using REPLI-g mini kit as per manufacturer's recommendations and purified using QIAquick PCR purification kit.

#### **4.1.3 Preparation of Anti-5mC Conjugated C-IONPs (5mC/C-IONPs)**

Antibodies against 5mC (Abcam ab73938) were conjugated to C-IONPs through EDC/NHS coupling following previously reported protocol [35]. Briefly, 1 mg C-IONPs dispersed by sonication in 0.1 M MES buffer pH 5 were washed 3 times with MES buffer and resuspended evenly in 500  $\mu$ L MES buffer by repeated pipetting. EDC and NHS have added to the solution in the ratio C-IONPs: EDC: NHS = 1:4:6 mg and incubated for 15 minutes at 37 °C with continuous rotation. The particles were separated magnetically from the reaction mixture and mixed with 500  $\mu$ L of anti-5mC antibody (10  $\mu$ g mL<sup>-1</sup>) diluted in 10 mM PBS buffer pH 7.4 (C-IONPs: anti-5-mC = 1mg: 5 $\mu$ g) followed by overnight incubation at 4 °C with continuous rotation. After 3 times washing with PBS buffer, antibody conjugated C-IONPs were resuspended in 1 mL PBS buffer. To verify the successful conjugation of C-IONPs with the anti-5mC antibody FTIR spectra for both conjugated and unconjugated. C-IONPs were recorded in the range of 500 - 4000 cm<sup>-1</sup> on a Nicolet 5700 FT-IR spectrometer (Nicolet Inc., Madison, USA) by transmission FTIR spectroscopy.

#### 4.1.4 Electrochemical Detection of Global DNA Methylation

DNA samples with designated levels of DNA methylation (0%, 5%, 25%, 50%, 75%, 95%, and 100%), referred to as standards from hereon, were prepared by mixing appropriate volumes of mDNA and umDNA. Cell line DNA and standards were diluted with 5X saline sodium citrate (5X-SSC) buffer (pH 4) to a final concentration of  $4 \text{ ng}\mu\text{L}^{-1}$ . 50  $\mu\text{L}$  of DNA samples were denatured at 95 °C to obtain ssDNA and quickly transferred to ice. Unless otherwise stated, all incubations were carried out at room temperature with gentle shaking. To capture methylated fraction of the DNA, 20  $\mu\text{L}$  of anti-5mC/C-IONPs were mixed with 50  $\mu\text{L}$  of denatured DNA samples and incubated for 30 minutes. After incubation, methylated DNA captured by anti-5mC/C-IONPs was magnetically separated and washed 3 times with 5X SSC buffer before finally being resuspended in 50  $\mu\text{L}$  5X SSC buffer. Unless otherwise stated, each of the following steps was followed by 3 times washing of the electrodes with tris-buffer (pH 7.4) and air drying. The captured DNA samples were dropped onto the working electrode of electrochemically cleaned SPGE and allowed to adsorb for 10 minutes. Next, 50  $\mu\text{L}$  of 50  $\mu\text{M}$   $[\text{Ru}(\text{NH}_3)_6]^{3+}$  was dropped onto the electrode and incubated for 5 minutes. Amount of DNA adsorbed onto the electrode surface was interrogated electrochemically by differential pulse voltammetry (DPV) using a CH1040C potentiostat in the presence of 10 mM tris-buffer. DPV measurements were conducted at room temperature with the following parameters: potential step 4 mV, pulse amplitude 50 mV, pulse width of 50 ms, and pulse period 500 ms. At least three replicates were measured for each sample and standard.

### Result and discussion

#### 4.1.5 FTIR Analysis of C-IONPs and Anti-5mC/C-IONPs

Surface functionalization of iron oxide with terminal moieties like –COOH groups provides a suitable base for attachment of biotargeting entities like antibodies and nucleic acids. These biotargeting entities permit specific recognition of target analyte/biomarker thus enabling the use of iron oxide particles in biomedical applications. Carbodiimide crosslinking of –COOH functional groups with the –NH<sub>2</sub> groups present in proteins (both at amino terminal as well as arginine, lysine, and histidine side chains) is one of the simplest and straightforward bioconjugation strategies (**Fig. 4.1**) and has been widely used for anchorage of protein and –NH<sub>2</sub> group functionalized DNA probes onto the surface of terminal –COOH group containing



NPs. EDC/NHS coupling reaction was used to conjugate the anti-5mC to C-IONPs. FTIR spectroscopy analysis of both unconjugated and anti-5mC conjugated C-IONPS was carried out to confirm the successful conjugations can be seen in FTIR (**Fig. 4.2**) analysis,

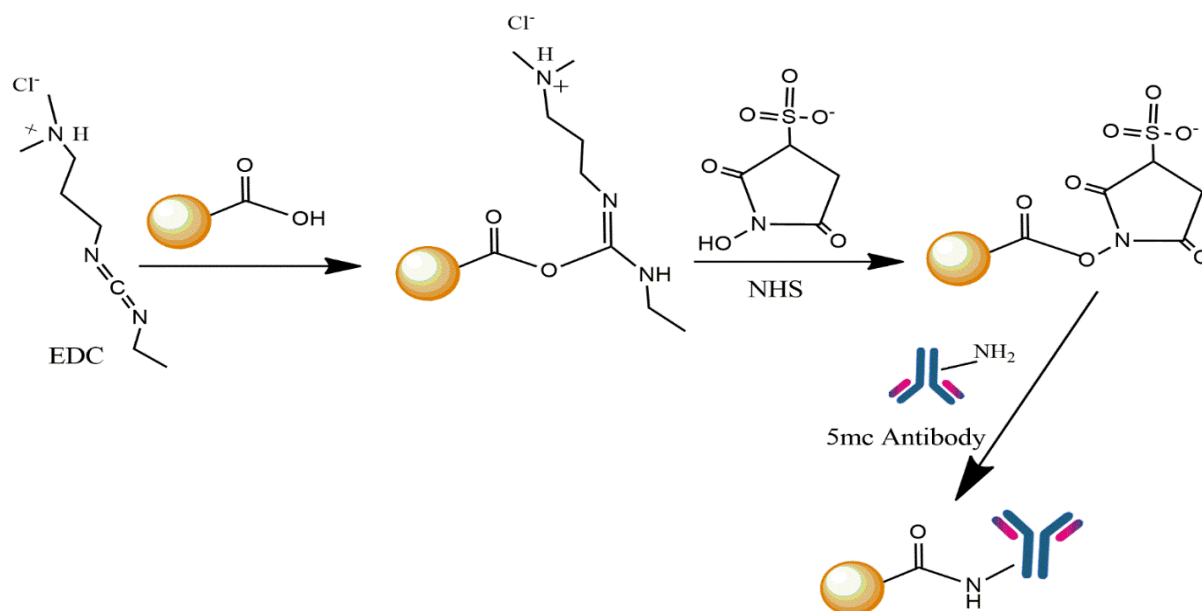


**Figure 4.1** Conjugation of anti-5mC antibody with C-IONPs by EDC/NHS coupling chemistries.

For C-IONPs without conjugate with anti-5mC, the absorption peak at  $1698\text{ cm}^{-1}$  was emerged for C=O stretching for amide bond. The strong peak at  $1732\text{ cm}^{-1}$  and  $2600\text{-}3200\text{ cm}^{-1}$  indicated C=O and O-H stretching for carboxylic acid. On the other hand, many new peaks were observed in anti-5mC conjugate C-IONPs. Most important among these, considered to be the characteristic peaks of amide bonds, were a strong peak at  $1652\text{ cm}^{-1}$  due to stretching of associated C=O primary amide and a medium peak around  $3500\text{ cm}^{-1}$  attributable to amide N-H stretch.

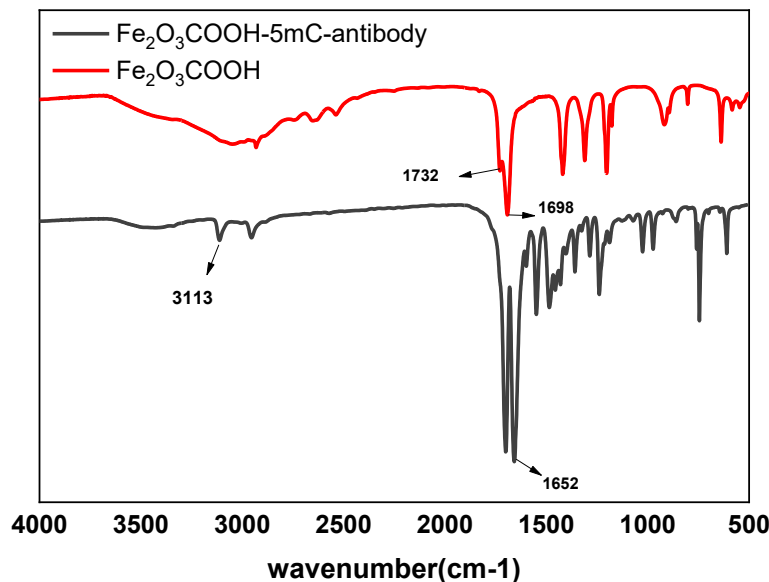


**Figure 4.2** FTIR analysis of C-IONPs and anti-5mC/C-IONPs

#### 4.1.6 Principal of *e*-MagnetoMethyl IP Method

The working principle of *e*-MagnetoMethyl IP is schematically presented in **Fig. 4.3** and is comprised of three steps. i) Anti-5mC/C-IONPs are mixed with the DNA samples which leads to the binding of methylated fraction of DNA with the antibody functionalized C-IONPs. Methylated DNA is then “pulled down” or magnetically separated from the unmethylated portion of DNA ii) Magnetically immunoprecipitated DNA is directly adsorbed onto the SPGE via gold-DNA affinity interaction. iii) Using positively charged redox molecules,  $[\text{Ru}(\text{NH}_3)_6]^{3+}$ , amount of DNA adsorbed on the gold electrode surface is electrochemically estimated. In this method, the total amount of immunocaptured, isolated, and adsorbed DNA onto the gold electrode in steps 1 and 2 is directly proportional to the level of methylation in the target DNA sample. In step 3, the electrochemical estimation of electrode-adsorbed DNA (and hence the DNA methylation) was achieved by measuring the reduction current of  $[\text{Ru}(\text{NH}_3)_6]^{3+}$  (i.e.  $[\text{Ru}(\text{NH}_3)_6]^{3+} + e \rightarrow [\text{Ru}(\text{NH}_3)_6]^{2+}$ ).  $[\text{Ru}(\text{NH}_3)_6]^{3+}$  is a positively charged transition metal complex that shows unique electroactive behavior on the surface of DNA modified electrodes and has been widely used as a redox indicator for electrochemical estimation of DNA.

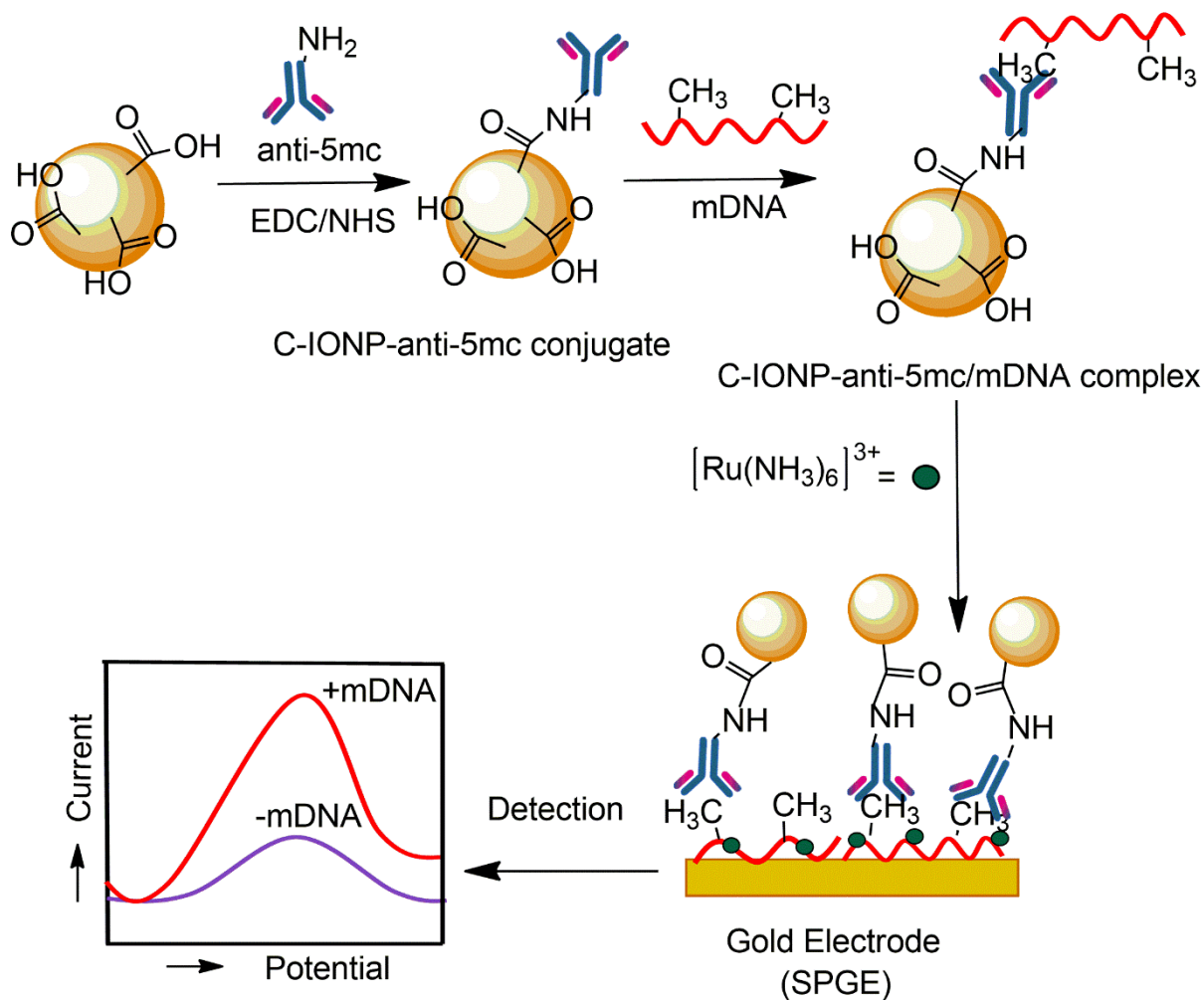


**Figure 4.3** Schematic representation of the e-MagnetoMethyl IP method. Methylated DNA is subjected to anti-5mC/C-IONPs mediated immunoprecipitation (IONPs-anti-5mC/mDNA complex). Immunoprecipitated DNA is adsorbed directly onto the SPGE surface and electrochemically detected as a function of current response generated by the reduction of DNA backbone-bound  $[\text{Ru}(\text{NH}_3)_6]^{3+}$  molecules.

$[\text{Ru}(\text{NH}_3)_6]^{3+}$  molecules lack planar aromatic groups so they cannot intercalate into DNA base pairs. Therefore, in a solution of low ionic strength,  $[\text{Ru}(\text{NH}_3)_6]^{3+}$  molecules exchange with the native charge compensation cations and associate with the DNA phosphate backbone solely based on their electrostatic interaction. Moreover, it has been proved previously that under conditions of saturation coverage  $[\text{Ru}(\text{NH}_3)_6]^{3+}$  provides complete charge compensation thus electrostatic determination of the amount of electrostatically trapped  $[\text{Ru}(\text{NH}_3)_6]^{3+}$  provides a direct estimation of the amount of DNA present on the electrode surface [36]. Increasing the

concentration/amount of DNA on the electrode surface will lead to an increased accumulation of  $[\text{Ru}(\text{NH}_3)_6]^{3+}$  molecules and a corresponding increase in current response. Combining this principle with the highly selective anti-5mC mediated capture of the methylated fraction of DNA and efficient magnetic separation characteristics of our novel C-IONPs, our assay provided a simple yet powerful strategy for accurate and sensitive estimation of global DNA methylation content in heterogeneous samples.

#### 4.1.7 Functionality and Selectivity of the Assay

To test the functionality of our assay, anti-5mC/C-IONPs were mixed with fully 100% methylated (mDNA) and fully unmethylated (umDNA) samples. An average peak current density of  $37.52 \mu\text{Acm}^{-2}$  (%RSD = 2.97 for  $n = 3$ ) was obtained for mDNA samples. In contrast, the average current density for umDNA samples was found to be  $17.92 \mu\text{Acm}^{-2}$  (%RSD = 3.2 for  $n = 3$ ). Representative DPV voltammograms obtained for the methylated and unmethylated samples are depicted in **Fig. 4.4a**. Clearly, a >2-fold increase in current response was resulted for mDNA compared to umDNA samples, indicating the feasibility of our method for the detection of global DNA methylation levels.

As optimal analytical performance of a biosensor is highly dependent upon the experimental conditions, we also sought to optimize parameters that might influence the capture efficiency of anti-5mC/C-IONPs as well as DNA-gold adsorption kinetics. Incubation time of antibody functionalized C-IONPs with the DNA samples is a crucial parameter as increased incubation times may lead to increased non-specific binding of DNA on C-IONPs surface. On the other hand, decreased incubation times may lead to reduced capture efficiency. I incubated both mDNA and umDNA samples with anti-5mC/C-IONPs for different time periods (10, 20, 30, 45, and 60 minutes) and recorded the current response obtained. Triplicate experiments were conducted for each time point (both mDNA and umDNA). Gradual increase in the current response was observed for mDNA between increasing incubation time from 10-30 minutes. However, after 30 minutes incubation no further increase in current response was observed. umDNA did not show a substantial increase in current response up to 45 minutes of incubation. However, after 60 minutes incubation slight increase in current response was observed (data not shown). Therefore, 30 minutes incubation of anti-5mC/C-IONPs with DNA samples was selected as optimum. Shiddiky groups previously demonstrated that 10 minutes incubation time is sufficient to provide optimal adsorption of human genomic DNA onto the commercial 4.0

mm-diameter SPGE [23-37]. Therefore, an optimized incubation time of 10 minutes was selected.

The specificity of the electrochemical signal observed in the assay is vital as several factors may contribute to the generation of non-specific responses. To unambiguously establish that the current response observed is primarily due to the  $[\text{Ru}(\text{NH}_3)_6]^{3+}$  bound to DNA, we conducted several control experiments. Firstly, a no-target control (NTC) assay was carried out where 20  $\mu\text{L}$  of anti-5mC/C-IONPs were added to 50  $\mu\text{L}$  of 5X-SSC buffer.

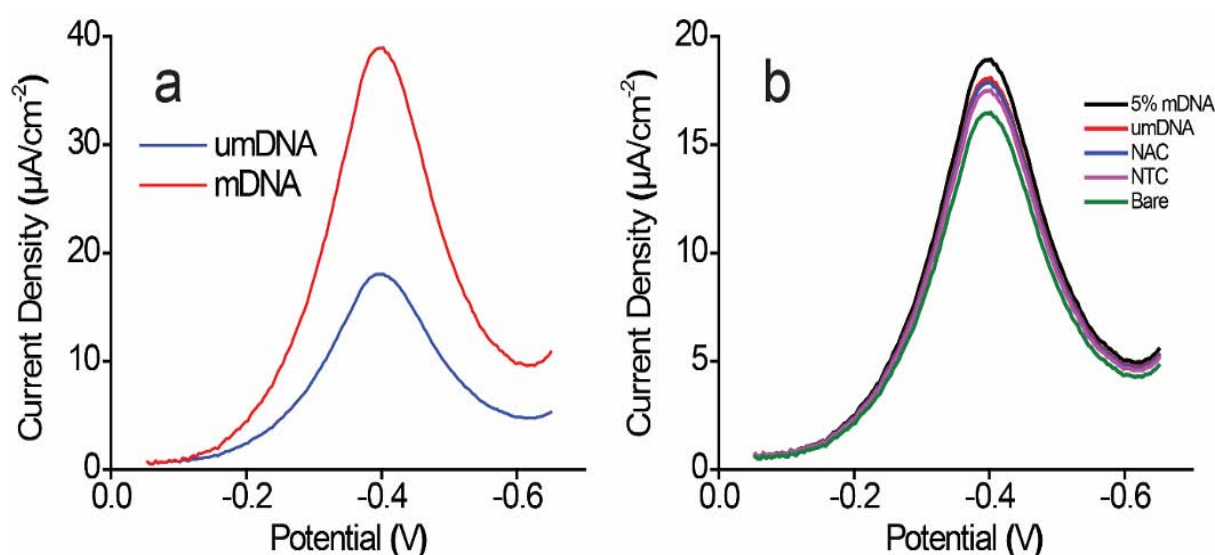


**Figure 4.4 (a)** Functionality of e-MagnetoMethyl IP method.  $\sim 2.5$ -fold higher current response was obtained for mDNA (100% methylated DNA) compared to umDNA (0% methylated DNA). **(b)** Specificity of the assay. Current response obtained by NTC (no-target control), NAC (C-IONPs not conjugated to anti-5mC) and bare electrode was significantly lower compared to sample with 5% methylated DNA. DPV measurements were conducted at room temperature in the presence of 10 mM tris-buffer (pH 7.4).

As the sample did not contain any DNA, theoretically negligible current response was expected. For the representative voltammograms shown in **Fig. 4.4b**, the peak current response obtained for NTC and umDNA samples were 17.51 and 18.07  $\mu\text{A}/\text{cm}^2$ , respectively. Thus, current response obtained for NTC was slightly lower or almost similar to the one obtained for umDNA (average 17.06  $\mu\text{A}/\text{cm}^2$ , %RSD = 3.65% for  $n = 3$  vs 17.92  $\mu\text{A}/\text{cm}^2$  for umDNA), clearly indicating the specificity of the signal obtained in our assay.

It has previously been shown that under acidic pH conditions the amino groups in polydopamine may undergo protonation leading to an overall positively charged surface [33], as DNA is negatively charged, this might lead to non-specific adsorption of DNA molecules onto the PD coated IONPs. As our capture reaction is conducted primarily at acidic condition (pH 4), this effect may interfere with the specificity of signal. In order to test whether this suspected non-specific adsorption has any effect on the selectivity of the final current response observed in our assay, C-IONPs not conjugated to anti-5mC were mixed with mDNA (no-antibody control, NAC). As can be seen in **Fig. 4.4b**, NAC samples showed a current response similar to umDNA and NTC (average peak current  $17.82 \mu\text{Acm}^{-2}$ , %RSD = 1.87% for  $n = 3$ ). Although the surface charge characteristics of our novel C-IONPs are currently not well understood, based on the current results it can be inferred that negatively charged DNA does not interact non-specifically with carboxyl functionalized IONPs. It might be due to the fact that amine groups present on PD surface have been efficiently masked during the succinic anhydride based  $-\text{COOH}$  group functionalization.

In order to rule out the possible non-specific adsorption of  $[\text{Ru}(\text{NH}_3)_6]^{3+}$  molecules on SPGE, I also tested the current response obtained after incubation of  $[\text{Ru}(\text{NH}_3)_6]^{3+}$  with a clean fresh SPGE (without DNA). For the bare electrode reaction, 50  $\mu\text{L}$  of 50  $\mu\text{M}$   $[\text{Ru}(\text{NH}_3)_6]^{3+}$  solution was directly dropped onto a clean bare gold electrode and incubated for 5 minutes, followed by 3X PBS washing and air drying. The average peak current response obtained for bare electrode was lower compared to other controls ( $16.60 \mu\text{Acm}^{-2}$ , %RSD = 1.04% for  $n = 3$ ). Lower current response obtained for bare electrode compared to NTC and NAC shows that the lower amount of  $[\text{Ru}(\text{NH}_3)_6]^{3+}$  molecules which may get trapped non-specifically, due to the nanosized asperities present on SPGE surface and other non-specific molecular interactions. On the other hand, a slightly higher current obtained for NTC and NAC compared to the bare electrode may indicate slight non-specific adsorption of  $[\text{Ru}(\text{NH}_3)_6]^{3+}$  on to the SPGE surface. Mixing anti-5mC/C-IONPs with a sample containing as low as 5% methylated DNA generated a significantly higher current response (average peak current  $18.53 \mu\text{Acm}^{-2}$ , %RSD = 2.06% for  $n = 3$ ) suggesting the effect of background noise is negligible (**Fig. 4.4b**).

#### 4.1.8 Analysis of Heterogeneous DNA Methylation

In order to demonstrate the applicability of our assay to analyze heterogeneous levels of DNA methylation, we mixed commercially available 100% methylated DNA (mDNA) with fully

unmethylated WGA DNA (umDNA) in designated proportions to prepare a series of standards with 0%, 5%, 25%, 50%, 75%, 95%, and 100% DNA methylation levels. As can be seen in **Fig. 4.5a**, a current response corresponding to the percentage of methylation in starting sample was observed.

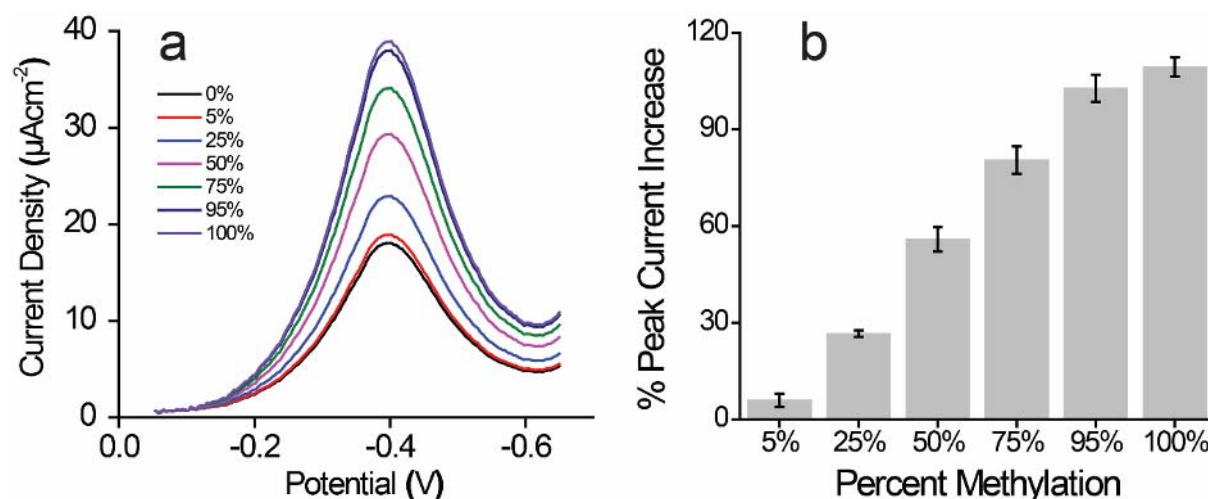


**Figure 4.5(a)** Differential pulse voltammetry analysis of heterogeneous DNA methylation levels. DPV current changes are corresponding to level of DNA methylation in different samples. **(b)** Average percent change in DPV current responses obtained for various DNA methylation levels. DPV measurements were conducted at room temperature in the presence of 10 mM tris-buffer (pH 7.4). Each data point represents the average of three separate measurements, and error bars represent the standard deviation of measurements (%RSD = < 5% for n = 3).

More importantly, our assay was able to reliably differentiate between methylation differences as low as 5% (**Fig. 4.5a**). Percent change in DPV current response was calculated as follows:

$$\% \text{ Increase in current response} = (I_{\text{std}} - I_{\text{umDNA}}) / I_{\text{umDNA}} \times 100 \dots \dots (1)$$

Where  $I_{\text{std}}$  is the current response obtained for sample of known DNA methylation percentage while  $I_{\text{umDNA}}$  is the current response obtained for 0%, or unmethylated DNA sample. Average percent change in DPV current densities ( $n = 3$ ) observed for all the standards are given in **Fig.**

**4.5b.** The error bars represent %RSD and were <5% indicating the intra-assay precision of our method.

Considerable heterogeneity in the DNA methylation levels is observed in real biological samples and small differences may have significant clinicopathological consequences. It has been shown that different stages of cancer are correlated with different global methylation levels. Moreover, CpG sites in human genome occur in very low frequencies (1/100 bp on the average) [34], thus 5mC forms only a very small portion of genomic DNA. Similarly, circulating cell free DNA (cfDNA) originated from tumor cells (ctDNA) is an attractive target for development of DNA methylation analysis based minimally invasive modalities for cancer diagnosis and monitoring [35]. However, ctDNA comprises only a very tiny fraction of the cfDNA repertoire. Thus, there are two major challenges: i) detection of low levels of methylated DNA, and ii) reliable differentiation between subtle changes in DNA methylation levels. Our assay was able to address both of these challenges by reproducibly detecting methylation levels as low as 5% amongst 95% unmethylated DNA molecules and by differentiating between methylation differences as low as 5% (compare 0% vs 5% and 95% vs 100%). This detection performance of our method is either comparable or better than that of the previously reported nanotechnology-based global DNA methylation methods [20-23]. For example, Wang *et al.* developed an SERS based platform for the detection of as low as 6.25% changes in global methylation levels [23]. Similarly, Shiddiky group have previously reported a porous nanozymes based global DNA methylation detection platform which could detect 10% methylation differences [20]. Thus, my method introduces an improvement to these methods. In addition, our method does not rely on enzymatic processing DNA processing [23] or rely on additional enzymatic reactions (TMB/H<sub>2</sub>O<sub>2</sub>) for the generation of electrochemical signal [20]. Although two methods reported earlier did achieve a resolution of 5% methylation difference, both the methods similarly relied on enzymatic DNA processing [36] or TMB/H<sub>2</sub>O<sub>2</sub> reaction [16]. In comparison, our current method introduces an enzyme-free and label-free approach with similar analytical resolution.



#### 4.1.9 Analysis of DNA Methylation in Cell Lines

In order to test the applicability of our method to complex biological samples, I isolated genomic DNA from two ovarian cancer cell lines namely SKOV3 and OVCAR3. I used immortalized human mesothelial cell line Met5a as normal control. The genomic DNA was processed as described earlier. The Current response obtained after adsorption of cell line DNA onto the gold electrode is shown in **Fig. 4.6**

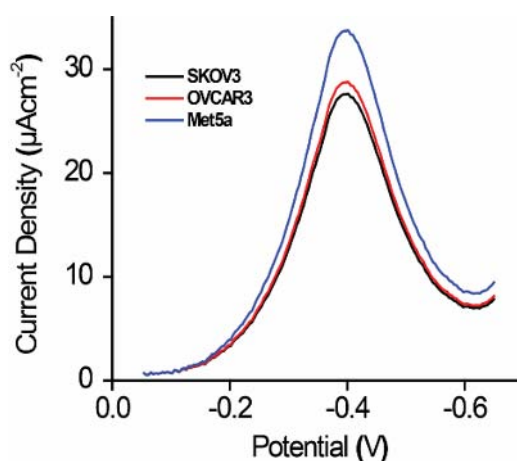


**Figure 4.6(a)** Differential pulse voltammetry analysis of heterogeneous DNA methylation levels. DPV current changes are corresponding to level of DNA methylation in different samples. **(b)** Average percent change in DPV current responses obtained for various DNA methylation levels. Each data point represents the average of three separate measurements, and error bars represent the standard deviation of measurements (%RSD = < 5% for  $n = 3$ ). DPV measurements were conducted at room temperature in the presence of 10 mM tris-buffer (pH 7.4).

As can be seen, cancer cell lines showed significantly reduced current response, indicative of lower methylation levels, as compared to the normal cell line. The average current densities obtained for non-cancerous Met5a cell line was  $31.89 \mu\text{Acm}^{-2}$  (%RSD = 4.24 for  $n = 3$ ) (average current densities for 75% methylation standard was  $32.35 \mu\text{Acm}^{-2}$ , see **Fig 4.5b**). On the other hand, average current densities obtained for the OVCAR3 and SKOV3 cell lines were 28.12 (%RSD = 4.75 for  $n = 3$ ) and  $27.5 \mu\text{Acm}^{-2}$  (%RSD = 3.52 for  $n = 3$ ) respectively (average current densities for 50% methylation standard was  $27.95 \mu\text{Acm}^{-2}$ ). Reduced levels of global

DNA methylation are found in cancer cells in comparison to normal cells. These data for all the cell lines were in accordance with previous reports [37-38]. Thus, our assay accurately differentiated between normal and cancer cells. Furthermore, the assay also showed good reproducibility as inter-assay %RSD was found to be <5% (n =3).

Several novel biosensors have been reported for analysis of cellular DNA methylation content and patterns [39]. Most approaches, however, have targeted gene specific (regional) DNA methylation patterns [11-12,40]. Various global DNA methylation assessment platforms have also been reported. However, they either include bisulfite treatment [16] or rely on enzymatic processes for signal generation [19-20,41]. In comparison, my assay provides several advantages which could pave the way for development of rapid global DNA methylation quantification platforms. Firstly, coupling a well-established anti-5mC based enrichment of methylated DNA with the magnetic properties of our nanoparticles can provide a very efficient method for enrichment of low levels of methylated DNA sequences. Secondly, my approach relies on direct adsorption of enriched DNA onto unmodified gold electrodes in contrast to some of the previously reported methods which involve multistep sensor functionalization steps [42]. Although the amount of input DNA used in our method is relatively higher compared to some of the earlier reported methods (e.g., 0.2 ng [23] and 50 ng [20]), our method is simpler yet provided sensitivity and reproducibility comparable to these methods or the other previously reported HRP/TMB/H<sub>2</sub>O<sub>2</sub> enzymatic reaction based electrochemical DNA methylation detection approaches [16]. Taken together our results demonstrate the excellent performance of C-IONPs in accurately capturing methylated DNA from heterogeneous samples with high sensitivity.

## **Conclusions**

In this work, carboxyl group functionalized magnetic Fe<sub>2</sub>O<sub>3</sub> nanoparticles was used for development of the e-MagnetoMethyl IP method for the estimation of global DNA methylation level in biological samples. Using only 200 ng of input DNA, our method could detect as low as 5% methylation in heterogeneous samples. The method is also suitable for quantifying different global methylation levels in normal and cancer cell line samples. The use of the magnetic nanoparticles and 5-mC antibody-induced immunocapture/collection of methylated DNA make the method highly specific and relatively simpler than the conventional bisulfite treatment and asymmetric PCR amplification based methods. The use of direct affinity

interaction of target DNA onto the disposable screen-printed electrodes also further simplifies the method by avoiding laborious electrode cleaning procedures or complicated sensor fabrication steps. Moreover, as the method does not rely on enzyme/substrate reactions for signal generation, it reduces the cost of assay by saving on reagents. Overall processing time of the assay is less than 90 min with a relatively cheaper cost of less than US\$5 per sample. Thus, this simple yet efficient method can pave the way for the development of next generation global DNA methylation level-based cancer diagnosis and monitoring platforms.

## References

- [1] P. W. Laird, "Principles and challenges of genome-wide DNA methylation analysis," *Nature Reviews Genetics* 2010 11:3, vol. 11, no. 3, pp. 191–203, Feb. 2010.
- [2] S. Liu, P. Wu, W. Li, H. Zhang, and C. Cai, "An electrochemical approach for detection of DNA methylation and assay of the methyltransferase activity," *Chem. Commun.*, vol. 47, no. 10, pp. 2844–2846, Feb. 2011.
- [3] W. J. Locke *et al.*, "DNA Methylation Cancer Biomarkers: Translation to the Clinic," *Front. Genet.*, vol. 0, p. 1150, Nov. 2019.
- [4] M. M. Suzuki and A. Bird, "DNA methylation landscapes: provocative insights from epigenomics," *Nature Reviews Genetics* 2008 9:6, vol. 9, no. 6, pp. 465–476, Jun. 2008.
- [5] K. Armstrong, E. Bermingham, and S. Bassett, "Global DNA methylation measurement by HPLC using low amounts of DNA," *Biotechnol. J.*, vol. 6, no. 1, pp. 113–117, Jan. 2011.
- [6] T. Nakagawa, M. Wakui, T. Hayashida, C. Nishime, and M. Murata, "Intensive optimization and evaluation of global DNA methylation quantification using LC-MS/MS," *Anal. Bioanal. Chem.*, vol. 411, no. 27, pp. 7221–7231, Nov. 2019.
- [7] F. F. L. L. and W. S., "Fluorescent conjugated polymer-based FRET technique for detection of DNA methylation of cancer cells," *Nature protocols*, vol. 5, no. 7, pp. 1255–1264, 2010.
- [8] Z. Wang, X. Wang, S. Liu, J. Yin, H. W.-A. chemistry, and undefined 2010, "Fluorescently imaged particle counting immunoassay for sensitive detection of DNA modifications," *ACS Publ.*, vol. 127, no. 3, pp. 9901–9908, Dec. 2005.
- [9] X. Wang, Y. Cui, and J. Irudayaraj, "Single-Cell Quantification of Cytosine Modifications by Hyperspectral Dark-Field Imaging," *ACS Nano*, vol. 9, no. 12, pp. 11924–11932, Oct. 2015.
- [10] C. Bock *et al.*, "Quantitative comparison of DNA methylation assays for biomarker development and clinical applications," *Nature Biotechnology* 2016 34:7, vol. 34, no. 7, pp. 726–737, Jun. 2016.
- [11] X. Chen *et al.*, "Electrochemical Biosensor for DNA Methylation Detection through Hybridization Chain-Amplified Reaction Coupled with a Tetrahedral DNA Nanostructure," *ACS Appl. Mater. Interfaces*, vol. 11, no. 4, pp. 3745–3752, Jan. 2019.
- [12] J. W. Chung *et al.*, "The prognostic role of preoperative serum albumin/globulin ratio in patients with non-metastatic renal cell carcinoma undergoing partial or radical nephrectomy," *Sci. Rep.*, vol. 10, no. 1, Dec. 2020.
- [13] D. K. Ban *et al.*, "Direct DNA Methylation Profiling with an Electric Biosensor," *ACS Nano*, vol. 14, no. 6, pp. 6743–6751, Jun. 2020.
- [14] K. Koo *et al.*, "eMethylsorb: rapid quantification of DNA methylation in cancer cells on screen-printed gold electrodes," *pubs.rsc.org*, vol. 00, pp. 1–3, 2013.

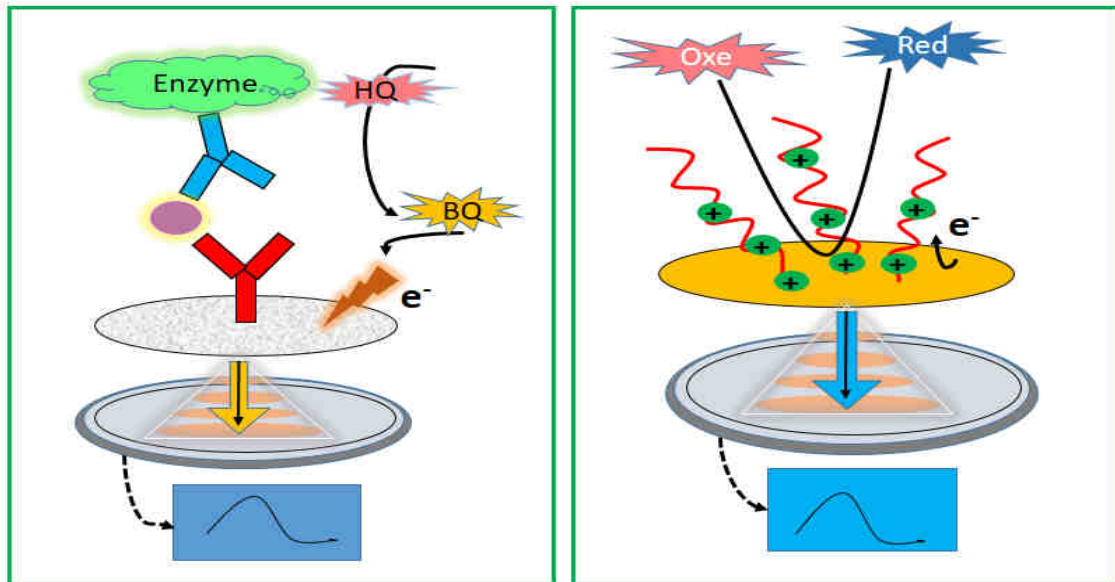
- [15] W. GL, Z. LY, L. HQ, and L. NB, “Electrochemical strategy for sensing DNA methylation and DNA methyltransferase activity.,” *Anal. Chim. Acta*, vol. 768, no. 1, pp. 76–81, Jan. 2013.
- [16] Md. H. Haque *et al.*, “Colorimetric and electrochemical quantification of global DNA methylation using a methyl cytosine-specific antibody,” *Analyst*, vol. 142, no. 11, pp. 1900–1908, May 2017.
- [17] H. MH *et al.*, “Detection of regional DNA methylation using DNA-graphene affinity interactions,” *Biosensors & bioelectronics*, vol. 87, pp. 615–621, Jan. 2017.
- [18] H. MH *et al.*, “Quantification of gene-specific DNA methylation in oesophageal cancer via electrochemistry,” *Analytica chimica acta*, vol. 976, pp. 84–93, Jul. 2017.
- [19] B. R, M. S, N. NT, and S. MJA, “A bisulfite treatment and PCR-free global DNA methylation detection method using electrochemical enzymatic signal engagement,” *Biosensors & bioelectronics*, vol. 126, pp. 102–107, Feb. 2019.
- [20] R. Bhattacharjee *et al.*, “Porous nanozymes: The peroxidase-mimetic activity of mesoporous iron oxide for the colorimetric and electrochemical detection of global DNA methylation,” *J. Mater. Chem. B*, vol. 6, no. 29, pp. 4783–4791, 2018.
- [21] P. Liu *et al.*, “Enzyme-free colorimetric detection of DNA by using gold nanoparticles and hybridization chain reaction amplification,” *Anal. Chem.*, vol. 85, no. 16, pp. 7689–7695, Aug. 2013.
- [22] L. Xiao *et al.*, “A MoS<sub>2</sub> nanosheet-based fluorescence biosensor for simple and quantitative analysis of DNA methylation,” *mdpi.com*, vol. 16, no. 10, Sep. 2016.
- [23] Y. Wang, E. J. H. Wee, and M. Trau, “Accurate and sensitive total genomic DNA methylation analysis from sub-nanogram input with embedded SERS nanotags,” *Chemical Communications*, vol. 52, no. 17, pp. 3560–3563, Feb. 2016.
- [24] L. Carrascosa, A. Sina, ... R. P.-C., and undefined 2014, “Molecular inversion probe-based SPR biosensing for specific, label-free and real-time detection of regional DNA methylation,” *pubs.rsc.org*, vol. 00, pp. 1–3, 2012.
- [25] M. K. Masud *et al.*, “Superparamagnetic nanoarchitectures for disease-specific biomarker detection,” *Chemical Society Reviews*, vol. 48, no. 24, pp. 5717–5751, Dec. 2019.
- [26] N. Soda, B. H. A. Rehm, P. Sonar, N.-T. Nguyen, and M. J. A. Shiddiky, “Advanced liquid biopsy technologies for circulating biomarker detection,” *J. Mater. Chem. B*, vol. 7, no. 43, pp. 6670–6704, Nov. 2019.
- [27] F. Ma, Q. Zhang, and C. Y. Zhang, “Nanomaterial-based biosensors for DNA methyltransferase assay,” *J. Mater. Chem. B*, vol. 8, no. 16, pp. 3488–3501, Apr. 2020.
- [28] D. M *et al.*, “DNA methylation detection by a novel fluorimetric nanobiosensor for early cancer diagnosis,” *Biosensors & bioelectronics*, vol. 60, pp. 35–44, Oct. 2014.
- [29] H. Yin *et al.*, “A new strategy for methylated DNA detection based on

- photoelectrochemical immunosensor using Bi<sub>2</sub>S<sub>3</sub> nanorods, methyl bonding domain protein and anti-his tag antibody,” *Biosensors and Bioelectronics*, vol. 51, pp. 103–108, Jan. 2014.
- [30] D. Kato *et al.*, “A nanocarbon film electrode as a platform for exploring DNA methylation,” *J. Am. Chem. Soc.*, vol. 130, no. 12, pp. 3716–3717, Mar. 2008.
- [31] A. A. I. Sina, L. G. Carrascosa, R. Palanisamy, S. Rauf, M. J. A. Shiddiky, and M. Trau, “Methylsorb: A simple method for quantifying DNA methylation using DNA-gold affinity interactions,” *Anal. Chem.*, vol. 86, no. 20, pp. 10179–10185, Oct. 2014.
- [32] A. B. Steel, T. M. Herne, and M. J. Tarlov, “Electrochemical quantitation of DNA immobilized on gold,” *Anal. Chem.*, vol. 70, no. 22, pp. 4670–4677, Nov. 1998.
- [33] Y. Liu, K. Ai, and L. Lu, “Polydopamine and its derivative materials: Synthesis and promising applications in energy, environmental, and biomedical fields,” *Chem. Rev.*, vol. 114, no. 9, pp. 5057–5115, May 2014.
- [34] L. C, D. IB, S. K, and H. JO, “DNA methylation in human epigenomes depends on local topology of CpG sites,” *Nucleic acids research*, vol. 44, no. 11, pp. 5123–5132, Jun. 2016.
- [35] L. Gorgannezhad, M. Umer, M. Islam, N. N.-L. on a Chip, and undefined 2018, “Circulating tumor DNA and liquid biopsy: opportunities, challenges, and recent advances in detection technologies,” *pubs.rsc.org*, vol. 18, no. 8, p. 1174, Apr. 2018.
- [36] E. J. H. Wee, T. H. Ngo, and M. Trau, “Colorimetric detection of both total genomic and loci-specific DNA methylation from limited DNA inputs,” *Clin. Epigenetics 2015 71*, vol. 7, no. 1, pp. 1–9, Jul. 2015.
- [37] R. Pacaud, E. Brocard, L. Lalier, E. Hervouet, F. M. Vallette, and P.-F. Cartron, “The DNMT1/PCNA/UHRF1 disruption induces tumorigenesis characterized by similar genetic and epigenetic signatures,” *Sci. Reports 2014 41*, vol. 4, no. 1, pp. 1–9, Mar. 2014.
- [38] T. T *et al.*, “Genome-wide methylation profiling of ovarian cancer patient-derived xenografts treated with the demethylating agent decitabine identifies novel epigenetically regulated genes and pathways,” *Genome Med.*, vol. 8, no. 1, Oct. 2016.
- [39] A. A. I. Sina *et al.*, “Epigenetically reprogrammed methylation landscape drives the DNA self-assembly and serves as a universal cancer biomarker,” *Nat. Commun. 2018 91*, vol. 9, no. 1, pp. 1–13, Dec. 2018.
- [40] P. E *et al.*, “Rapid Electrochemical Assessment of Tumor Suppressor Gene Methylations in Raw Human Serum and Tumor Cells and Tissues Using Immunomagnetic Beads and Selective DNA Hybridization,” *Angewandte Chemie (International ed. in English)*, vol. 57, no. 27, pp. 8194–8198, Jul. 2018.
- [41] Z. Yang, W. Jiang, F. Liu, Y. Zhou, ... H. Y.-C., and undefined 2015, “A novel electrochemical immunosensor for the quantitative detection of 5-hydroxymethylcytosine in genomic DNA of breast cancer tissue,” *pubs.rsc.org*, vol. 00, pp. 1–3, 2015.

- [42] S. R. Teixeira *et al.*, “Direct monitoring of breast and endometrial cancer cell epigenetic response to DNA methyltransferase and histone deacetylase inhibitors,” *Biosens. Bioelectron.*, vol. 141, p. 111386, Sep. 2019.

# CHAPTER FIVE

## Conclusions





## CHAPTER FIVE

---

### 5 Conclusions

In this research, a starch-assisted gel formation method has been developed for the synthesis of C-IONPs to mitigate some of the limitations of current synthetic techniques, such as cumbersome steps, harsh conditions, and toxicity. Scanning electron and transmission electron microscopy analysis revealed that starch assisted method was successfully used to synthesis COOH functionalized ferric oxide ( $\text{Fe}_2\text{O}_3$ ) nanoparticles with controlled size and morphology in a facile way. The current research revealed that carboxyl group-functionalized iron oxide nanoparticles (C-IONPs) showed Peroxidase-mimicking activity that was investigated through catalytic oxidation of 3,3',5,5'-tetramethylbenzidine (TMB) in the presence of  $\text{H}_2\text{O}_2$ . C-IONPs nanoparticles follows typical Michaelis-Menten kinetics and exhibits excellent affinity towards TMB and  $\text{H}_2\text{O}_2$  with estimated  $K_M$  and  $V_{\text{Max}}$  values of 0.0992 mM and  $0.156 \times 10^{-8} \text{ Ms}^{-1}$  for TMB, and 114 mM and  $0.197 \times 10^{-8} \text{ Ms}^{-1}$  for  $\text{H}_2\text{O}_2$ , respectively.

C-IONPs were used to develop a rapid, easy and inexpensive method for the direct isolation and quantification of disease-specific exosomes. C-IONPs were used as “dispersible nanocarriers” to capture the bulk population of exosomes and were used as nanozymes to generate an enzyme catalyzed current indicative of the presence of tumor-specific exosomes. Chronoamperometric analysis showed that the method exhibits an excellent specificity for OVCAR3 cell-derived exosomes (linear dynamic range,  $6.25 \times 10^5 - 1.0 \times 10^7$  exosomes/mL; detection limit,  $1.25 \times 10^6$  exosomes/mL) with a relative standard deviation of  $<5.0\%$  ( $n=3$ ). Due to their excellent enzyme catalytic activity, ability to magnetically separate target from bulk samples, and versatile bioconjugation capability (because of the  $-\text{COOH}$  group), C-IONPs are a promising candidate for the development of advanced exosome biosensing assays for various clinical applications

Furthermore, a magnetic nanoparticles-assisted methylated DNA immunoprecipitation (*e*-Magnetomethyl IP) coupled with electrochemical quantification of global DNA methylation have been reported. The amount of DNA adsorbed on the electrode surface, which corresponds to the DNA methylation level in sample, was electrochemically estimated by differential pulse voltammetric (DPV) study of electroactive indicator  $[\text{Ru}(\text{NH}_3)_6]^{3+}$  bound to the surface-adsorbed DNA. The assay could successfully detect as low as 5% differences in global DNA methylation levels with high reproducibility (relative standard deviation (% RSD) =  $<5\%$  for  $n$

= 3). The method could also reproducibly analyze various levels of global DNA methylation in synthetic samples as well as cell lines. The method avoids bisulfite treatment, does not rely on enzymes for signal generation, and can detect global DNA methylation using clinically relevant quantities of sample DNA without PCR amplification. This proof-of-concept method could potentially find applications for liquid biopsy based global DNA methylation analysis in point-of-care settings.

Finally, this research discovered that a -COOH functionalized magnetic iron oxide nanozyme can be used to detect cancer biomarkers in a sensitive and specific electrochemical manner, laying the groundwork for the development of advanced nanomaterials for a variety of diagnostic applications.

## PUBLICATIONS

---

### Publications arising from this research:

1. **Fatema Zerine Farhana**, Muhammad Umer, Ayad Saeed, Amandeep Singh Pannu, Sediqa Husaini, Prashant Sonar, Shakhawat H Firoz,\* Muhammad J. A. Shiddiky\**e-MagnetoMethyl IP: A magnetic nanoparticles-mediated immunoprecipitation and electrochemical detection method for global DNA methylation. *Analyst*, 2021,146, 3654-3665. [Impact Factor: 4.616]*
2. **Fatema Zerine Farhana**, Muhammad Umer, Ayad Saeed, Amandeep Singh Pannu, Mahboobeh Shahbazi, Aiden Jabur, Hyun Jae Nam<sup>d</sup>, Ken (Kostya) Ostrikov, Prashant Sonar\*, Shakhawat H Firoz\*, Muhammad J. A. Shiddiky\**Direct Isolation and Detection of Exosomes Using Peroxidase Mimetic Fe<sub>2</sub>O<sub>3</sub>Nanoparticles. *ACS applied nano materials*, 2021, 4, 2, 1175–1186. [Impact Factor: 5.097]*
3. Rabbee G. Mahmudunnabi, † **Fatema Zerine Farhana**, † Navid Kashaninejad, Shakhawat H. Firoz, Yoon-Bo Shim ,Muhammad J. A. Shiddiky. *Nanozyme-based electrochemical biosensors for disease biomarker detection. *Analyst*, 2020,145, 4398-4420. [Impact Factor: 4.616]*